2018

Aerodynamic performance analysis and inverse design of horizontal axis wind turbines

Behnam Moghadassian

Iowa State University

Follow this and additional works at: https://lib.dr.iastate.edu/etd

Part of the Aerospace Engineering Commons, and the Oil, Gas, and Energy Commons

Aerodynamic performance analysis and inverse design of horizontal axis wind turbines

by

Behnam Moghadassian

A dissertation submitted to the graduate faculty

in partial fulfillment of the requirements for the degree of

DOCTOR OF PHILOSOPHY

Major: Aerospace Engineering

Program of Study Committee:
Anupam Sharma, Major Professor
Ming-Chen Hsu
Ganesh Rajagopalan
Partha Sarkar
Eugene Takle

The student author, whose presentation of the scholarship herein was approved by the
program of study committee, is solely responsible for the content of this dissertation. The
Graduate College will ensure this dissertation is globally accessible and will not permit
alterations after a degree is conferred.

Iowa State University

Ames, Iowa

2018

DEDICATION

I dedicate this thesis to my beautiful mom Pooran, my dad Majid, and my brother Peyman for their inspirations and encouraging words.

TABLE OF CONTENTS

LIST OF TABLES

LIST OF FIGURES

ACKNOWLEDGEMENTS

ABSTRACT

A description of my works in the field of wind turbine aerodynamic analysis and design is given in this dissertation. My main focus has been on analyzing and suggesting novel ideas to enhance energy capture by wind turbines and windfarms. Based on the problems I have solved throughout my research, I have classified my contributions in three chapters.

First, I analyzed the aerodynamic performance of dual rotor wind turbines (DRWTs) and compared it to the traditional single rotor wind turbines (SRWTs). There are multiple forms of aerodynamic loss that hinder energy capture by wind turbines from reaching the Betz limit (59.3%). DRWTs were suggested as a new concept to get more power from windfarms and wind turbines operating in isolation by mitigating blade root loss and wake loss. In my research, I used a high-fidelity solver (large eddy simulation, LES) to analyze the aerodynamic performance and loads on DRWTs under different stability conditions of the turbulent atmospheric boundary layer (ABL). The actuator line method (ALM) was used to model the rotating turbine blades. Moeng wall model was applied to obviate a high resolution mesh in the high gradient regions near the ground. The mixing length model by Smagorinsky was used to model eddy viscosity. Aerodynamic analysis was quantified by the mean velocity and turbulent intensity at different axial locations in the wake of wind turbine. In addition, the effect of using a secondary rotor on wake loss mitigation was checked by computing the momentum entrainment into the turbine wake layer. Moreover, the changes in loading (specifically, out-of-plane blade moment) and mechanical power of wind turbines were computed both in time and spectral domains. My findings confirm that the DRWT can improve the aerodynamic performance (C_P) by 5-6% for all ABL conditions compared to the corresponding SRWT. The DRWT also enhanced wake mixing and entrainment of higher momentum fluid from outside the wake layer for moderately high atmospheric turbulence (such as in the neutral stability ABL).

Results of the first investigation led me to the second part of this thesis. There was room for

improvement in energy capture by using DRWT instead of SRWT. However, neither SRWTs, nor DRWTs were particularly designed to give the best aerodynamic performance; and that's what I focused on. The aerodynamic performance of a wind turbine is strongly dependent on its blade geometry. In my work, I measured the angle of attack and axial induction factor to quantify the aerodynamic behavior. Then, the design problem is posed as follows: what should the blade chord and twist distribution be to achieve the preferred (desired) values of angle of attack and axial induction factor along the blade? This is an inverse problem, because technically it is needed to find the causes (i.e. the blade geometry) of some system behavior (i.e. the turbine aerodynamic response). I used the trust region reflective (TRF) method, which is an iterative method, to find the optimal blade geometry that produces the desired aerodynamic behavior along the blades. For iterative design processes, high-fidelity aerodynamic models (such as LES) are usually not suitable as the computational cost becomes prohibitive. Therefore, the medium-fidelity Reynolds Averaged Navier-Stokes (RANS) is employed as the aerodynamic model. The effect of rotating blades was modeled by the actuator disk method (ADM). Prandtl's tip loss correction was applied to account for the finite length of the blades. Based on the choices for the direct (i.e. aerodynamic) and inverse solvers, a design algorithm was proposed to find the blade geometry. The goals were twofold: 1) to make sure that the algorithm was capable of providing the desired aerodynamic features and 2) to extend the design process to DRWTs. The design algorithm was tested on different single- and dual-rotor turbines. The desired aerodynamic behavior and the airfoils constituting the blade varied from case to case to verify the robustness of the algorithm. It was found that the proposed algorithm could give blade geometries that resulted in the desired aerodynamic behavior. Moreover, the TRF method was compared to the multi-dimensional Newton method, which is a commonly-used inverse solver. The extension of the design algorithm to DRWTs was successful.

While my results demonstrated improvements in performance and design of isolated wind turbines, the ultimate goal of my research was to get maximum power from windfarms where multiple turbines, as opposed to an isolated turbine, are placed to capture wind energy. Design of windfarms is different than the design of isolated turbines because turbines in a farm face

different inflow conditions depending on their location in the windfarm. The downstream turbines may operate in the wake of upstream turbines under certain flow conditions (direction). Employing RANS and ADM enabled me to simulate the turbine wake flow and extend the blade design to windfarms. My objective was to find an answer to this question: what should the blade geometry be to maximize total power output from a windfarm with n in-line wind turbines? In addition, from previous experience in blade design, it was found that calculation of Jacobian matrix with a finite difference scheme took majority of the total computational time. Therefore, I added the Broyden's method, which is a quasi-Newton method that recursively approximates the Jacobian matrix, to the proposed algorithm. First, design of isolated SRWTs and DRWTs wind turbines was tested using the proposed method. Difference between the blades that were specifically designed for maximum power and those that were not (such as Betz' optimal turbine) were analyzed. For three in-line turbines, it was demonstrated that if turbines could have different individual blade designs, a higher total power could be achieved. However, we proposed a unique blade design for all turbines which resulted in slightly less total power but avoided extra costs of manufacturing different blades. For the case of ten in-line turbines, remarkable gain in power achieved by considereng all the turbines into the design process.

CHAPTER 1.   INTRODUCTION AND BACKGROUND

1.1   Background

Power has been extracted from wind for more than a couple of centuries with notable designs of windmills. Initial windmills were usually built from wood, fabric, and stone. The end goal of using windmills were pumping water or to grinding grains. Windmills were typically large, isolated and not very efficient. They were supplanted in the nineteenth century by fossil-fuel powered machines. However, burning of fossil fuels has undesireable environmental effects and has raisen worldwide interest in clean energy. In the last half of the twentieth century, improved understanding of aerodynamic features and advences in material science have prompted the arrival of a new generation of devices for extracting wind energy. Wind energy machines are now primarily used to generate power, and often referred to as wind turbines [2]. Wind energy is now established as a modern well-developed industry. Today, the advancement, make and operation of wind turbines are not limited to small laboratory scales anymore.

In the last two decades, wind turbines have become the preferred source of sustainable power in the world. By late 2016, the total capacity of wind turbines around the world achieved about 500 GW of electrical power[3]. In 2016, renewable energy in the United States reached 609.44 GkW-h (giga kilowatt hours) and was responsible for generating 14.94% of the local electricity, and 11.1% of total energy. In 2016, wind energy in the United States came to 226.5 GkW-h, or 5.55% of total generated electrical energy and 37.1% of the renewable energy [4]. Wind energy systems also improve local economies and create jobs, and attract diverse interested sectors, from private people to large enterprises. This remarkable interest has led to significant and constant advances in turbines. Wind-driven electricity has experienced a tremendous rise in the last two decades and it is predicted to continue to grow. As Global Wind Energy Council

indicated, by 2020 aggregate worldwide wind capacity could supply 17-19% of the world's power needs [3].

Continuation of such trmendous development in wind turbines depends on improved understanding of wind turbine aerodynamics. Wind turbines are now found everywhere, even in the most remote areas throughout the world. They experience unique environmental conditions and corresponding aeromechanical loads, and are usually expected to last for more than 120,000 working hours over their lifetime. Turbines are designed to work at their best in different conditions, for example in low or high wind speeds, offshore or onshore locations, etc. Therefore, accurate predictions are needed to design wind turbines for persistent ideal performance during their lifetime. Future challenges can be foreseen and overcome through advancements and innovation in experiments and simulations of wind turbines in action[5].

Wind turbines are classified based on the variations in turbine operating condition, turbine setup, output power, etc. Besides the general operating conditions, such as working onshore or offshore, the configuration of the shaft and rotational axis decides the principal grouping of wind turbines. A turbine with a shaft mounted parallel to the ground is known as a horizontal axis wind turbine (HAWT), while a vertical axis wind turbine (VAWT) has its shaft perpendicular to the ground. The two setups have immediately discernable rotor configurations, each with its own positive and negative attributes. In general, a typical VAWT can accept the wind from any direction and does not need a complicated yawing algorithm. VAWTs also use a vertical shaft; so overwhelming generator and gearbox can be mounted on the ground to diminish tower loads. On the other hand, VAWTS are known to have a low tip speed ratio and troubles in controlling rotor speed. Also until not long ago, it was incorrectly believed that VAWTs are not capable of a self-start. All these drawbacks have hindered advancement of VAWTs. However, to harness their good qualities, VAWTs are not totally neglected for future improvement. A novel V-formed VAWT rotor configuration is currently under investigation [6, 7]. This turbine is as of now doubtful on a megawatt scale, requiring advancements in design and analysis before it can be considered for commercial usage. Meanwhile, HAWTs typically have tall towers and expanded rotor control through handling pitch and yaw. Tall towers of HAWTs lead to some major disadvantages. Towers have to support heavy forces and moments. These loads consist

of aerodynamic forces on the blades as well as gravitational loads of each part. Extraordinary heights of turbine towers also pose additional installation and maintenance challenges. However, HAWTs benefit from tall towers by having access to higher speed wind in the upper atmosphere. Increasing wind speed enhances the aerodynamic loads on blades and eventually on tower. This is an undesireable effect from structural point of view. However, higher wind speed also leads to more power generation by wind turbine. Wind speed usually increases with going up in the atmosphere. At each point, vertical atmospheric wind shear is the difference in wind speed over a relatively short distance from that point in the atmosphere. In some regions with high wind shear, every ten meters above the ground the wind speed increases by 20% and the generated power by 34% [8]. Besides, HAWTs have generally higher efficiency than VAWTs, because the blades face the wind and generate power in their entire 360° of rotation. These positive attributes have made HAWT the more accepted design and has been promoted by the most of the current large-scale turbine manufacturers [9].

Like most large energy systems, wind turbines are installed in a group and work in a same location to capture the wind energy with a higher overall efficiency and less effort [10]. A windfarm, also known as wind plant, is where a group of turbines are installed. Power extraction from wind turbines and windfarms is not without its difficulties. Distinctive areas, situations, and national and local regulations have to be considered when arranging and executing a wind energy project. The following elements are possibly the most relevant factors: how is the nearby network grid? Are there political confinements or district laws that could confuse the improvement?, etc. Likewise, limited ecological limitations, for example, turbine height, noise level, and wildlife threats all need to be considered. Furthermore, some areas have higher fluctuations in wind, which should be taken into the account [11, 12].

Nonetheless, power generation is still the main purpose of utility-scale wind turbines and farms. Power is generated by the interaction of wind and wind turbine blades. Therefore, from an aero/mechanical engineer's point of view, one of the most important tasks is to investigate this interaction and its effect on the generated power. Wind flow and turbine blades both affect one another. While the wind make the turbine blades rotate which eventually transforms into the electrical energy; the rotation of blades influences the airflow as well. The airflow upstream

and downstream of a wind turbine are very different in terms of circulation, velocity, pressure, turbulent intensity and even temperature. To understand this mutual impact, corresponding equations that govern airflow and motion of turbine blades need to be solved.

1.2 Aerodynamic analysis of single- and dual rotor wind turbines

In 1919, physicist Albert Betz demonstrated that for a hypothetically perfect wind energy capturing machine, the basic laws of continuity and energy conservation allow up to 16/27 (59.3%) of the energy in the wind to be captured [13]. Modern wind turbines can achieve 70 to 80% of this theoretical cutoff [14].

In practice, wind turbines face several complications (or as known in wind energy community, losses) that hinder them from reaching the Betz' limit. Two major losses are blade root loss and wake loss. Wind turbine rotor blades are made by stacking airfoils along the blade span. The main impetus of blade rotation is the lift force created due to a pressure difference in the flow over of airfoils. The blade root area is the closest to the hub and comprises 20-25% of the total blade length. The rest of the blade is the outboard region. Present-day utility-scale HAWT rotor blades are aerodynamically optimized in the outboard region, though the blade root area is designed essentially to withstand structural loads. Generally, airfoils with high thickness-to-chord ratio are not very preferred for wind turbines because they do not have high lift-to-drag ratio. However, they are used in large wind tubine blades as a part of the blade root area so that it has structural integrity. Studies show that in some cases, the blade root region not only does not contribute to the overall power generation from a wind turbine, but instead it generates negative torque that opposes the generation of power [15, 16, 17]. Because of blade root loss, each turbine loses up to 5% of its ability to capture wind energy. It happens even in turbines that work in isolation, i.e., with no other turbine close-by. However, most utility-scale turbines are installed in windfarms, with various turbines working in the vicinity of each other. Because turbines are tightly-spaced in a windfarm, cluster interference (wake) loss occurs. This loss occurs because of the aerodynamic interplay between turbines in windfarms and has been measured to be in the range of 8% and 40% relying upon windfarm location, farm design, atmospheric stability condition as well as wind speed and direction [18, 19, 20].

Single rotor wind turbines (SRWTs) have been heavily studied. There have been limited theoretical studies in the 80s on the performance of wind turbines with more than one rotor [21, 22, 23]. They used several simplifying assumptions (uniform flow, no turbulence, 1-D momentum, etc.) to be able to present an analytical solution. Recently proposed wind turbines with two rotors (commonly organized as two rotors in tandem so that the incoming stream area is unaltered) are known as dual rotor wind turbines (DRWTs). DRWT innovation has been shown to diminish blade root and wake losses in wind turbines and windfarms [24, 25, 26]. It uses an auxiliary, smaller, co-axial rotor to mitigate the wake- and blade root losses.

One idea is to reduce the blade root loss through the use of a smaller aerodynamically tailored rotor in front (or in the back) of the large main rotor. Power generation and aerodynamic loads on blades are directly dependent on rotor size. Considering failure of wind-turbine rotor blades due to aerodynamic and gravitational loads is an integral part of blade/rotor/tower design process. In general, aerodynamic loads are larger in magnitude than the gravitational loads. Bending of the rotor blades exhibits a periodic behavior, and so does the stress response in the rotor blades. Also, normal stresses in blades caused by gravity fluctuate twice in each blade rotation. Loads generated everywhere on the blade pass through the blade root region, into the nacelle, through the tower, and ultimately to the ground. This load acts as a constraint in the design of large blades. The reason that large blades do not generate much power in the root region is because they should be able to resist the loads in the blade root region rather than being aerodynamically optimized. Having a secondary rotor of a smaller size covering the root region of the main rotor allows the DRWT to make up for the negative torque in root region of the main rotor. This is done when airflow reaches the smaller rotor that has been aerodynamically optimized all along its blade span and does not endure any blade root loss.

In addition, previous studies have suggested that the use of secondary rotor can potentially be effective in reducing the wake loss through increasing the momentum entrainment in the turbine wake [16]. Undisturbed airflow possesses a specific level of kinetic energy based on its velocity, turbulent intensity, etc. When it passes through a wind turbine, its mean energy level drops right after the turbine. However, it can re-reach its original kinetic energy content if there is not further disturbance in the wake of the turbine. It is believed that the prominent

mode of re-energizing the airflow is the turbulent momentum transport from free stream into the wake layer [27]. It is shown that even after 20D (D=turbine diameter) behind the turbine, the velocity deficit in the flow still exists [28]. However in practice, windfarms are consist of closely spaced individual wind turbines, with inter-turbine separation distance of less than 10D [29, 19]. Wake loss occurs because flow passing through the first row of a turbine array is not given enough space to fully recover its original energy level before reaching to the second row of turbine. This loss cascades down in a large array of turbines.

Another idea behind using a smaller, aerodynamically optimized secondary rotor in DRWTs is that circulations of the two rotors in the wake of wind turbine pair up. This pairing intensifies drawing the flow with higher turbulence momentum from the free stream into the wake layer and have a flow with higher energy level for the turbines sitting in the next row. Preliminary studies have shown the potential of the DRWT to overcome the blade root losses and enhance the aerodynamic efficiency of the turbine [15]. Those examinations demonstrated an improvement in power generation by around 7% with using the DRWT. However, there are some simplifying assumptions in those studies that do not perfectly reflect the real-world application of wind turbines; for example the wind was considered to be uniform with zero turbulent inflow and no atmospheric boundary layer. One objective of this study is to extend numerical analysis of DRWTs to conditions exprienced by a real wind turbine in the field. Aerodynamic response and loads on blades of DRWTs under different atmospheric stability conditions and comparisons to SRWTs are discussed in this study.

In solving the governing equations of airflow, the blade rotation and forces from the blades on the flow should be assessed exactly or with reasonable approximations. In one computationally efficient yet simplified approach, the blade geometry is not resolved in the simulation. Instead, the forces exerted by the blades on the flow are simulated using source terms (commonly as a body force) in the Navier-Stokes equations. The Actuator Line Method (ALM) [30, 31] and the Actuator Disk Method (ADM) [32] are two common strategies employed to evaluate and apply the blade body forces in numerical models. Both techniques utilize look-up tables for 2-D lift and drag polars (acquired through earlier tests or simulations) with the local relative velocity to compute the net sectional force at each radially discretized component of the blade.

The net force is then applied as a spatially distributied (usually with a Gaussian distribution) source around the component. ALM and ADM can model the blade forces with a reasonable accuracy if a fine enough mesh is used with a suitable spatioal distribution [33]. While more computationally involved, these methods are able to capture turbulent wake mixing, which is an advantage over potential flow techniques, such as the vortex lattice method (VLM) [34, 35]. Therefore, ALM and ADM are suitable for problems that involve investigations of turbine wakes and/or require the accurate assessment of aerodynamic loads.

In this study, the conceptual 5-MW turbine by the National Renewable Energy Laboratory (NREL) is utilized as the standard single-rotor design and also as the main rotor for the DRWT [36]. The secondary rotor was designed utilizing an inverse approach based on the blade element momentum (BEM) theory [15]. Preliminary studies on this DRWT utilized Reynolds Averaged Navier-Stokes (RANS) CFD simulations with an actuator disk model of turbine rotors [15, 1]. In this work, we broaden the analysis of DRWT by including the impact of the atmospheric boundary layer and analyze turbine aerodynamics performance and loads, in addition to wake mixing. High-fidelity Large Eddy Simulation (LES) [37] is used as the mathematical model of the turbulence. Comparative aerodynamic investigations between dual and single rotor wind turbines are performed in uniform inflow with no turbulence, and two atmospheric stability conditions: unstable and stable. One of the concerns with the DRWT innovation is the potential increase in unsteady loads on the main rotor because of its proximity with the secondary rotor. Therefore, unsteady loads and their spectral density are monitored in DRWTs and are compared to SRWTs under the same atmospheric conditions. In our investigation, these loads are assessed numerically by joining LES and ALM and presented as power spectral densities of out-of-plane blade root moment.

1.3   Design of wind turbine blades

Power generation from wind turbines ranges from a couple of kilowatts to 8 MW, as of now the largest active turbine. Producers are targeting turbines of around 10 MW for offshore windfarms [38, 39]. They are attempting to lessen the Cost of Energy (CoE) by expanding turbine dimensions, and eventually decreasing the quantity of turbines in a farm (bringing down

the Cost of Installation and Transportation, CoI), and furthermore by diminishing the aggregate Cost of Operation and Maintenance (CoM) [3]. Power generated is also being augmented through enhanced control, incorporated plan, and site assessments.

In the last 30 years, wind turbine blades have grown 15 times in size, ready to reap more energy from the wind than any other time in the history [40, 41]. The first commercial wind turbines had a limit of 30 kW with a 10 m rotor diameter. Comparing that to the current 8 MW wind turbine by Siemens, which has a rotor diameter of 150 m, examplifies the push in the direction of larger-size turbines. The rotor of a Siemens 8 MW turbine is almost the same size as the wingspan of an A380 plane which makes it the world's biggest rotor in operation today. As the blades increment in size, researchers look for ways to bring the weight down, enhance stability, reduce expenses, facilitate transportation, and expand safety.

In addition, as power generation strongly depends on the design of the wind turbine blades, significant amount of research has concentrated on developing strategies to imorove the blade design [42, 43, 44, 45]. The primary cause of blade rotation is the lift force prompted by the pressure difference on airfoil-shaped cross sections of blades. Lift force is normal to the relative velocity vector and is dependent on the magnitude of relative speed and angle of attack. As a rule of thumb lift and drag forces increments with the angle of attack, before stull happens. While tangential component of the lift force bolsters the blade rotation, the drag force contradicts it. Therefore for a wind turbine, it is desireable to have the highest lift-to-drag ratio on each section of blade. For a given airfoil, lift-to-drag ratio is a function of angle of attack. Airfoil cross sections are adjusted to work at ideal angle of attack in which lift-to-drag ratio is the highest or close to it. For a given flow over an airfoil, angle of attack is a function of the airfoil geometry (chord, twist, etc.).

Geometric design of wind turbine blades has been an active field of research for many years and the design techniques have been evolving ever since. Parametric sweep is arguably the most common traditional design approach. It is quite an easy and straightforward approach. It is still implemented and used in very simple design problems. However, this approach is not effective because it is extremely time-consuming in problems with multiple dependent- and independent design variables. Geometric design of wind turbine blades is a multi-dimensional

problem. Each blade cross section is a 2-D airfoil. Wind turbine blades usually have different airfoils at different radii from hub height. Chord and twist of the airfoils at each section affect the turbine's aerodynamic response as well as sectional and overall power extraction. A recent trend in wind turbine design is the use of multi-dimensional optimization techniques as design tools [43, 45]. Generally, in an optimization problem the goal is to maximize or minimize a target function. Iterative inverse/optimization techniques have recently been implemented for solving blade design problems [45, 46, 47]. Technically, an inverse problem is defined as finding the cause of a specific result. As an instance, we are interested in finding a blade geometry that maximizes the turbine power coefficient or the lift-to-drag ratio along the blade. The solution to an inverse problem usually starts with an initial estimate for design variables. Initial design variables can be found either randomly or by an educated estimate, based on the designer's expertise. Then the target function is assessed. Assessing the target function requires the direct (also known as forward) problem to be solved. In our case for example, the direct problem is to solve the governing equations of aerodynamics and loads of a wind turbine, i.e. Navier Stokes and actuator disk/line models. Solution to the direct problem provides values of the power extraction and lift-to-drag ratio along the blade. Oftentimes when starting with a random initial guess, or even an educated one, calculated target function is not at the optimal point. An inverse solver is then employed to find a new estimation for the design variables. This estimation is done by finding how much and in which direction in design space should the initial estimate change in order to approach the optimum point of target function. The new design variables are inputted in the direct solver and the target function is estimated. In this study, trust region reflective (TRF) method [48, 49] is used to update the design variable at each iteration of the inverse solver. This procedure continues until the target function reaches its optimum point.

For numerical simulation of the direct (aerodynamic) problem, models that solve the Navier-Stokes equations, rather than simplified potential flow solvers such as BEM theory [50] and vortex lattice method (VLM) [51], offer higher fidelity in analyzing wind turbine aerodynamics. The Navier-Stokes equations are usually solved with some assumptions about the flow. In particular for wind turbine aerodynamics, the flow is assumed to be turbulent and incom-

pressible. Turbulence (at least turbulence at high wavenumbers) is modeled, e.g. by utilizing eddy-viscosity based turbulence models. When the interest is just in mean quantities, time variation is disregarded and Reynolds Averaged Navier-Stokes (RANS) equations are solved with turbulence closure models that cover the whole turbulence spectra.

The output power from a wind turbine depends strongly on the turbine blade geometry. Another objective of this study is then to find the turbine blade geometries that result in the maximum output power from isolated wind turbines and windfarms. Reducing levelized cost of energy (LOCE) by designing the turbine blades for maximum turbine power has recently become an interesting topic for researchers in wind energy [52, 53]. However, blade design for windfarm applications has not been investigated. In previous studies, solution of the aerodynamic problem has been found by computationally cheap potential flow solvers such as BEM. The main reason for not using a high- or medium-fidelity aerodynamic model is to keep the computational cost low, especially when the aerodynamic solver is getting called multiple times in an iterative inverse/optimization algorithm. While simple potential flow solvers (like BEM) are typically fast in assessing the wind turbine aerodynamic behavior, they are not well suited for windfarm applications as they cannot model/predict properties of wake flows [54, 55]. There are usually multiple rows of turbines in a windfarm. Turbines in rear rows may have to operate in the wake of turbines in front rows. RANS/ADM has this capability to model the far wake and hence is suitable for windfarm design problems [56]. In this work, the RANS/ADM is utilized with the TRF method to maximize the total power from isolated SRWTs and DRWTs as well as windfarms. To reduce the computational costs, the Broyden method [57] is employed in the proposed algorithm to update the sensitivity matrix recursively.

CHAPTER 2.   NUMERICAL INVESTIGATION OF AERODYNAMIC PERFORMANCE AND LOADS OF A NOVEL DUAL ROTOR WIND TURBINE

Behnam Moghadassian, Aaron Rosenberg, and Anupam Sharma

Abstract

The objective of this paper is to numerically investigate the effects of the atmospheric boundary layer on the aerodynamic performance and loads of a novel dual-rotor wind turbine (DRWT). Large eddy simulations are carried out with the turbines operating in the atmospheric boundary layer (ABL) and in a uniform inflow. Two stability conditions corresponding to neutral and slightly stable atmospheres are investigated. The turbines are modeled using the actuator line method where the rotor blades are modeled as body forces. Comparisons are drawn between the DRWT and a comparable conventional single-rotor wind turbine (SRWT) to assess changes in aerodynamic efficiency and loads, as well as wake mixing, and momentum and kinetic energy entrainment into the turbine wake layer. The results show that the DRWT improves isolated turbine aerodynamic performance by about 5-6%. The DRWT also enhances turbulent axial momentum entrainment by about 3.3%. Highest entrainment is observed in the neutral stability case when the turbulence in the ABL is moderately high. Aerodynamic loads for the DRWT, measured as out-of-plane blade root bending moment, are marginally reduced. Spectral analyses of ABL cases show peaks in unsteady loads at the rotor passing frequency and its harmonics for both rotors of the DRWT.

2.1 Introduction

Modern utility-scale horizontal axis wind turbine (HAWT) rotor blades are aerodynamically optimized in the outboard region, whereas the blade root region is designed primarily to withstand structural loads. Therefore, very high thickness-to-chord ratio airfoils, which are aerodynamically poor, are used in the blade root region to provide structural integrity. Up to 5% loss in wind energy extraction capability is estimated to occur per turbine due to this compromise [58]. This "root loss" occurs even in turbines that operate in isolation, i.e., with no other turbine nearby. Most utility-scale turbines are deployed in clusters, with multiple turbines operating in proximity of each other. Array interference (wake) losses resulting from aerodynamic interaction between turbines in wind farms have been measured to range between 8 - 40% depending on wind farm location, farm layout/wind direction, and atmospheric stability condition [59].

Flatback airfoils [60] and vortex generators [61] have been used in the blade root region to mitigate root losses. Improvements in windfarm efficiency have been sought by optimizing windfarm layout so as to minimize wake interference between turbines [62, 63, 64]. Ideas for windfarm efficiency improvement include the use of counter rotating vertical axis wind turbines (VAWTs) for large-area wind farms to increase power production per unit land area [65]. Other ideas have been pursued for horizontal axis wind turbines in windfarms with set turbine layout. Redirecting the wakes of upstream turbines through yaw misalignment [66, 67] is one such concept. By yawing an upstream turbine, the force exerted by the turbine on the flow (reaction to the thrust force) is turned slightly in the cross-flow direction. A component of this force then acts in a direction perpendicular to the flow velocity, serving as a centripetal force to curve the mean flow and divert the flow/wake away from the turbines immediately downstream. Another idea [68] aims to reduce wake loss through manipulation of the turbulence in the turbine wake by changing the induction factor for the turbine rotor. This can be achieved by various means such as altering the pitch of the blades, the RPM of the rotor, or the yaw of the nacelle.

Wind turbines with two rotors (typically arranged in tandem so that the incoming flow stream area is unchanged) are known as dual rotor wind turbines (DRWTs). Newman [69]

developed a multi-rotor actuator disk theory and demonstrated that a turbine with two equal-size rotors, could capture up to 8% more energy than a corresponding SRWT. Previous research on DRWTs has been focused on increasing wind energy capture by harvesting the kinetic energy left in the wind after it passes through the turbine rotor. Jung *et al.* [70] explored a 30 kW counter-rotating dual-rotor wind turbine. It featured an eleven-meter diameter main rotor with a 5.5 meter auxiliary rotor located upwind of the main rotor. This DRWT uses a bevel gear to couple the counter-rotating shafts. The authors used quasi-steady strip theory and a wake model to predict the performance of several DRWT configurations. They predicted a 9% increase in turbine power coefficient (C_P) when compared with a single-rotor configuration. Other studies have led to patents including Kanemoto and Galal [71, 72] who propose a DRWT with two different sized upwind rotors driving a generator with two rotating armatures.

The DRWT technology by Rosenberg *et al.* [1, 73] (see Fig. 2.1) takes a different approach - it aims at reducing losses (blade root and wake losses) in wind turbines and windfarms. It utilizes a secondary, smaller, co-axial rotor to mitigate root losses and to enhance mixing of the turbine wake. Rosenberg *et al.* [1] and Selvaraj [74] introduced this turbine technology and presented preliminary aerodynamic analyses of a DRWT design. The conceptual 5 MW offshore turbine by NREL [75] was used as the baseline single-rotor design and also as the main rotor for the DRWT. The secondary rotor was designed using an inverse design approach based on the blade element momentum theory. The design and optimization approach used Reynolds Averaged Navier-Stokes (RANS) computational fluid dynamics (CFD) simulations with an actuator disk representation [76] of turbine rotors. RANS CFD analyses showed an increase in C_P of around 7% with the DRWT.
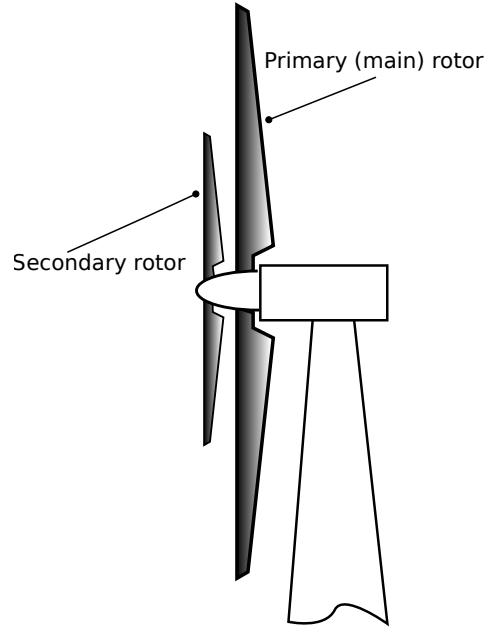
Figure 2.1: A cartoon of the DRWT technology proposed by Rosenberg *et al.* [1].

In this paper, we extend the analyses of Refs. [1], [73] and [74] by including the effect of the atmospheric boundary layer, and investigate turbine aerodynamic performance and loads, as well as wake mixing. We present comparative (between DRWT and SRWT) isolated turbine aerodynamic analyses for uniform inflow with no incoming turbulence, and two atmospheric stability conditions - neutral and stable. An improvement of about 6% in C_P through root loss reduction is demonstrated. Analysis of turbine wake shows increased momentum and kinetic energy entrainment in the wake layer of the DRWT. One of the concerns with the DRWT technology is the potential of increased unsteady loads on the primary rotor due to its proximity with the secondary rotor. These loads are computed numerically using LES and reported as power spectral densities of out-of-plane blade root moment. No significant increase in loads is observed for the DRWT.

The remainder of the paper is laid out as follows. A summary of the numerical method utilized in this study and its validation against experimental data are presented first. Code validation and parallel scalability results are also presented in this section. Section 3.2.2 summarizes the computational setup, grids, and simulation details, including the assumptions made in the present calculations. Aerodynamic performance results are described in section 4.3 wherein

comparisons are drawn between a SRWT and a DRWT operating in uniform inflow and in neutral- and stable atmospheric boundary layer (ABL) flow. Section 4.3 also investigates the aerodynamic loads on the two rotors of the DRWT for the different inflow conditions. The conclusions are presented in the final section.

2.2   Numerical Method

A wide range of methods can be used to model wind turbine and wind farm aerodynamics. Analytical models [77, 78] and semi-analytical models, such as blade element momentum theory, vortex lattice methods, etc. [79] have been extensively used for design and analysis of wind turbines operating in isolation. Wind turbine wake dynamics and windfarm aerodynamics have been investigated using parabolic methods [80] and computational fluid dynamics (CFD) methods. CFD methods can range from time-averaged Reynolds Averaged Navier-Stokes (RANS) simulations [81] to large eddy simulations (LES) [82] that resolve energy containing turbulence in the atmosphere and turbine wakes. Vermeer [83] provides an overview of aerodynamics of wind turbine aerodynamics as well as wind farm aerodynamics through a survey of existing numerical as well as experimental work. Sanderse [84] reviews different numerical methods currently being used for aerodynamic analysis of wind turbines and wind farms.

Recent research on numerical modeling of wind turbine and windfarm aerodynamics has largely focused on using LES (see e.g., Refs. [85, 86, 87, 88, 89, 90, 91]). Jimenez *et al.* [85, 86] used incompressible LES to model the aerodynamics of a single wind turbine (modeled as an actuator disk) in an atmospheric boundary layer. Troldborg *et al.* [89] investigated aerodynamic interaction between two turbines using an actuator line model coupled with an LES flow solver. Aerodynamic interaction between the turbines was simulated for varying atmospheric turbulence intensity, distance between the turbines, and partial and full-wake operation of the downstream turbine. Porte-Agel *et al.*[90] investigated wake losses in an offshore windfarm with varying wind direction using LES. Stevens *et al.* [91] investigated effects of alignment of turbines in a windfarm and identified optimal staggering angles to use for micrositing (windfarm layout).

The Simulator fOr Wind Farm Application (SOWFA) [92, 93] software is the LES flow solver used in this work. SOWFA solves spatially filtered, incompressible forms of continuity and Navier-Stokes equations (see Eq. 2.1). The grid-filter width, computed as cube-root of the cell volume $\Delta = (\Delta_x \Delta_y \Delta_z)^{1/3}$, is used as the spatial filter width. Unresolved, sub-filter (or subgrid) scale stresses introduced by spatial filtering are modeled using a subgrid model. Turbine rotor blades are parameterized using the actuator line model (ALM); blade geometry is not resolved. The actuator line model uses lookup tables for airfoil polars to compute sectional lift and drag forces and applies them as body forces. The governing equations are written in spatially-filtered quantities (denoted by overhead ($\tilde{}$)) as

$$\frac{\partial \widetilde{u}_i}{\partial x_i} = 0,$$

$$\frac{\partial \widetilde{u}_i}{\partial t} + \widetilde{u}_j \left(\frac{\partial \widetilde{u}_i}{\partial x_j} - \frac{\partial \widetilde{u}_j}{\partial x_i} \right) = -\frac{\partial \widetilde{p^*}}{\partial x_i} - \frac{\partial \tau_{ij}}{\partial x_j} + \nu \frac{\partial^2 \widetilde{u}_i}{\partial x_j^2}$$

$$- \underbrace{f_i/\rho_0}_{\text{turbine force}} + \underbrace{\delta_{i1} F_P}_{\text{driving pressure}} + \underbrace{\delta_{i3} g_0 (\widetilde{\theta} - \langle \widetilde{\theta} \rangle)/\theta_0}_{\text{buoyancy force}} + \underbrace{F_c \epsilon_{ij3} \widetilde{u}_j}_{\text{coriolis force}},$$

$$\frac{\partial \widetilde{\theta}}{\partial t} + \widetilde{u}_j \frac{\partial \widetilde{\theta}}{\partial x_j} = -\frac{\partial q_j}{\partial x_j} + \alpha \frac{\partial^2 \widetilde{\theta}}{\partial x_j^2}. \tag{2.1}$$

In the above, θ is potential temperature, α is thermal diffusivity of the fluid, and f_i is the force exerted by turbine rotor blades computed using lookup tables for airfoil lift and drag polars; $\widetilde{p^*} = \widetilde{p}/\rho_0 + \widetilde{u}_j \widetilde{u}_j/2$ is modified kinematic pressure, $\tau_{ij} = \widetilde{u_i u_j} - \widetilde{u}_i \widetilde{u}_j$, is subgrid scale (SGS) stress tensor, and $q_j = \widetilde{u_j \theta} - \widetilde{u}_j \widetilde{\theta}$ is SGS heat flux; ρ_0 and θ_0 are constants based on the Boussinesq approximation. For simulating the atmospheric boundary layer, the flow is driven by a pressure gradient, $\delta_{i1} F_P$; the coordinate system is such that index '1' corresponds to the streamwise direction, '3' points up and normal to the ground, and '2' is determined by the right hand rule. The DRWT is modeled in SOWFA by simulating the two rotors of the DRWT as two single-rotor turbines operating in tandem.

The deviatoric part of the SGS stress tensor (τ_{ij}) is modeled using an eddy-viscosity model, $\tau_{ij} - \delta_{ij} \tau_{kk}/3 = -2\nu_{sgs} \widetilde{S}_{ij}$ and the SGS heat flux with an eddy-diffusivity model $q_j = \widetilde{u_j \theta} - \widetilde{u}_j \widetilde{\theta} = -(\nu_{sgs}/Pr_{sgs}) \partial \widetilde{\theta}/\partial x_j$, where, $\widetilde{S}_{ij} = 1/2 \ (\partial \widetilde{u}_i/\partial x_j + \partial \widetilde{u}_j/\partial x_i)$ is the resolved strain-rate tensor and Pr_{sgs} is the SGS Prandtl number. The mixing length model by Smagorinsky [94] is used to model eddy viscosity as $\nu_{sgs} = (C_S \Delta)^2 |\widetilde{S}|$. In the original model, C_S was assumed to be

a constant, but dynamic calculation of this coefficient has been used in recent years [95, 96]. Improved, tuning-free, scale-dependent SGS models have also been developed (see e.g., Ref. [87]) and used for atmospheric flow and windfarm simulations. The standard Smagorinsky model with $C_S = 0.135$ is used here.

SOWFA uses a finite volume formulation and the discretization is second order accurate in space (central) and time (backward). Details about the SOWFA software can be found in Ref. [97]. A two-step solution procedure is used. In the first (precursor) step, the turbines are removed and turbulent flow in the domain (the ABL) is simulated using periodic boundary conditions in the streamwise and cross-stream directions; the flow is driven by an adjustable pressure gradient. After the solution reaches a statistically stationary state, time-accurate data is sampled at every time step on the inlet plane(s) of the computational domain and stored. This data is specified as a boundary condition for the subsequent windfarm calculations.

Viscous effects are negligible everywhere except near surfaces (ground, in the present case) due to the high Reynolds number in ABL flows. Energy containing eddies near the ground can become very small, and resolving such small scales can lead to exorbitant grid sizes. Surface flux models for stress and heat (see e.g., Moeng [98]) are therefore usually used in wind-farm computations. Moeng's models require as input the surface roughness height, h_0, the horizontally-averaged surface heat flux, q_s, and a measure of the horizontally-averaged shear stress specified as friction velocity, u_*. While h_0 and q_s are directly specified (from estimates in literature for different surfaces - sea, grasslands, forest, etc.), u_* is approximated using the Monin-Obhukhov similarity theory [99].

Lee *et al.* [100] coupled the LES solver for windfarm aerodynamics, SOWFA with the structural dynamics solver in the FAST (Fatigue, Aerodynamics, Structures, and Turbulence) code [101] to enable calculation of fatigue loads due to atmospheric and wake turbulence. Through this coupling, the simplified aerodynamics module (including the turbulent inflow model) in FAST is replaced by LES, which provides much higher fidelity in resolving the flow. Since the focus of this paper is limited to aerodynamic performance and loads, and not aeroelasiticity, the turbine is idealized by assuming the rotor blades to be infinitely stiff. Structural dynamics can have a significant effect on blade/turbine/tower loads and hence the

present *loads* analysis is only a preliminary investigation. In order to avoid confounding effects from the controller, the turbine is assumed to operate at a fixed, user-specified rotation rate. The turbine RPM and incoming mean wind speed are set to achieve the design tip speed ratio. The instantaneous tip speed ratio fluctuates with the incoming turbulent wind.

2.2.1 Validation

The SOWFA solver is first validated against experimental data for the three-bladed, stall-controlled, 100 kW Tellus turbine (measurement data from Ref. [102]). This turbine is referred to as Risø turbine in Ref. [102]. The turbine rotor diameter is 19 m and its blade chord and twist distributions are shown in Fig. 2.2 (a). Figure 2.2 (b) compares LES predictions of the power curve against measured data as well as against blade element momentum (BEM) theory predictions. Stall-controlled turbines run at a fixed rotational velocity. Above a certain wind speed corresponding to rated power, they begin to stall to reduce power generation. This turbine stalls for wind speeds greater than 12 m/s. It is well known that spanwise flow alleviates stall in 3D blades and allows the blade to operate at higher angles of attack than a 2D blade would. This alleviation of stall cannot be simulated with the actuator line method. Stall-corrected 2-D polars can be used to partly address this weakness of the model, but it was not pursued here as the focus is on evaluating DRWT performance at the design condition. Therefore, the comparison in Fig. 2.2 (b) is limited to pre-stall operation.
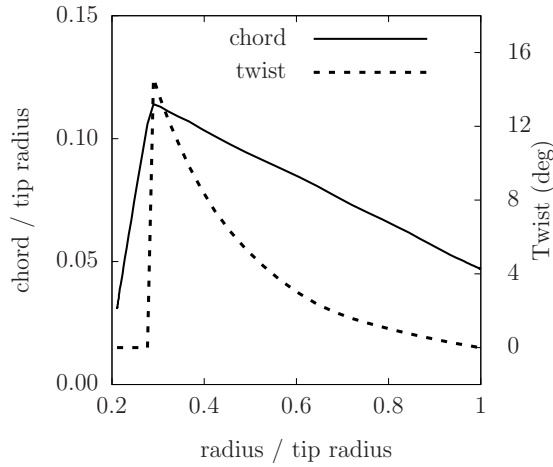
(a) Turbine geometry
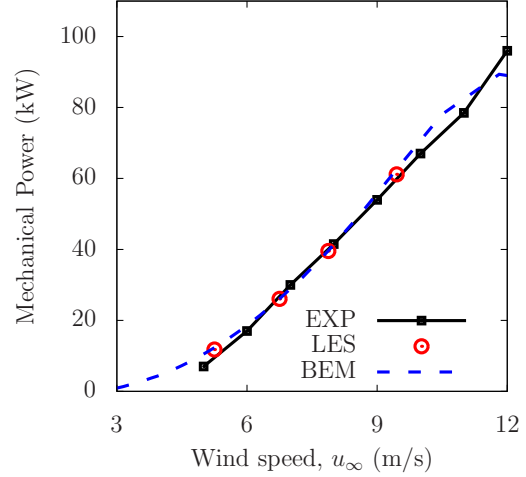
(b) Power curve

Figure 2.2: Verification of LES predicted results for the Tellus (Risø) turbine. (a) non-dimensional rotor blade chord and twist variation, and (b) power curve variation with wind speed compared against data and BEM.

Comparisons of radial distributions of sectional torque (tangential) force coefficient, c_{τ_F} between the predictions made by LES and BEM theory methods for two rotor tip speed ratios, $\lambda = \Omega\, r_{tip}/u_\infty = 6.0$ and 7.0, (close to the design λ) are presented in Fig. 2.3. c_{τ_F} is the non-dimensional aerodynamic force on a blade section that generates torque and is defined as

$$c_{\tau_F} = \frac{F_\tau}{0.5\,\rho\,u_{rel}^2\,c} = c_l \sin(\phi) - c_d \cos(\phi), \tag{2.2}$$

where F_τ is the component of the net aerodynamic force (per unit length) in the plane of rotor rotation, ρ is the fluid density, u_{rel} is blade relative flow velocity, c is section blade chord, c_l and c_d are section lift and drag coefficients respectively, and ϕ is the angle that the blade relative velocity vector makes with the plane of rotor rotation. The agreement between the two solvers is very good except very near the point where the blade cross-section abruptly transitions from an airfoil shape to a cylinder (around $0.3\times$ the tip radius). The differences between the two models emanate from the different blade discretization and interpolation used to calculate sectional airfoil properties (chord, twist, and polars), and are magnified at the geometric transition point.
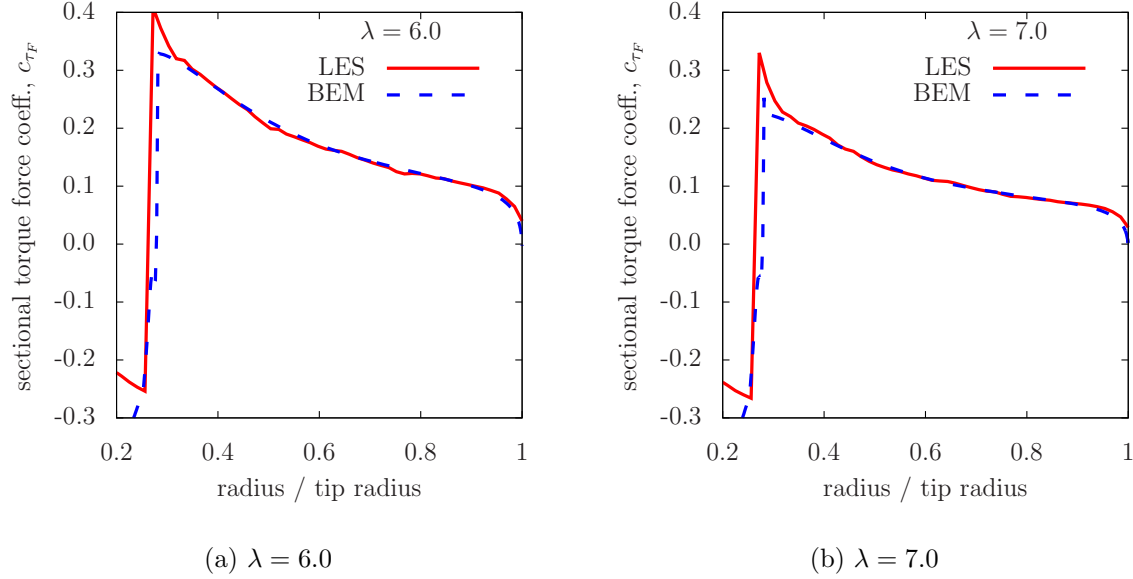
Figure 2.3: Radial variation of sectional torque force coefficient, c_{τ_F} compared between LES and BEM theory predictions at (a) $\lambda = 6.0$ and (b) $\lambda = 7.0$.

2.3 Computational Setup

A two-step approach is used for the numerical predictions. The atmospheric boundary layer (ABL) flow is computed first on one grid and then the flow around the wind turbine is computed on another, more refined grid. Investigations are conducted for uniform inflow and two atmospheric stability conditions: (1) neutral, and (2) stable. In the simulations presented here, the wind blows from the South-West; the wind direction is 240 degrees (measured clockwise) from the North such that the West and the South boundaries of the computational domains are inlet while the East and the North boundaries are outlet (see Fig. 3.1).

Three coordinate systems are utilized in this study. A frame of reference attached to the ground, described by unit vectors $\hat{e}_{\tilde{x}}, \hat{e}_{\tilde{y}}, \hat{e}_z$, is utilized for the CFD calculations. The freestream wind blows at an angle $\phi = 30^o$ to $\hat{e}_{\tilde{x}}$. A new coordinate system with its x-axis aligned with the flow direction is therefore defined by the unit vectors $\hat{e}_x, \hat{e}_y, \hat{e}_z$, where $\hat{e}_{\tilde{x}}.\hat{e}_x = \cos(30^o)$. Lastly, a cylindrical coordinate system, with its axis aligned with $\hat{e}_x$ is used to compute momentum and energy entrainment into the turbine wake layer (see Section 2.4.2.3). This coordinate system is defined by the unit vectors $\hat{e}_r, \hat{e}_\theta, \hat{e}_x$. The details are provided in Appendix A.
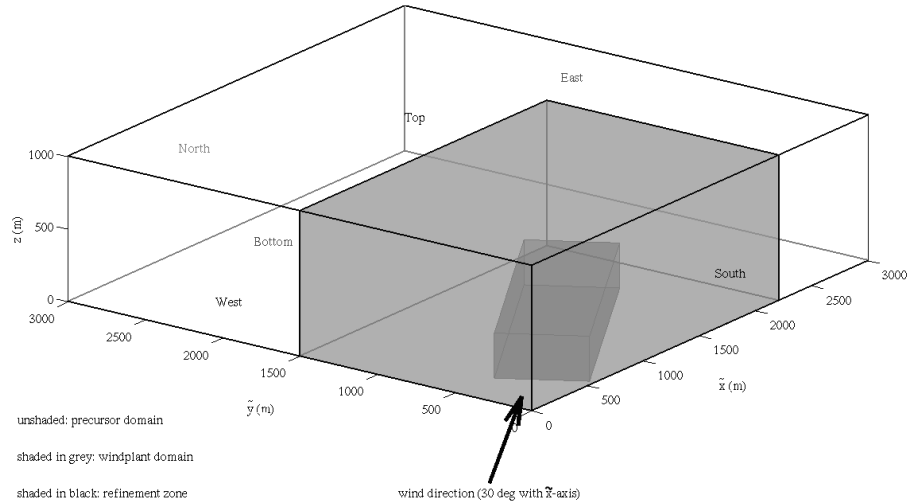
(a) CFD domain for precursor simulations
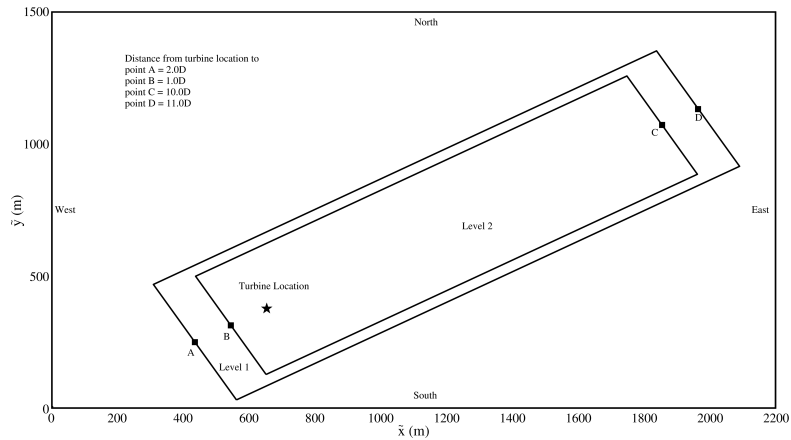
(b) CFD domain for wind turbine simulations

Figure 2.4: A schematic showing the computational domains for the atmospheric boundary layer (precursor) and the main (wind turbine) simulations. The entire box in (a) is the domain for precursor calculations; shaded are shows the smaller domain for wind turbine calculations. In (b), points A-D are lateral midpoints of the rectangular refinement zones.

The atmospheric boundary layer (ABL) is developed in a computational domain by performing "precursor" simulations. A precursor calculation simulates an infinitely long domain in the horizontal directions (the Earth surface) by using cyclic boundary conditions. The intent here is to create steady state ABLs under different stability conditions and not to capture the transient effect caused by the diurnal or seasonal variation of the ABL. Wall models by

Moeng [98] are used to estimate the surface stresses (viscous and SGS) and temperature flux at the bottom boundary. The aerodynamic surface roughness is $h_0 = 0.1$ m, which is a typical value for a terrain with low crops and occasional large obstacles [103]. The top boundary is at 1 km, which is many diameters away from the turbine. The velocity normal to the boundary is set to zero. The pressure boundary condition is zero-gradient and temperature gradient is specified to be 0.003 K/m at the top boundary. Temperature inversion is applied in the domain with the width of 100 m. The temperature at the bottom of the inversion layer is 300 K and at its top is 308 K. Above the inversion layer, the temperature gradient is 0.003 K/m. The inlet is on the South and the West boundaries and a zero pressure gradient boundary condition to simulate outlet conditions is applied on the North and the East boundaries.

Since the objective of the precursor simulations is to establish a fully-developed atmospheric boundary layer flow, wind turbines are excluded from these simulations. The flow is driven by a pressure gradient which is adjusted to achieve the desired flow speed at the turbine hub height. Random perturbations are applied to the flow initially to trip the boundary layer. Precursor simulations are carried out for a long enough time (5 hours of simulation time) to achieve statistical stationarity. With the mean flow speed at the turbine hub height set at 8 m/s, it takes about 9 minutes of simulation time for the flow to cross the computational domain from the inlet to the exit. In 5 hours of simulation time, the flow cycles the domain approximately 34 times, which is sufficient to achieve a fully developed ABL.

Time accurate flow data sampling is initiated at the inlet boundaries after reaching a statistical stationary state (at $t = 5.0$ hours). Sampling is performed for $1,000$ seconds of simulation time, which is the total simulation time for the wind turbine calculations. This time-accurate flow data is prescribed as an inflow boundary condition in the wind turbine simulation. This is one approach to prescribe time-accurate inflow boundary conditions. Another approach is to use synthesized turbulence, where the time-accurate flow information can be constructed using analytical models of turbulence spectra (e.g., Kaimal, von Karman, etc.) [104]. Once statistical stationarity is reached (at $t = 5.0$ hours), the entire flow field from the precursor simulation is also stored and used to initialize the flow in the wind turbine simulations.

Each wind turbine simulation starts at $t = 5.0$ hours and a total of $1,000$ seconds of flow is simulated. The initial and inlet boundary conditions are prescribed using the precursor simulation data as described above. The computational domains for precursor and wind turbine simulations need not be identical. On the contrary, it is desirable to make the domain of the precursor calculation considerably larger than the domain for the wind turbine simulation to account for the length scale disparity between the physical phenomena of interest in these simulations. In the precursor simulations, the energy containing turbulent eddy size can be of the order of a kilometer (planetary boundary layer height), while in the wind turbine simulation, the flow physics of interest is turbine wake for which the relevant length scale is of the order of the turbine diameter (~ 100 m for utility scale turbines).

A shorter domain is used for wind turbine simulations in comparison with precursor simulations to allow for higher spatial resolution of the turbine wakes. As seen in Fig. 3.1, the precursor runs are performed on a computational domain with dimensions 3 km $\times$ 3 km $\times$ 1 km. The domain is discretized into $288 \times 288 \times 100$ hexahedral cells. The precursor simulations are performed in parallel on 128 cores and each run takes about 50 hours of wall-clock time. The wind turbine runs are performed on a domain of size 2.2 km $\times$ 1.5 km $\times$ 1 km that is discretized into $220 \times 150 \times 100$ hexahedral cells. Two levels of mesh refinement are used in the vicinity of- and downstream of the wind turbine. Each grid cell in a refinement block is split into half along each direction (i.e., it is divided into 8 cells). In the refined block, the cell size is 2.5 m in each direction. The final mesh has a total of about 14 M cells. The *blockMesh* utility in OpenFoam is used to generate the computational meshes. It takes approximately 120 hours of wall-clock time to simulate $1,000$ seconds of flow in each wind turbine simulation using 128 cores in parallel. Figure 3.1 (b) shows the turbine location in the computational domain as well as the topology of the refinement zones.

LES simulations are carried out using the optimum DRWT identified in Rosenberg *et al.*[1]. The non-dimensional chord and twist distributions of the main and secondary rotors of the DRWT are shown in Fig. 2.5. The blade chord (c) and radius (r) are nondimensionalized by the respective rotor tip radii. To enable direct comparisons, simulations are also performed for a conventional single rotor wind turbine (SRWT), which is the conceptual NREL 5MW

offshore reference turbine [75]. The NREL 5 MW turbine rotor is used as the primary rotor of the DRWT.

(a) Primary rotor   (b) Secondary rotor
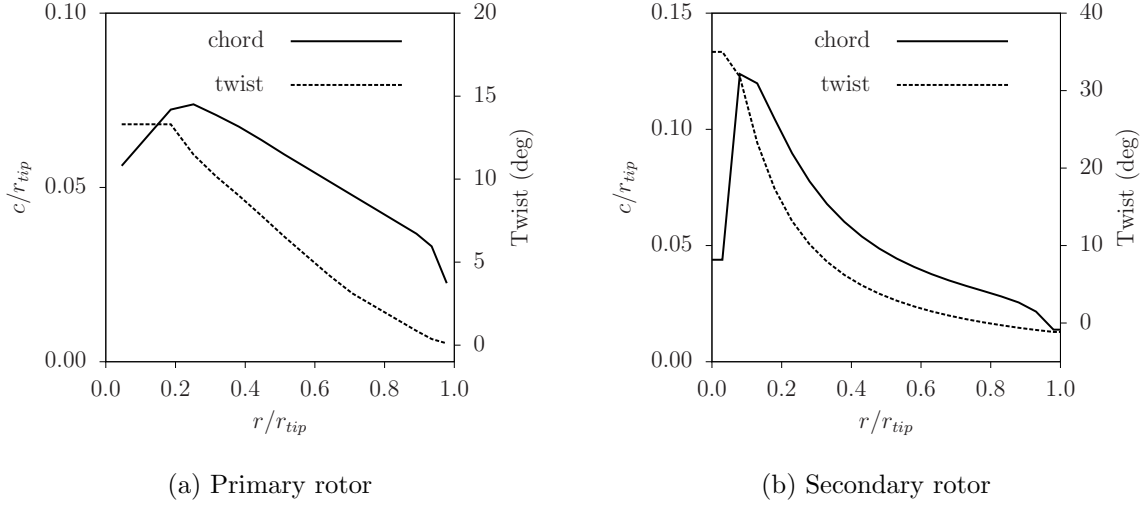
Figure 2.5: Radial distributions of the (a) primary and (b) secondary rotor blade chord and twist of the DRWT configuration analyzed here.

2.4   Results and Discussion

The objectives of the DRWT technology by Rosenberg *et al.* [1] are twofold: (1) minimize root losses, and (2) increase entrainment from the upper atmosphere into the turbine wake. An increase in C_P between 5-7% through root loss mitigation was already demonstrated for uniform inflow calculations in Rosenberg *et al.* [1]. Here we analyze the effect of the atmospheric boundary layer (ABL) on blade root loss, wake mixing, and aerodynamic loads.

2.4.1   Atmospheric Boundary Layer

The precursor (ABL) simulations are analyzed first. The simulated flow data is averaged in time and space (along the horizontal directions) to obtain mean velocity profiles for both the neutral and stable ABL conditions. A pressure gradient along the flow direction is imposed and is continually adjusted until the desired mean flow speed ($\overline{u}_{\infty,h} = 8$ m/s for the simulations here) is achieved at the turbine hub height. The atmospheric stability is varied between different simulations by changing the heat flux through the bottom boundary. Zero net heat flux is

prescribed for the neutral ABL simulation, while a value of -0.4 K.m/s is used to simulate the stable ABL condition. A negative value implies heat flux out of the computational domain.

Figure 2.6 (a) plots the normalized mean velocity profiles for two ABL simulations; the freestream mean wind speed at the turbine hub height ($\bar{u}_{\infty,h}$) is used for the normalization. The uniform flow case does not require a precursor simulation - a uniform wind speed of 8 m/s with zero inflow turbulence is used for that case. As expected, the vertical shear in the mean wind speed near the ground in the stable case is much higher than in the neutral case. Figure 2.6 (b) compares the streamwise turbulence intensity, defined as $\sigma_{u_x}/u_{\infty,h} = (\overline{u_x^2} - \bar{u}_x^2)^{\frac{1}{2}}/\bar{u}_{\infty,h}$, where u_x is the streamwise component of the wind velocity. Equation A.1 is used to calculate streamwise turbulence intensity from the computed Reynolds stress. In both ABL cases, the streamwise turbulence intensity decreases with height across the turbine rotor. At the hub height, the streamwise turbulence intensity ($\sigma_{u_x}/u_{\infty,h}$) is about 6% for the stable ABL case and about 10% for the neutral ABL case. Note that these values would be higher if the local mean wind speed at the turbine hub height was used rather than the corresponding freestream value. Stable stratification suppresses atmospheric turbulence and hence the streamwise turbulence intensity is less for the stable ABL case compared to the neutral case.

(a) Mean velocity, $\langle \overline{u}_x \rangle / \overline{u}_{\infty,h}$ (b) Turbulence intensity, $\sigma_{u_x} / \overline{u}_{\infty,h}$
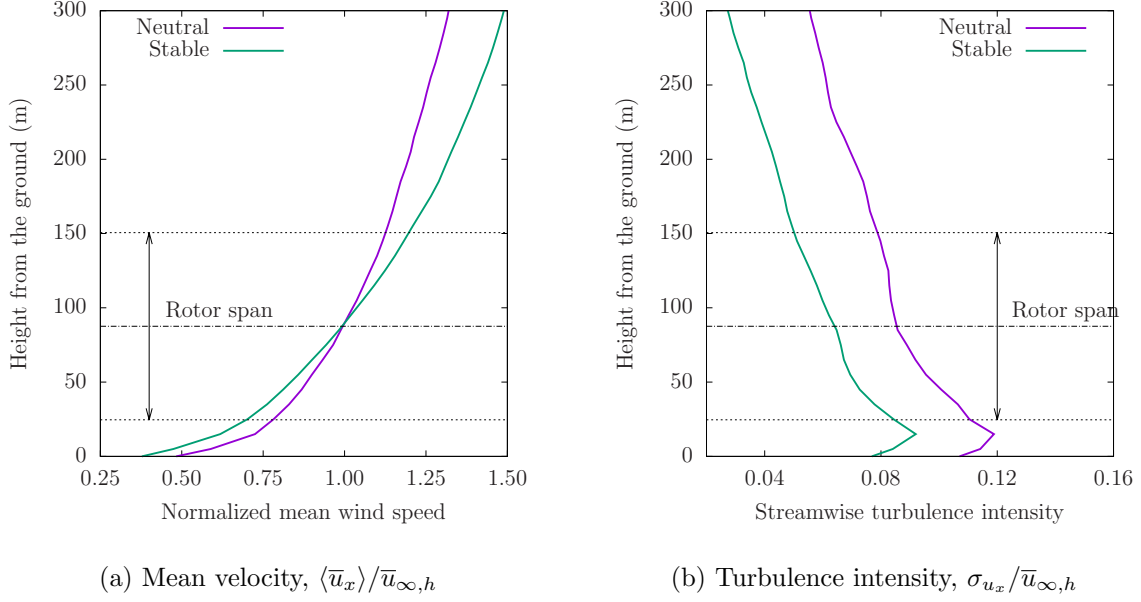
Figure 2.6: Time averaged streamwise wind speed and streamwise turbulence intensity profiles for the two ABL conditions simulated. The mean wind speed is $\overline{u}_{\infty,h} = 8$ m/s. The turbulence intensity is zero for the uniform inflow case.

Atmospheric boundary layer stability is characterized by the Richardson number, which can be written as

$$Ri = \frac{g}{T} \frac{(\Delta\theta/\Delta z)}{(\Delta u/\Delta z)^2} = \frac{z/L\phi_h}{\phi_m^2}, \tag{2.3}$$

where z is height from the ground, θ is potential temperature, u is flow speed, L is the Obukhov Length and ϕ_m and ϕ_h are nondimensional temperature and wind profiles, respectively. For $z/L \geq 0$, $\phi_h = 0.74 + 4.7z/L$ and $\phi_m = 1 + 4.7z/L$. z is set as 50 m for the ABL calculation of the Richardson number [105, 106]. For neutral stability, $L \to \infty$ and $Ri \to 0$. For the stable condition simulated, $Ri = 0.125$, which falls in the "slightly stable" category according to the classification of atmospheric stability by Sedefian and Bennett [105]. They collected meteorological data over a year at a site in Staten Island, NY. They categorized all the possible ABL stability conditions into seven groups, ranging from strongly unstable to strongly stable ABL. As they reported, neutral- and slightly stable atmosphere (as characterized by Ri using Eq. 2.3) were observed for 31.1% and 12.3% of the time respectively. Due to their high probability of occurrence in the field, these two stability conditions were selected for the simulations.

2.4.2 Aerodynamic Performance

The aerodynamic performance of the DRWT design is analyzed and compared against the corresponding SRWT. Analysis is presented for the three inflow conditions described in Section 3.2.2: (a) uniform inflow, (b) slightly stable ABL, and (c) neutral ABL. The emphasis is on evaluating the ability of the DRWT to mitigate blade root loss and wake loss.

Figure 2.7 visualizes the flow field downstream of the SRWT turbine operating in a neutral ABL. The figure is an iso-surface plot, showing surfaces with a constant value of Q-criterion. In a vortex, $Q = 0.5(|\boldsymbol{\Omega}|^2 - |\boldsymbol{S}|^2)$ is greater than 0, where $\boldsymbol{\Omega}$ and $\boldsymbol{S}$ are vorticity and rate-of-strain tensors respectively, and $|\boldsymbol{T}|$ denotes the Euclidean norm of the tensor $\boldsymbol{T}$. The tip and hub vortices can be seen in the near-wake region, but quickly disintegrate in one to two rotor revolutions due to the high atmospheric turbulence. Some structures can be seen underneath the turbine, which correspond to the ABL turbulence near the ground.
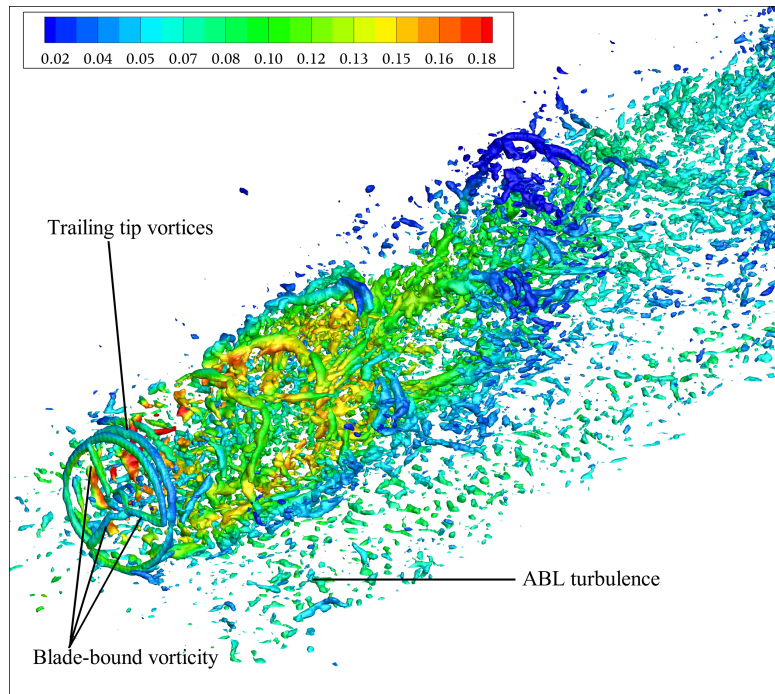
Figure 2.7: Iso-surfaces of Q-criterion of the SRWT operating in a neutral ABL. The contours are colored by streamwise turbulence intensity - red and blue showing high and low turbulence intensity levels respectively.

2.4.2.1 Root Loss Mitigation

Airfoils in the root region (approximately inner 25%) of conventional turbine blades have very high thickness-to-chord ratio and thus have poor aerodynamic performance. The smaller secondary rotor in the DRWT proposed by Rosenberg *et al.* [1] aims to mitigate the losses due to the aerodynamically non-optimum root region of the larger primary rotor blades. Since the secondary rotor is much smaller in size compared to the primary rotor, it has significantly lower loads; loads increase in proportion with the cube of rotor diameter. The secondary rotor can therefore be designed using relatively thin, aerodynamically optimized airfoils that are efficient at extracting wind energy passing through the main rotor blade root region.

The C_P of the DRWT is computed as the sum of the powers generated by the two rotors, normalized by the power in the wind going through the main rotor disk area. RANS calculations by Rosenberg *et al.* [1] showed an increase in C_P of about 7% with the DRWT. The results from the LES simulations for the three inflow conditions, conducted as a part of this study, corroborate the findings of Rosenberg *et al.* [1]. The DRWT outperforms the conventional SRWT for all inflow conditions in terms of time-averaged power produced, demonstrating the 'root loss mitigation' ability of the DRWT. There is also a marginal reduction in the time-averaged out-of-plane blade root bending moment (M_{OOP}) of the primary rotor of the DRWT. A summary of these results is presented in Table 2.1. The percentage differences in the table are calculated as $100\times$(DRWT-SRWT)/SRWT. The largest increase in power is observed for the neutral ABL condition and smallest for the uniform inflow case.

Table 2.1: Percentage difference in time-averaged turbine C_P and M_{OOP}.

Case	%ΔPower	%ΔM_{OOP}
Uniform inflow	5.0	-0.39
Stable ABL	5.4	-0.29
Neutral ABL	6.1	-0.07

2.4.2.2 Turbine Wake Mixing

Comparative wake mixing analyses are performed for the DRWT and SRWT to investigate the ability of the DRWT to reduce wake loss. The setup and inflow boundary condition for the neutral and stable cases are described in Section 3.2.2. For the uniform inflow simulation, the precursor run is not required and a uniform wind velocity and zero turbulence intensity are specified at the inlet boundaries. The flow angle is kept the same (30 degrees w.r.t. $\hat{e}_{\tilde{x}}$) as for the two ABL cases.

Meanflow Time-averaged velocities in turbine wakes are compared first. Averaging is performed over 110 revolutions of the main rotor. Large scale eddies in atmospheric turbulence contain significant energy at frequencies much lower than rotor passing frequency, hence averaging over a long time (in comparison with the rotor rotation period) is required. Contours of mean streamwise velocity are plotted on an x-z plane in the streamwise direction (see subplots 'a' and 'b' in Figs. 2.8, 2.9, & 2.10), and on $y - z$ planes in the cross-stream direction at four downstream locations: $2D$, $4D$, $6D$, and $8D$, where D is the main rotor diameter (see subplots 'c' and 'd' in Figs. 2.8, 2.9, & 2.10). The cross-stream contour plots are drawn over disks of diameter 1.4 times the turbine rotor diameter such that the top of each disk corresponds to the 12 o'clock position of the rotor and the bottom to the 6 o'clock position; the view is looking from downstream (but at an angle, so the disks look oval and not circular) and the main turbine rotor is rotating in the counter-clockwise in the figures. The path traced by the rotor tip is marked with the dashed curves. For a more quantitative comparison, streamwise velocity is azimuthally (circumferentially) averaged; averaging denoted by angle brackets as $\langle \bar{u}_x \rangle$. Radial profiles of $\langle \bar{u}_x \rangle$, normalized by $\bar{u}_{\infty,h}$, are compared between the SRWT and the DRWT in the wake region (see e.g., Fig. 2.8 e).
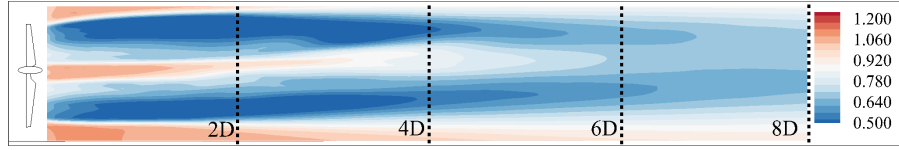
(a) SRWT: $\overline{u}_x/\overline{u}_{\infty,h}$ contours (Uniform)
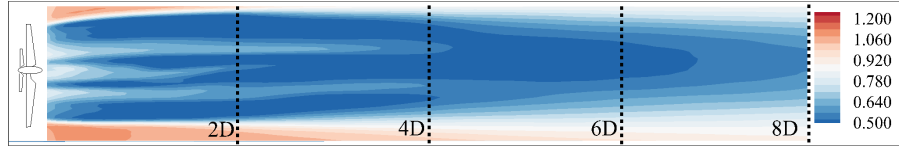
(b) DRWT: $\overline{u}_x/\overline{u}_{\infty,h}$ contours (Uniform)
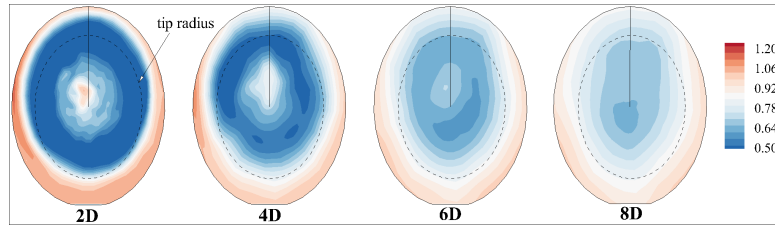
(c) SRWT: $\overline{u}_x/\overline{u}_{\infty,h}$ contours (Uniform)
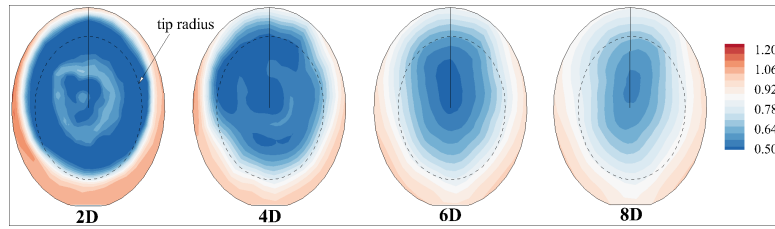
(d) DRWT: $\overline{u}_x/\overline{u}_{\infty,h}$ contours (Uniform)
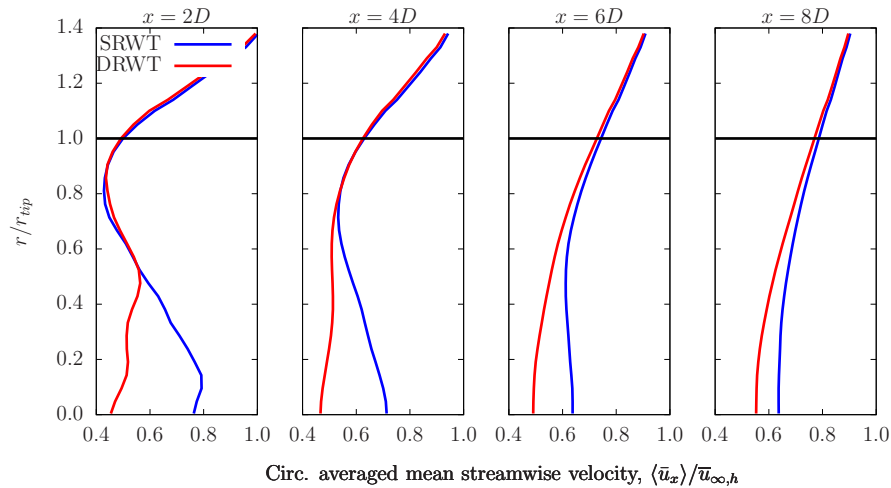
(e) $\langle\overline{u}_x\rangle/\overline{u}_{\infty,h}$ (Uniform)

Figure 2.8: Comparison between SRWT and DRWT of normalized mean streamwise velocity, $\overline{u}_x/u_{\infty,h}$: (a,b) on the x-z plane passing through the rotor hub, and (c,d) on cross-stream (y-z) planes, and (e) circumferentially averaged values at four downstream locations ($x/D = 2, 4, 6,$ & 8) for the **uniform** inflow condition.

31

Figure 2.8 compares the SRWT and DRWT designs for the uniform inflow case. Large differences in mean velocities near the center of the disks are evident up to 8D downstream of the rotor. The SRWT is not effective at extracting energy from the wind in the blade root region, and hence the wind flows through there unharvested. In contrast, the secondary rotor of the DRWT efficiently extracts the energy from this streamtube and hence leaves a larger momentum (velocity) deficit in the wake. Reduced values of $\langle \bar{u}_x \rangle / \bar{u}_{\infty,h}$ are therefore observed in the wake of the DRWT as compared to SRWT for $r/r_{tip} < 0.4$. This deficit reduces with downstream distance due to enhanced wake mixing in the DRWT. The circumferentially averaged plots show that by 8D downstream, the difference in the velocity (and hence kinetic energy) deficit between the DRWT and SRWT is considerably reduced. Also noted in the uniform inflow case is the slight flow acceleration near the ground under the turbines, which occurs due to the contraction of the streamtube caused by the slip wall boundary condition imposed on the ground. As a result, the wake deficit shifts up and away from the ground as it convects downstream (see Fig. 2.8).

The addition of the atmospheric boundary layer (ABL) considerably changes the turbine performance and wake dynamics. The wall shear reduces the velocity near the ground. Hence, the acceleration effect observed in the uniform inflow case – due to streamtube contraction – is not observed in the ABL cases. The effect of wake rotation is evident in the ABL cases as seen by the azimuthal locations of highest mean velocity in subplots (c) and (d) of Figs. 2.9 and 2.10. The main rotors of the turbines are rotating in the counter-clockwise direction as seen from downstream and the turbine wake rotates in the opposite (clockwise) direction. As the wake rotates, it pulls the higher momentum fluid from above (12 o'clock position) down and to the right in the figure (clockwise). Wake rotation also pulls the low momentum fluid in the boundary layer near the ground, up and to the left in the figures.
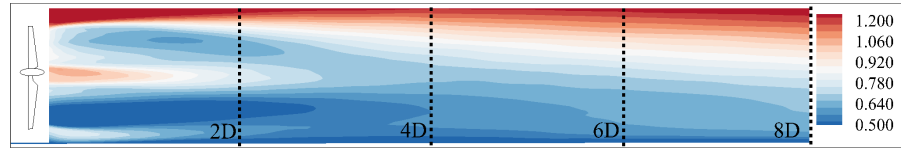
(a) SRWT: $\overline{u}_x/\overline{u}_{\infty,h}$ contours (Stable)

(b) DRWT: $\overline{u}_x/\overline{u}_{\infty,h}$ contours (Stable)

(c) SRWT: $\overline{u}_x/\overline{u}_{\infty,h}$ contours (Stable)

(d) DRWT: $\overline{u}_x/\overline{u}_{\infty,h}$ contours (Stable)
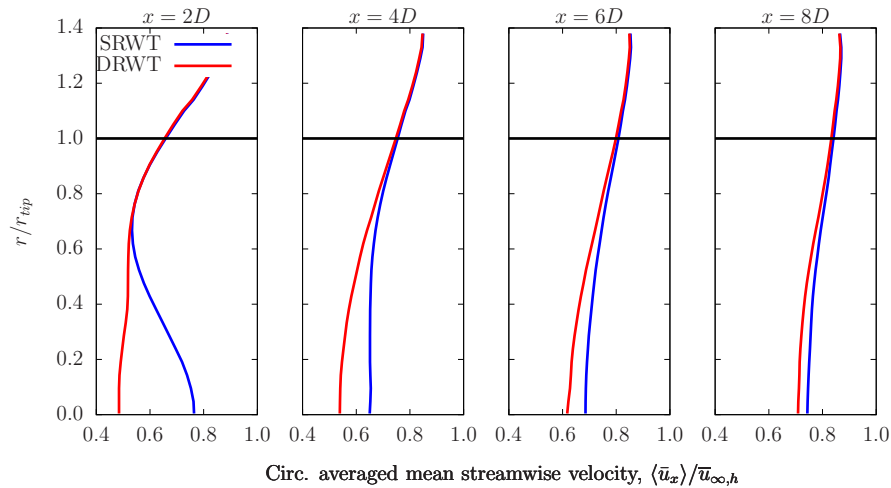
(e) $\langle \overline{u}_x \rangle/\overline{u}_{\infty,h}$ (Stable)

Figure 2.9: Comparison between SRWT and DRWT of normalized mean streamwise velocity, $\overline{u}_x/u_{\infty,h}$: (a,b) on the x-z plane passing through the rotor hub, and (c,d) on cross-stream (y-z) planes, and (e) circumferentially averaged values at four downstream locations ($x/D = 2, 4, 6, \&\ 8$) for the **stable** ABL condition.

(a) SRWT: $\overline{u}_x/\overline{u}_{\infty,h}$ contours (Neutral)

(b) DRWT: $\overline{u}_x/\overline{u}_{\infty,h}$ contours (Neutral)
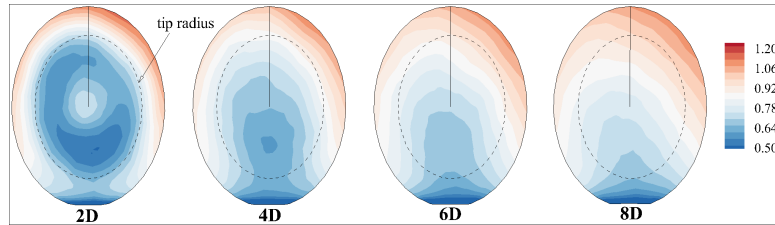
(c) SRWT: $\overline{u}_x/\overline{u}_{\infty,h}$ contours (Neutral)
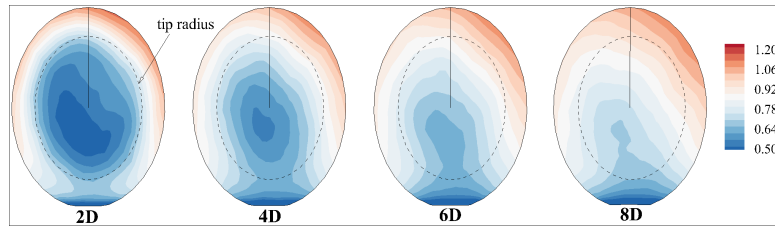
(d) DRWT: $\overline{u}_x/\overline{u}_{\infty,h}$ contours (Neutral)
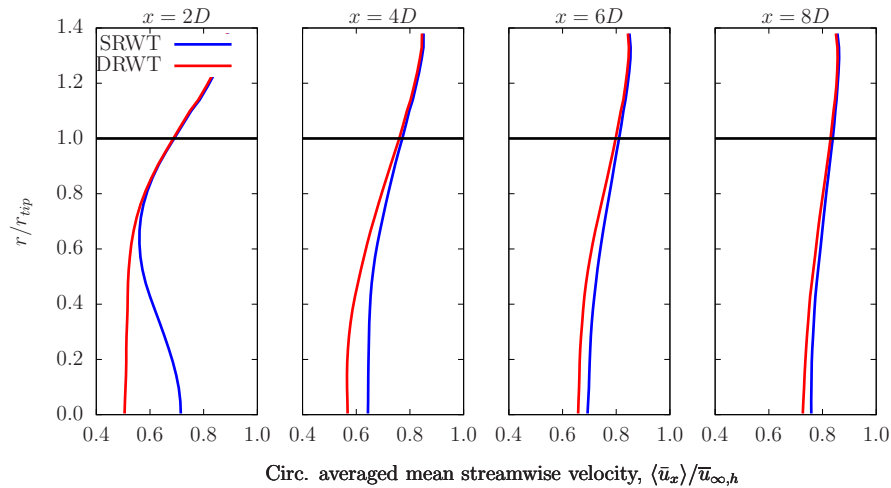
(e) $\langle\overline{u}_x\rangle/\overline{u}_{\infty,h}$ (Neutral)

Figure 2.10: Comparison between SRWT and DRWT of normalized mean streamwise velocity, $\overline{u}_x/u_{\infty,h}$: (a,b) on the x-z plane passing through the rotor hub, and (c,d) on cross-stream (y-z) planes, and (e) circumferentially averaged values at four downstream locations ($x/D = 2, 4, 6,$ & 8) for the **neutral** ABL condition.

The primary mechanism of wake mixing is turbulent momentum transport across the turbine wake layer, which is proportional to the turbulence level in the incoming wind. Higher turbulence intensity in incoming flow therefore leads to higher wake mixing rate. The turbulence in the ABL enhances wake mixing and hence the velocity deficits in the wakes are reduced for the two ABL cases in comparison with the uniform inflow case. The wake deficit for either turbine is highest for the uniform flow case and smallest for the neutral ABL case. This behavior of turbine wake mixing rate increasing with inflow turbulence intensity, has been previously observed both experimentally [107] and numerically [108] for conventional, single-rotor turbines.

The interesting observation in the present study is that the *difference* in the velocity deficits between the SRWT and DRWT also reduces faster for the ABL cases when compared to the uniform flow case; the difference is negligible by 8D downstream (compare subplot 'e' in Figs. 2.9 & 2.10 with Fig. 2.8). This suggests that the presence of atmospheric turbulence enhances the wake mixing rate of the DRWT more than that of the SRWT. The increase in wake mixing rate is due to the ABL turbulence augmenting the interaction between the trailing wake/vortex systems of the two rotors of the DRWT; this interaction leads to increased turbulent momentum transport into the turbine wake layer, as shown later in Section 2.4.2.3. The largest increase in wake mixing rate is observed for the neutral ABL case (Fig. 2.10).

It should be noted that the secondary rotor of the DRWT used here is not specifically designed or operated to target wake mixing. The results obtained here, of enhanced wake mixing rate with a DRWT, indicate that the technology has potential to reduce wake losses if its design and operation are optimized for that purpose. Also, it is observed that even with the *de facto* design/operation of the DRWT, the additional wake deficit due to the secondary rotor of the DRWT is sufficiently mixed out such that it will not adversely impact the performance of the immediately downstream turbine if it is placed at least 8D away. Therefore the gains achieved by mitigating root losses for isolated turbines will be realized in array configurations (windfarms) as well.

Turbulence Intensity Mechanical turbulence, generated due to mean velocity shear in turbine wake and tip vortices, is an important contributor to wake mixing. Streamwise turbulence intensities in the wakes are therefore compared between the DRWT and SRWT configurations for the three inflow conditions in Figs. 2.11, 2.12, and 2.13. In all three cases, streamwise turbulence intensity near the turbine hub height is higher for the SRWT until about $4D$ downstream of the turbine. This is because of two reasons: (1) due to the "leakage" of high-momentum fluid through the blade root region, a higher velocity shear is present in the wake of the SRWT than that of the DRWT; compare e.g., subplots (a) and (b) in Fig. 2.8. Mean velocity shear is a source of turbulence. Hence, there is higher shear-generated turbulence in the wake of the SRWT near the turbine hub height up to $4D$ downstream of the turbine, and (2) the secondary rotor of the DRWT dampens the large-scale eddies in the incoming ABL flow. This phenomenon of a turbine rotor acting as a damper / high-pass filter has been reported by Chamorro [109] for conventional single rotor wind turbines.

While the SRWT shows higher turbulence intensity in the wake up to about $4D$, the turbulence intensity for the DRWT is higher further downstream for all inflow conditions. This increase in turbulence production in the DRWT for $x > 4D$ is due to the interaction between the trailing wake/vortex systems of the primary and the secondary rotors of the DRWT. The turbulence production mechanism is velocity shear, which is increased by this interaction. Higher turbulence intensity in the wake explains the higher wake mixing rate for the DRWT noted in the previous section. The difference in turbulence intensities between the DRWT and the SRWT is highest for the neutral ABL case (which has the highest ABL turbulence of all the cases simulated), re-emphasizing that atmospheric turbulence promotes interaction of the wake/vortex systems of the two rotors.

While increased turbulence intensity enhances wake mixing rate and therefore boosts wind-farm efficiency, it does have a potential to increase fatigue loading on downstream turbines. This potential issue with the DRWT technology will be addressed in the future. Aerodynamic loads for a DRWT operating in "clean" flow however, are analyzed in Section 2.4.3.
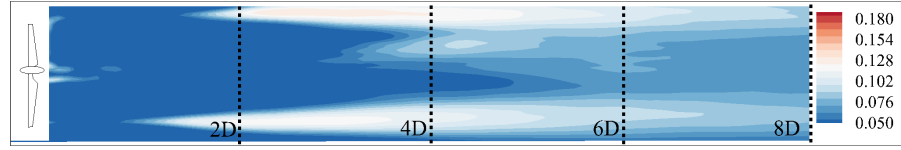
(a) SRWT: $\sigma_{u_x}/\bar{u}_{\infty,h}$ contours (Uniform)
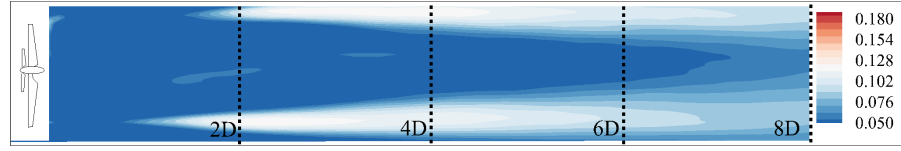
(b) DRWT: $\sigma_{u_x}/\bar{u}_{\infty,h}$ contours (Uniform)
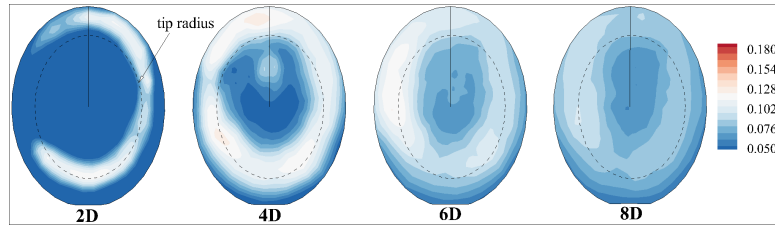
(c) SRWT: $\sigma_{u_x}/\bar{u}_{\infty,h}$ contours (Uniform)
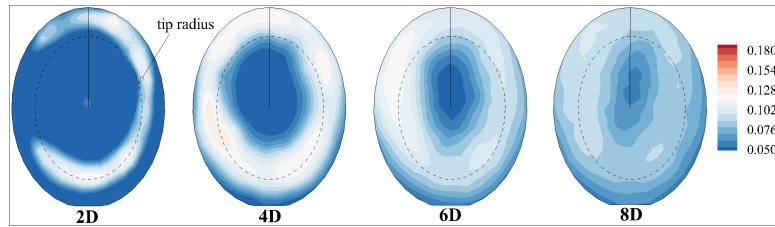
(d) DRWT: $\sigma_{u_x}/\bar{u}_{\infty,h}$ contours (Uniform)
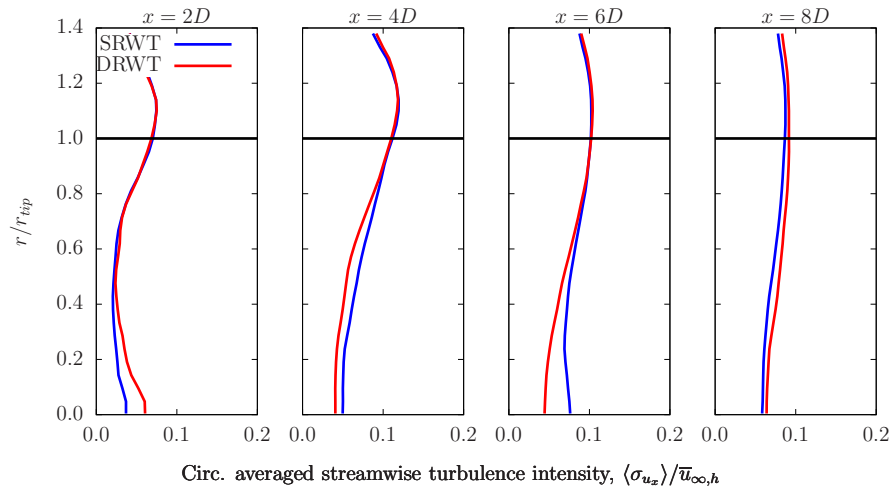
(e) $\langle\sigma_{u_x}\rangle/\bar{u}_{\infty,h}$ contours (Uniform)

Figure 2.11: Comparison between SRWT and DRWT of normalized streamwise turbulence intensity, $\sigma_{u_x}/\bar{u}_{\infty,h}$: (a,b) on the x-z plane passing through the rotor hub, and (c,d) on cross-stream (y-z) planes, and (e) circumferentially averaged values at four downstream locations ($x/D = 2, 4, 6,$ & 8) for the **uniform** inflow condition.
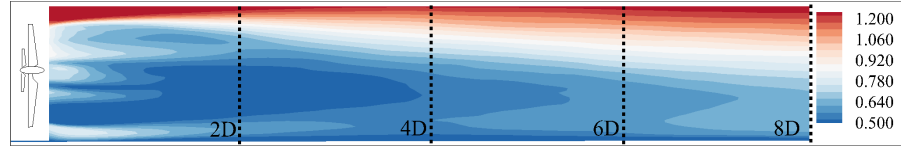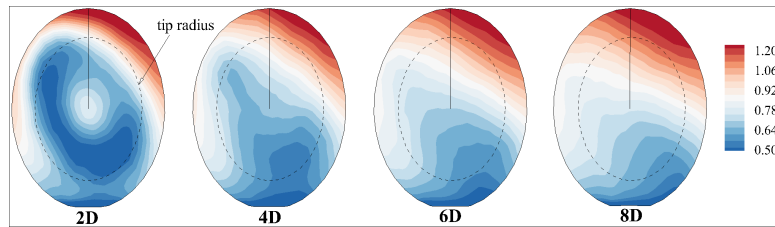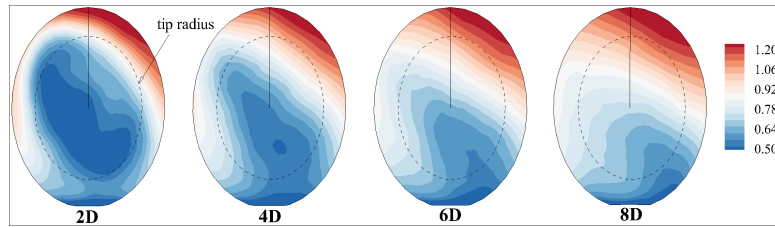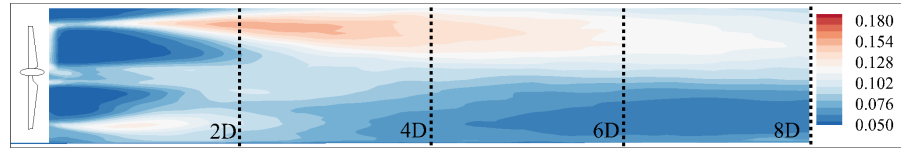
(a) SRWT: $\sigma_{u_x}/\bar{u}_{\infty,h}$ contours (Stable)
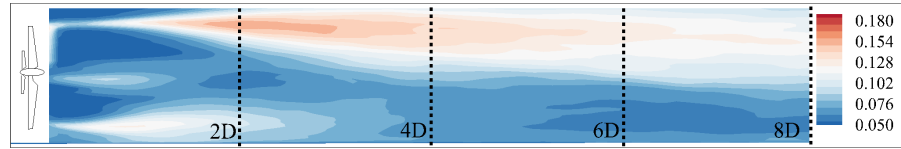
(b) DRWT: $\sigma_{u_x}/\bar{u}_{\infty,h}$ contours (Stable)
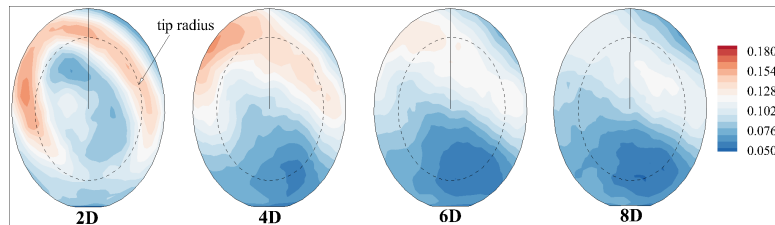
(c) SRWT: $\sigma_{u_x}/\bar{u}_{\infty,h}$ contours (Stable)
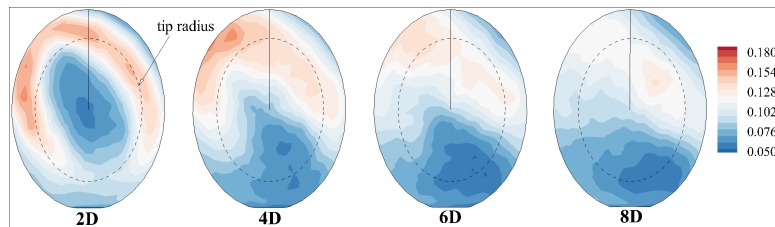
(d) DRWT: $\sigma_{u_x}/\bar{u}_{\infty,h}$ contours (Stable)
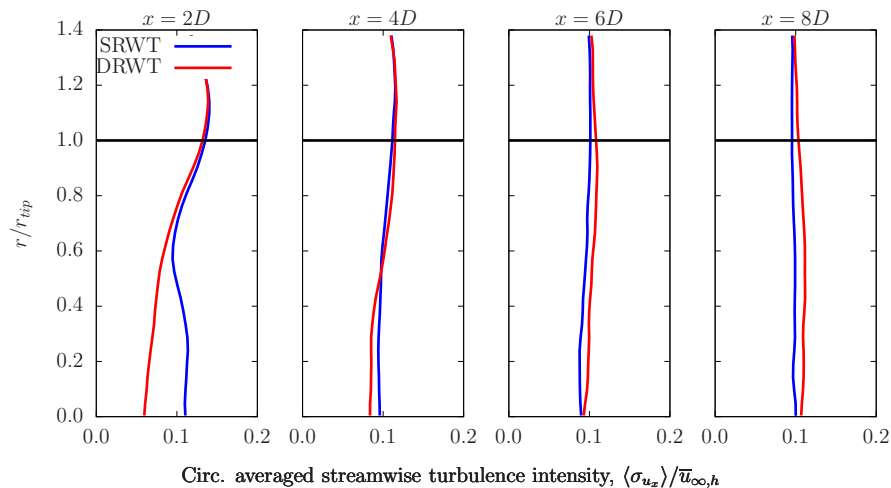
(e) $\langle\sigma_{u_x}\rangle/\bar{u}_{\infty,h}$ contours (Stable)

Figure 2.12: Comparison between SRWT and DRWT of normalized streamwise turbulence intensity, $\sigma_{u_x}/\bar{u}_{\infty,h}$: (a,b) on the x-z plane passing through the rotor hub, and (c,d) on cross-stream (y-z) planes, and (e) circumferentially averaged values at four downstream locations ($x/D = 2, 4, 6,$ & 8) for the **stable** ABL condition.
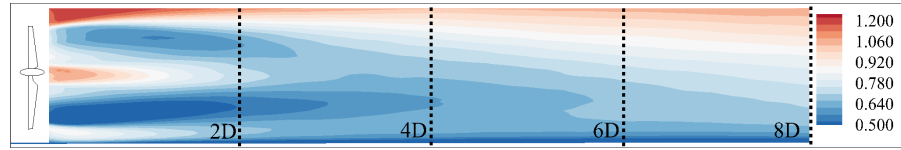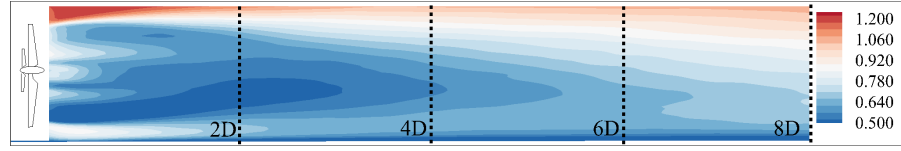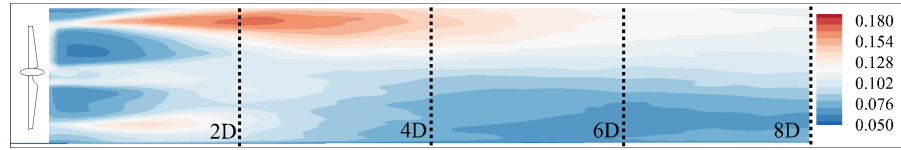
(a) SRWT: $\sigma_{u_x}/\bar{u}_{\infty,h}$ contours (Neutral)
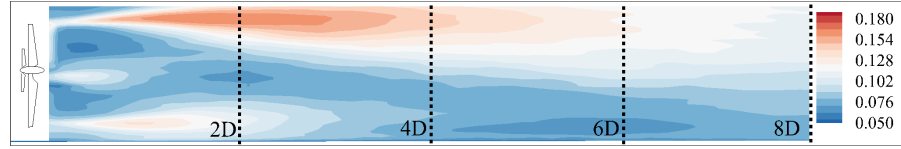
(b) DRWT: $\sigma_{u_x}/\bar{u}_{\infty,h}$ contours (Neutral)
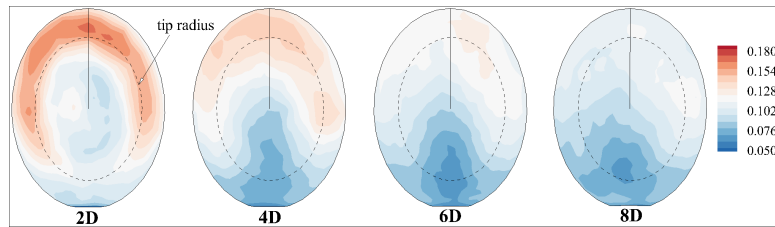
(c) SRWT: $\sigma_{u_x}/\bar{u}_{\infty,h}$ contours (Neutral)
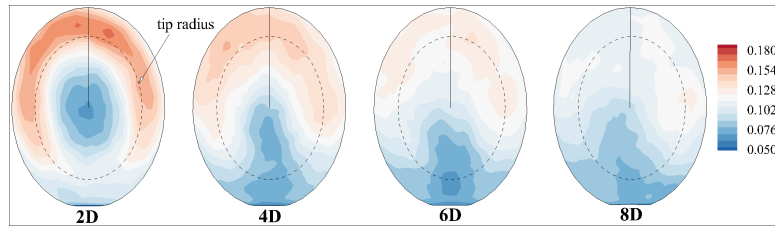
(d) DRWT: $\sigma_{u_x}/\bar{u}_{\infty,h}$ contours (Neutral)
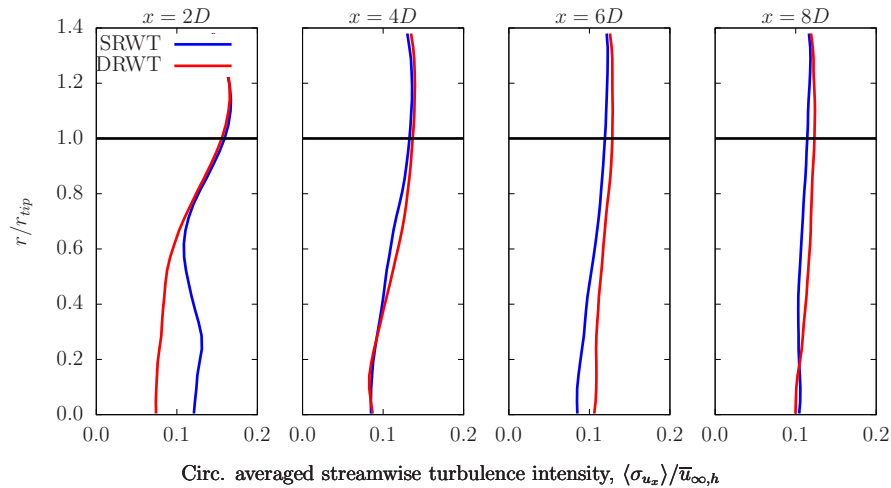
(e) $\langle\sigma_{u_x}\rangle/\bar{u}_{\infty,h}$ contours (Neutral)

Figure 2.13: Comparison between SRWT and DRWT of normalized streamwise turbulence intensity, $\sigma_{u_x}/\bar{u}_{\infty,h}$: (a,b) on the x-z plane passing through the rotor hub, and (c,d) on cross-stream (y-z) planes, and (e) circumferentially averaged values at four downstream locations ($x/D = 2, 4, 6,$ & 8) for the **neutral** ABL condition.

2.4.2.3   Momentum Entrainment

Utility scale turbines in windfarms are typically installed in systematic arrangements (arrays). Wake losses in a windfarm are most severe when the wind direction is aligned with the turbine rows. In such extreme cases, it is meaningful to look into entrainment of high-momentum fluid into the turbine wake layer. For a very large, closely-packed turbine array, the turbine wake layer would be horizontal, stretching vertically from $H - r_{tip}$ to $H + r_{tip}$, where H is the turbine hub height and r_{tip} is the rotor tip radius. For an isolated turbine analysis however, the turbine wake layer is cylindrical, co-axial with the rotor, and has the same diameter as that of the turbine rotor (see Fig. 2.14).

Turbulent transport of momentum from outside the turbine layer has been identified to be the dominant mechanism for re-energizing the flow in large wind turbine arrays [27]. Turbulent momentum flux through the cylindrical turbine wake layer (see Fig. 2.14), is analyzed to compute turbulent momentum and energy transport and investigate wake recharging. The present analysis is performed for a turbine wake layer that extends from the turbine rotor location to $8D$ downstream. Time averaged velocity and Reynolds stress tensor $(\overline{u_i' u_j'})$ are interpolated onto this cylindrical surface using the Tecplot 360 software (www.tecplot.com).

(a) Schematic

(b) Turbine wake layer (cylindrical surface)
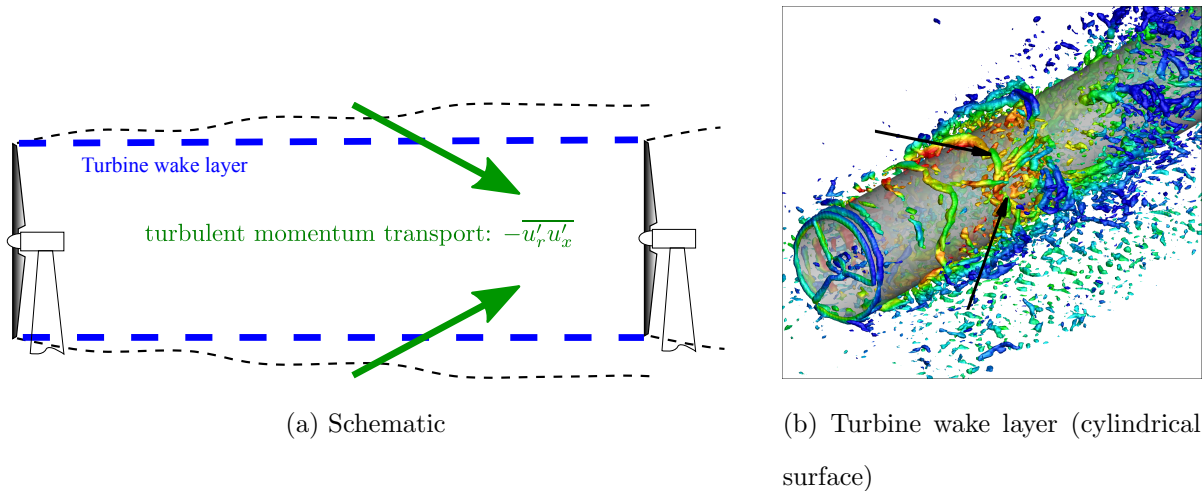
Figure 2.14: Investigation of turbulent momentum transport into the turbine wake layer: (a) a schematic and (b) cylindrical surface showing the turbine wake layer through which turbulent momentum flux is computed to quantify entrainment in turbine wake.

Entrainment of high momentum fluid into this cylinder is induced by turbulent stresses, particularly the stress term $\overline{u_r' u_x'}$, where the subscript 'r' denotes the radial component, the prime denotes a perturbation quantity, and the overline denotes a time-averaged quantity. A cylindrical coordinate system $(\hat{e}_r, \hat{e}_\theta, \hat{e}_x)$ with its axis aligned with the freestream flow direction $\hat{e}_x$ is used (see Appendix A). Equation A.3 relates $\overline{u_r' u_x'}$ to the Reynolds stress tensor computed in the ground frame of reference $(\hat{e}_{\tilde{x}}, \hat{e}_{\tilde{y}}, \hat{e}_z)$. Since $\hat{e}_r$ points radially outward, a negative value of $\overline{u_r' u_x'}$ implies transport *into* the cylinder (turbine wake layer).

Figure 2.15 (a-f) plot the Reynolds stress term $\overline{u_r' u_x'}$ normalized by $u_{\infty,h}^2$ on the unwrapped cylindrical surface that defines the turbine layer. The colormap in the figure is reversed to make intuitive sense - negative values indicate net flux into the cylinder. In the figure, $\theta = 0^o$ corresponds to the 12 o'clock position and $\pm 180^o$ correspond to the 6 o'clock position. It can be noticed that the highest value of $-\overline{u_r' u_x'}$ is not at the 12 o'clock position but skewed about it. This behavior has been noted previously by Wu and Porté Agel [110] although for the stress term $\overline{u_x' u_z'}$. A clear trend of increasing momentum entrainment with increasing ABL turbulence is seen in the figure for both SRWT and DRWT. The x-location where peak entrainment occurs varies both with atmospheric turbulence intensity and azimuthal location. The peak values occur closer to the turbine as inflow turbulence intensity increases (compare subplot 'a' with 'b' & 'c' of Fig. 2.15). This is because the incoming turbulence disintegrates the tip vortex system quickly. For ABL cases, peak $-\overline{u_r' u_x'}$ occurs around 1 rotor diameter downstream of the turbine near the ground ($\theta = \pm 180^o$), while near the 12 o'clock position, the peak values occur further downstream.
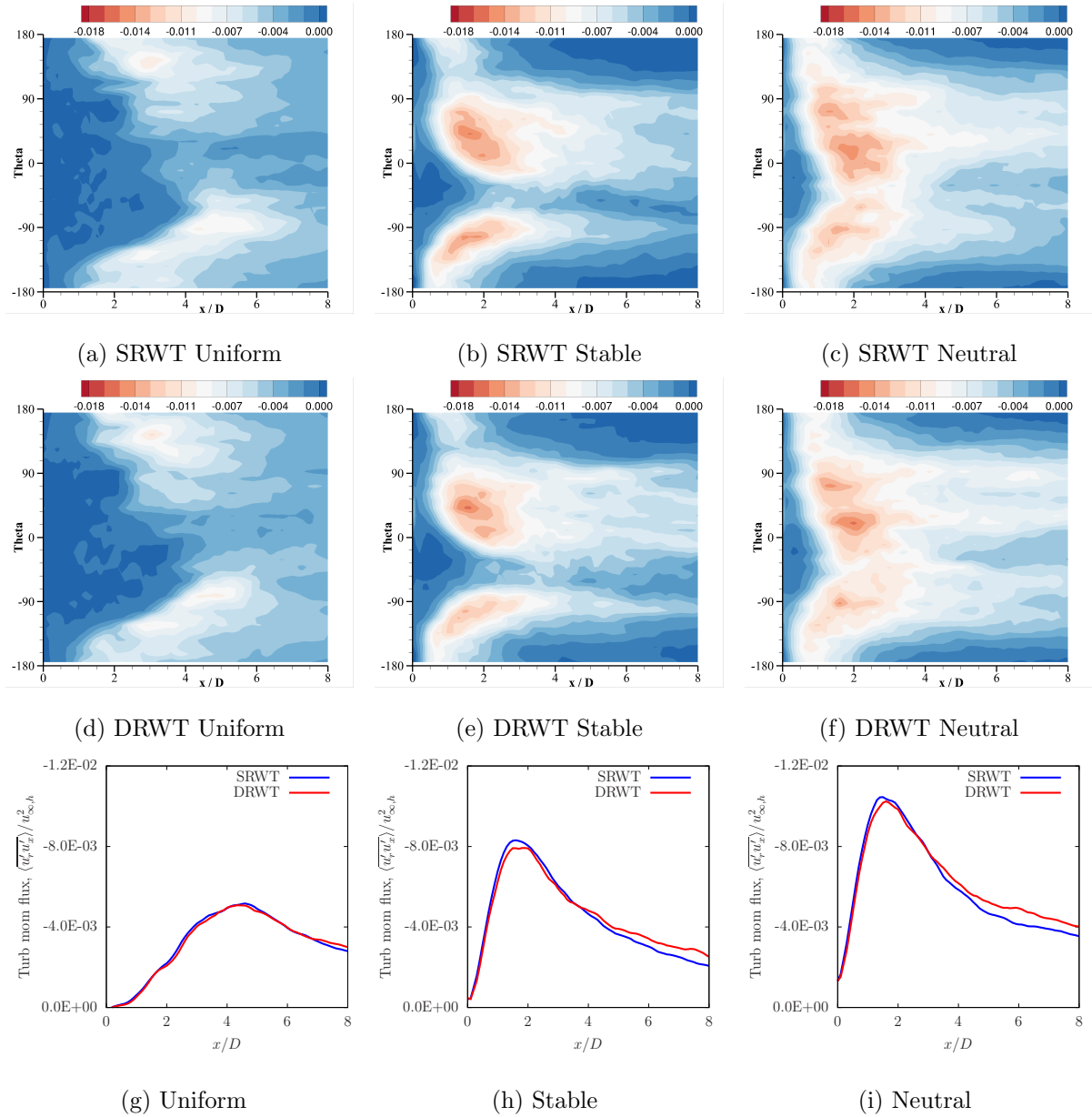
Figure 2.15: Radial transport of streamwise momentum into the turbine wake layer. Color contours show $\overline{u'_r u'_x}/u^2_{\infty,h}$ on the cylindrical surface of Fig. 2.14 that has been cut at $\theta = \pm 180^o$ and unwrapped.

While there is a significant difference in the spatial distribution and magnitudes of $\overline{u'_r u'_x}$ between the three inflow conditions considered, the differences between the SRWT and DRWT are subtle. The DRWT shows a higher level of momentum entrainment, especially for $x > 5D$. To calculate net entrainment from all around the cylinder, $\overline{u'_r u'_x}$ is further averaged azimuthally.

The azimuthal averaging operation is denoted by angle brackets, thus the quantity $\langle \overline{u_r' u_x'} \rangle$ represents temporally and spatially averaged value of $u_r' u_x'$. $\langle \overline{u_r' u_x'} \rangle$ multiplied by the circumference of the cylinder $(2\pi r_{tip})$ is the turbulent momentum entrainment per unit length into the cylinder. Subplots (g-i) in Fig. 2.15 show the variation of $\langle \overline{u_r' u_x'} \rangle$ (normalized by $u_{\infty,h}^2$) with distance from the turbine rotor location. The $y-$axis is reversed in the plots as negative values imply positive entrainment. Variation is plotted on the same scale to contrast the mixing rates between the different inflow conditions. The neutral ABL case shows highest entrainment while the uniform inflow case shows the lowest entrainment. The increase in entrainment for the DRWT over the SRWT is also highest for the neutral ABL case and lowest (indeed there is a slight reduction) for the uniform inflow case. The plots for turbulent flux of kinetic energy $(\overline{u_x} \times \overline{u_r' u_x'})$ are very similar to those for momentum flux and hence are not shown. The overall percentage change in turbulent flux of axial momentum and kinetic energy due to the DRWT are provided in Table 2.2.

A modest 3.29% increase in momentum entrainment is observed. The reader is reminded that in these simulations, the secondary rotor is operated at the tip speed ratio that gives maximum aerodynamic performance for *isolated* turbine operation in uniform inflow conditions. No attempt is made here to optimize the secondary rotor design/operation to enhance wake mixing. Notwithstanding the sub-optimal design/operation, the DRWT still shows higher levels of entrainment than the SRWT for the two ABL cases. These results demonstrate that in a windfarm, the turbines operating in wake flow can benefit from enhanced entrainment provided by the DRWT. Additionally, the fact that the turbine operation and the geometry of the secondary rotor, can be optimized to actively target wake mixing, leaves potential for further improvement in windfarm efficiency from the DRWT technology.

Table 2.2: Percent change (DRWT-SRWT) in cumulative streamwise momentum and kinetic energy for the three inflow conditions.

Inflow condition	$\%\Delta(\overline{u_r'u_x'})$	$\%\Delta(\overline{u}_x \times \overline{u_r'u_x'})$
Uniform	-1.17%	-2.30%
Stable	+1.78%	+1.63%
Neutral	+3.29%	+2.54%

2.4.3 Aerodynamic Loads

Aerodynamic loads in terms of blade root bending moments are analyzed in this section. The approximations made to carry out this analysis are: (1) the rotor blades are assumed to be infinitely rigid (i.e., no deformation in turbine geometry is permitted), (2) the turbine is operated at a fixed rotation rate irrespective of the incoming wind speed (hence the tip speed ratio is fluctuating due to inflow turbulence), and (3) the blade geometry is not resolved in the simulations and hence the potential interaction between the rotors due to blade thickness is not captured.

Figures 2.16 and 2.17 compare the turbine power and out-of-plane blade root bending moment (M_{OOP}) in the time and frequency domains for the two ABL cases simulated. The dynamic loads in the uniform flow case are very small compared to the ABL cases and hence those results are not presented. For the DRWT, turbine power is the sum of powers from the two rotors; blade root moment however is only compared for the main rotor unless otherwise stated. Figure 2.16 compares the DRWT and SRWT power and loads for the stable ABL condition. The secondary rotor in the DRWT efficiently extracts power near the main rotor blade root region and hence the DRWT produces higher net power than the SRWT (see subplot 'a' in Figs. 2.16 and 2.17). In the plots, power is normalized by $1/2\rho\bar{u}_{\infty,h}^3 A_d$ and blade root bending moments by $1/2\rho\bar{u}_{\infty,h}^2 A_d\, r_t$, where $A_d = \pi r_t^2$ and r_t is the main rotor tip radius.
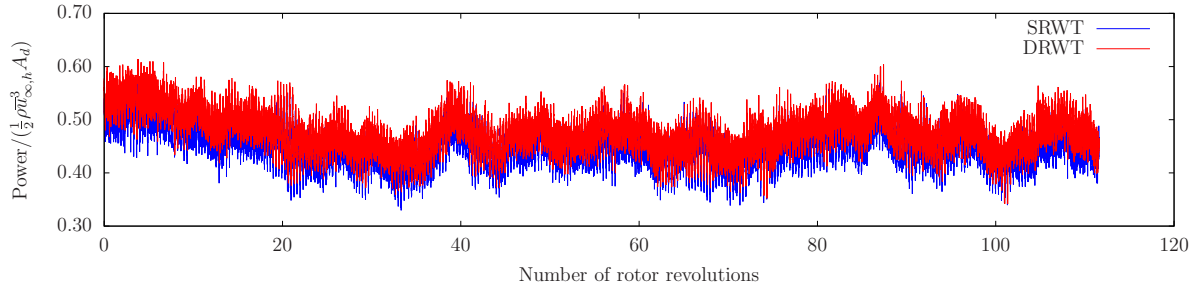
(a) Time variation of normalized turbine power
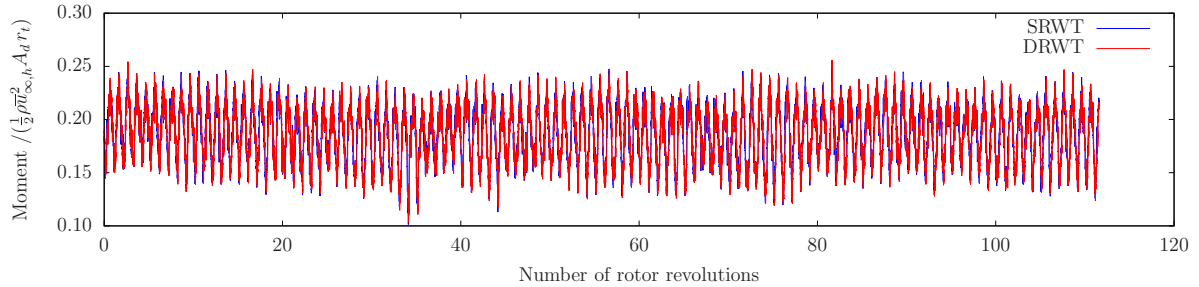
(b) Time variation of normalized M_{OOP}
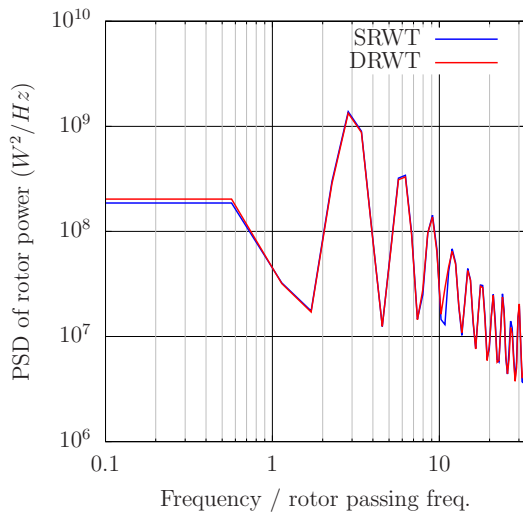
(c) PSD of turbine power
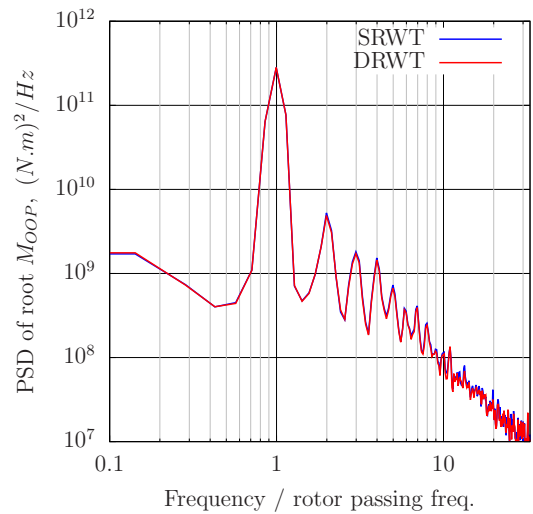
(d) PSD of M_{OOP}

Figure 2.16: **Stable** ABL simulation results. Turbine power and out-of-plane blade root bending moment (M_{OOP}) compared in time and frequency domains.
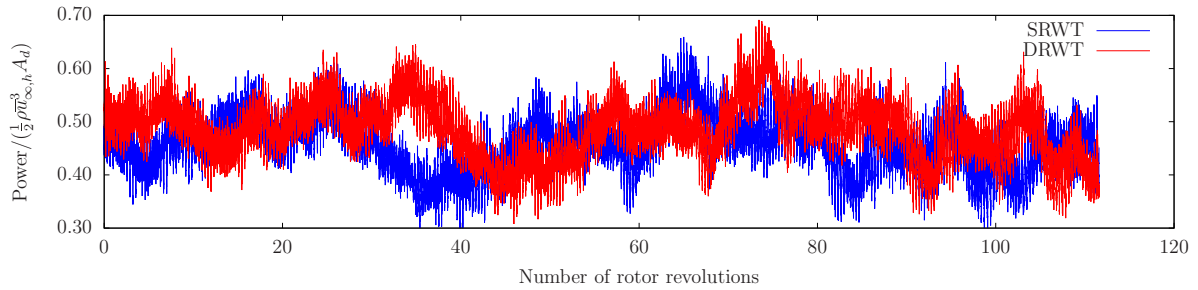
(a) Time variation of normalized turbine power
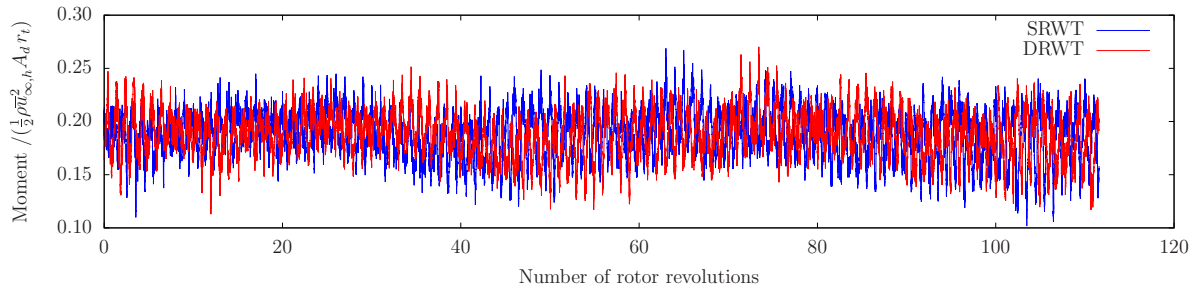
(b) Time variation of normalized M_{OOP}
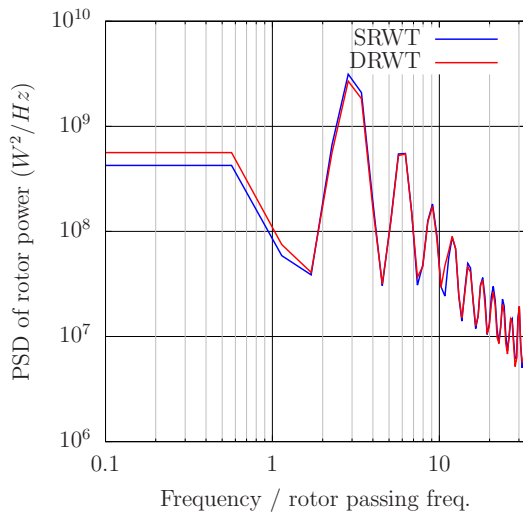
(c) PSD of turbine power
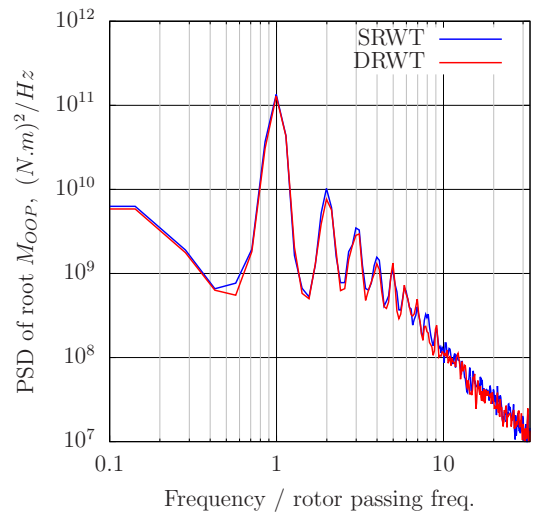
(d) PSD of M_{OOP}

Figure 2.17: **Neutral** ABL simulation results. Turbine power and out-of-plane blade root bending moment (M_{OOP}) compared in time and frequency domains.

Fluctuations in power output are caused by spatial and temporal variations of the incoming wind. While the temporal variations are only due to turbulence, spatial variations also occur in the mean wind speed in the ABL; the mean wind speed varies monotonically with height

from the ground in the area swept by the turbine rotor (see Fig. 2.6a). Each blade of the turbine rotor(s) experiences a one per revolution variation/excitation because of this spatial variation of the mean wind speed - highest wind at the 12 o'clock position and lowest at the 6 o'clock position. This periodic (since the rotor rotation speed is fixed) excitation results in deterministic fluctuations in turbine power and blade loads. The torque contribution from each blade of a turbine rotor adds linearly (scalar addition) to give the net rotor torque (and power); blade root bending moments however are about different axes for each blade, so they need to be added as vectors in order to compute the moment on the turbine shaft. In here we analyze blade root moments. Since the turbine blades are assumed to be identical, one-per-revolution fluctuation in the torque/power for each blade causes a one-per-BPF variation in torque/power for the rotor, where BPF stands for blade passing frequency. Blade root bending moments however are for each rotor blade, which therefore fluctuate at the fundamental frequency of one per turbine revolution, or 1/rev.

Deterministic power fluctuations at the BPF and its harmonics are observed in the power spectral density (PSD) plots (see subplot 'c' in Figs. 2.16 and 2.17) due to the variation of mean wind speed with height as discussed above. In these figures, the main rotor passing frequency is used to normalize frequency. Power fluctuations at secondary rotor passing frequency and its harmonics are also present but they are much smaller in magnitude and are therefore inconspicuous in the figure. While the increase in mean power from the DRWT is measurable (between 5-6%), the change (reduction) in power fluctuations observed is insignificant. Power fluctuations are not desirable, and hence no increase in such fluctuations with the DRWT is beneficial. The difference in out-of-plane blade root bending moment (M_{OOP}) is also insignificant; the DRWT showing a very small reduction at high harmonics of rotor passing frequency (see Fig. 2.17). The reduction is expected to be small since the contribution to root bending moment from the blade root region, where the blade relative flow velocity and the moment arm are both small, is insignificant. The results suggest that the aerodynamic interaction between the main rotor and the secondary rotor has little impact on unsteady aerodynamic loads experienced by the main rotor.

Figure 2.18 compares the M_{OOP} for the SRWT operating in the stable and neutral ABL conditions. The PSD of the M_{OOP} is higher for the stable case at the fundamental rotor passing frequency because the vertical shear in the mean wind speed is higher for the stable case (see Fig. 2.6 (a)). Vertical shear in mean wind results in a 1/rev variation in angle-of-attack, and hence loads, on the rotor blades. At frequencies greater than the fundamental rotor passing frequency, the neutral case shows higher values of M_{OOP} than the stable case. This behavior can be explained by the difference in the size of the turbulent eddies in the two ABL cases. A wind turbine rotor can 'chop' through a large, slow-moving turbulent eddy multiple times, resulting in blade loads at the rotor passing frequency and its harmonics. Integral length scale represents the size of the largest eddies in a turbulent flow. In the present problem, the integral length scale is computed at the hub height using a two-point correlation of streamwise wind velocity, defined as $R_{uu}(r) = \langle \overline{u(\mathbf{x})\,u(\mathbf{x} + r\,\hat{e}_x)} \rangle$, where the angle brackets denote spatial averaging over the horizontal plane at the turbine hub height ($\mathbf{x}.\hat{e}_z = h$), and the overline denotes time averaging. The two-point correlations are computed using the precursor simulations for the two ABL cases and are compared in Fig 2.18 (b). The integral length scale (L) is computed as $L = \int_0^{R_{max}} R_{uu}(r)\,\mathrm{d}r$, where the upper limit of the integral, $R_{max} = 3$ km. The integral lengths are found to be approximately 24 m and 130 m for the stable and neutral ABL cases respectively. The higher values of M_{OOP} at frequencies greater than the fundamental rotor passing frequency can be attributed to the larger eddy sizes (higher integral length scale) in the neutral ABL case.

2.4.3.1   Secondary Rotor

Figure 2.19 presents the power spectral densities of the secondary rotor M_{OOP} for neutral and stable conditions. Contrasting the magnitudes in Fig. 2.19 with those in Figs. 2.16 & 2.17 elucidates that the mean and the fluctuating loads on the secondary rotor are in fact orders of magnitude smaller than those on the main rotor. Therefore, the secondary rotor can be designed with relatively thin airfoils. The abscissa in Fig. 2.19 is normalized by the secondary rotor blade passing frequency. While the decay in power spectral density with frequency is monotonic for the main rotor, that is not the case with the secondary rotor. The M_{OOP} at

the fourth harmonic of rotor passing frequency is higher than the second and third harmonics. This is likely an effect of the aerodynamic interaction between the main and the secondary rotors.

(a) M_{OOP} for the SRWT in ABL

(b) Velocity autocorrelation
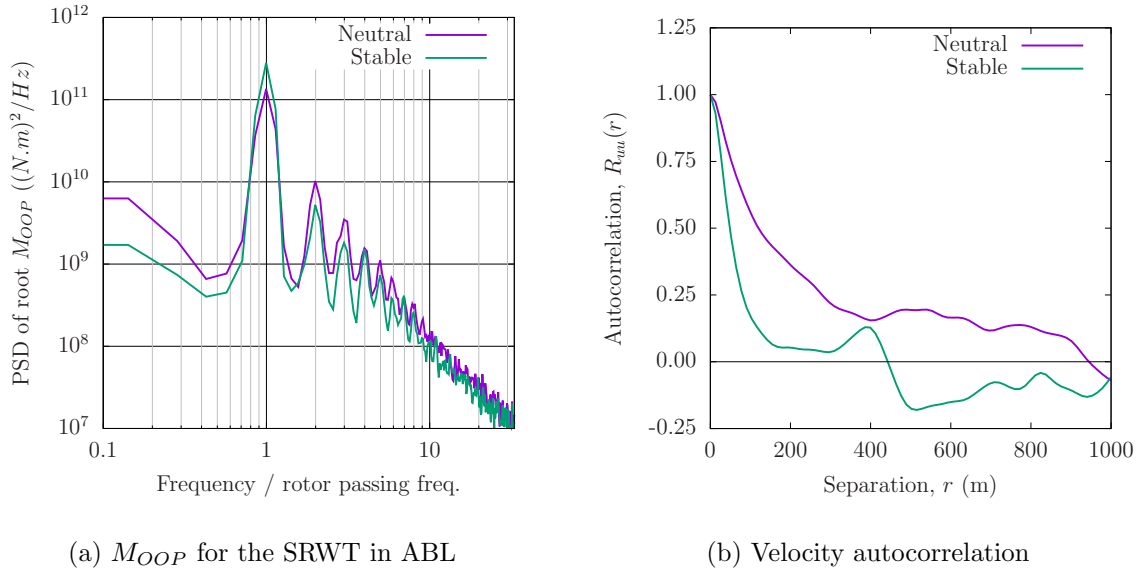
Figure 2.18: Autocorrelation of velocity fluctuation as a function of distance.
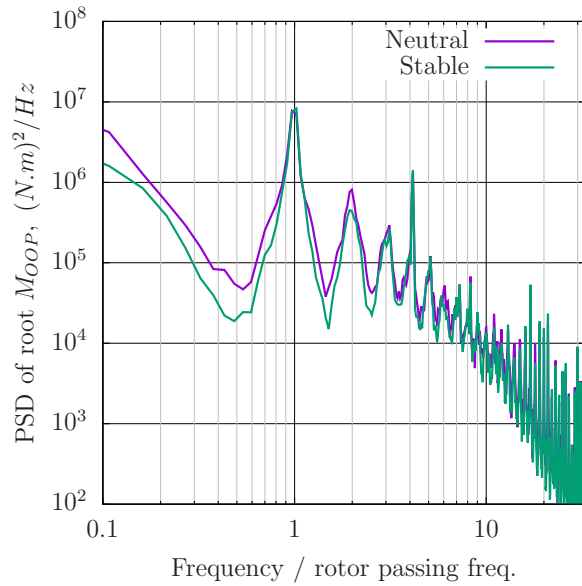
Figure 2.19: Secondary rotor simulation results

2.5   Conclusions

A numerical study is conducted using large eddy simulations to investigate aerodynamic performance and loads for the dual rotor wind turbine (DRWT) technology proposed by Rosenberg *et al.* [1]. The LES solver is first validated against experimental data as well as blade element momentum theory results for a conventional, single-rotor turbine. A two-step procedure is used to first simulate the atmospheric boundary layer and then wind turbine aerodynamics. The DRWT is analyzed for three different inflow conditions - uniform inflow, stable-, and neutral- atmospheric boundary layer. The following conclusions are drawn from the results of this study.

1. The DRWT operating in isolation shows aerodynamic performance (C_P) improvement of about 5-6% for all inflow conditions. The performance benefit is obtained due to efficient extraction of energy (using the smaller secondary rotor) from the streamtube going through the blade root region.

2. The DRWT enhances wake mixing and entrainment of higher momentum fluid from outside the wake layer when the atmospheric (freestream) turbulence is moderately high (as in the neutral stability case simulated here). A modest ($\approx 3.2\%$) increase in momentum entrainment is observed with the *de facto* DRWT design.

3. The enhancement in wake mixing is associated with the increased turbulence intensity in the wake. This could potentially increase fatigue loads on the downstream turbines.

4. Spectral analysis of aerodynamic loads (measured as rotor power and out-of-plane blade root moment) show negligible reduction for the main rotor in the DRWT. Unsteady fluctuations in rotor power are observed at blade passing frequency while fluctuations in blade root moments are at the rotor passing frequency and its harmonics. These fluctuations occur because of the azimuthal variation (due to the ABL) in the incoming mean wind as well as turbulence in the wind.

The enhanced wake mixing rate observed with the DRWT is promising. It proves that the technology has the potential to improve windfarm efficiency if the secondary rotor is optimally designed and/or operated for that purpose.

2.6   Acknowledgement

CHAPTER 3.   INVERSE DESIGN OF SINGLE- AND MULTI-ROTOR HORIZONTAL AXIS WIND TURBINE BLADES USING COMPUTATIONAL FLUID DYNAMICS

Behnam Moghadassian and Anupam Sharma

Abstract

A method for inverse design of horizontal axis wind turbine (HAWT) is presented in this paper. The direct solver for aerodynamic analysis solves the Reynolds Averaged Navier Stokes (RANS) equations, where the effect of the turbine rotor is modeled as momentum sources using the actuator disk model (ADM); this computational fluid dynamics (CFD) approach is referred to as RANS/ADM. The inverse problem is posed as follows: for a given selection of airfoils, the objective is to find the blade geometry (described as blade twist and chord distributions) which realizes the desired turbine aerodynamic performance at the design point; the desired performance is prescribed as angle of attack (α) and axial induction factor (a) distributions along the blade. An iterative approach is used. An initial estimate of blade geometry is used with the direct solver (RANS/ADM) to obtain α and a. The differences between the calculated and desired values of α and a are computed and a new estimate for the blade geometry (chord and twist) is obtained via nonlinear least squares regression using the Trust-Region-Reflective (TRF) method. This procedure is continued until the difference between the calculated and the desired values is within acceptable tolerance. The method is demonstrated for conventional, single-rotor HAWTs and then extended to multi-rotor, specifically dual-rotor wind turbines. The TRF method is also compared with the multi-dimensional Newton iteration method and

found to provide better convergence when constraints are imposed in blade design, even though faster convergence is obtained with the Newton method for unconstrained optimization.

3.1   Introduction

Rapid increase in utilization of turbines to harvest clean and renewable wind energy resource has introduced new challenges for researchers. As power production is directly dependent on the design of the wind turbine blades, considerable research studies have focused on developing methods to improve blade design in order to increase the output power. One approach to blade design is to use direct analysis codes and perform parametric sweeps to identify highest-performing blade design. However, this approach is computationally demanding and does not guarantee that the optimum design will be reached [45]. More recently, researchers have started using optimization algorithms in the blade design process. For example, Chattot [111] used the Lagrange multiplier optimization method to maximize power while constraining thrust at a given tip speed ratio. The inputs to the optimization algorithm were blade twist and chord. A prescribed-wake vortex line method (VLM) was used that consisted of the Goldstein model [112] to analyze the trailing wake vortex structure behind the rotor blades and used the Biot-Savart formula to calculate the induction.

Inverse algorithms were introduced in wind turbine blade design process by Selig and Tangler [47]. They combined the multi-dimensional Newton method with the Blade Element Momentum (BEM) theory to perform inverse blade design. This method is implemented in the software PROPID which can perform inverse design in a variety of ways. One way is to prescribe the desired distributions of axial induction factor (a) and lift coefficient (C_l) along the blade, and the inverse design gives the blade geometry (blade twist and chord distributions) that would yield the prescribed a and C_l distributions. The desired radial distributions of a and C_l are carefully selected based on prior experience of the designer but with the general aim of maximizing annual energy production (AEP). Any combination of aerodynamic quantities, e.g., angle of attack (α), lift coefficient (c_l), circulation (Γ), axial induction (a), etc. can be prescribed as desired distributions that the final blade design is required to satisfy.

Lee [45] proposed the use of VLM over the BEM theory as the direct solver in inverse design of HAWT blades to model the effects of the three dimensional aerodynamic features of modern turbine blades, such as sweep, pre-bend, non-planar wing tips, etc. The VLM allows for partial coupling of the different radial sections of the blade through induced velocity computed via Biot Savart's law. Note that the coupling is partial because the method still uses 2-D airfoil polars and cannot account for spanwise flow over the blade. Radial distributions of a and c_l were used to prescribe the desired blade aerodynamics. The multi-dimensional Newton method was used to iterate on blade geometry (twist and chord) to obtain the prescribed a and c_l distributions.

Selig and Coverstone-Carroll [113] and Giguere and Selig [114] merged the optimization techniques with inverse design approaches to find the blade geometry that would maximize AEP. They utilized the BEM theory along with a genetic algorithm to reach their goal of maximizing AEP through blade design. If blade design is sought with the sole objective of maximizing the AEP without any constraints, the final blade design would have extremely high solidity inboard. The inboard c_l and a distributions are therefore tailored during inverse design procedure to yield a practical blade design that would satisfy design-, manufacturing-, and transportation constraints. Lee *et al.* [115] used this idea to determine the blade shape by considering a target function that includes the AEP as well as the costs for blade masters, mold sets, tooling and blade production. They used the strip theory [116] to perform the inverse design, while their target was to minimize energy loss at the Betz optimum condition. The inverse blade design was a part of a global optimization algorithm which aimed to maximize power production and simultaneously minimize blade cost.

Aerodynamics models that solve the Navier-Stokes equations offer higher fidelity in analysis and design of wind turbine blades in comparison with models based on solving the simplified potential flow equations (e.g., BEM and VLM). The Navier-Stokes equations are usually solved with some simplifying assumptions. For wind turbine aerodynamics application, the incompressible turbulent flow (at least turbulence at high wavenumbers) is modeled (e.g., using eddy-viscosity based turbulence models), rather than directly solved. If the interest is only in mean quantities, time variation is ignored and Reynolds Averaged Navier-Stokes (RANS) equations are used with appropriate turbulence models that present the entire turbulence spectra. Many

researchers [117, 118, 119, 120, 121] have utilized different forms of the RANS model to investigate wind turbines aerodynamics. In one computationally efficient but simplified approach, the blade geometry is not resolved in the simulation, instead, the effect of the spinning blades on the air flow is introduced as source terms (typically as body forces) in the Navier-Stokes equations.

The Actuator Line Method (ALM) [122] and the Actuator Disk Method (ADM) [123] are the most commonly used methods to simulate the effect of rotor blades using body forces without resolving the blade geometry. Both methods use look-up tables for 2-D lift and drag polars (obtained via prior experiments or simulations) with the local flow velocity vector to calculate the net sectional force at each radially discretized element of the blade. The net force is then applied as a spatially distributed (typically a Gaussian distribution is used) source around the radial element. Even though these methods use the strip theory approach with 2-D airfoil polars, they are still advantageous over potential flow methods in that they can, to some degree, simulate turbulent wake mixing. Inverse design approaches that use such CFD techniques then have the potential to explore designs that maximize wake mixing, and hence minimize wake losses in wind farms. This paper presents a methodology to use RANS CFD to perform inverse design of HAWT blades. The approach adopted here for inverse design is to specify the desired α and a distributions and let the inverse design compute the blade twist and chord. The trust-region-reflective method [48, 124] is used as the optimization algorithm. The proposed inverse design procedure is first demonstrated for conventional, single rotor wind turbines (SRWTs) and then extended to multi-rotor wind turbines, e.g., the dual-rotor wind turbine (DRWT) proposed by Rosenberg *et al.* [16].

Manufacturing and transportation constraints on rotor blades of conventional, utility scale wind turbines result in aerodynamically sub-optimal design in the blade root region (inner 25%) [16]. This results in inefficient extraction of energy by the rotor in this region. The dual rotor wind turbine [16, 125, 126] uses a secondary smaller rotor in front of the main rotor to efficiently harness the energy from the airflow passing through the blade root region. Additionally, the DRWT can enhance flow entrainment in the turbine wake, leading to faster wake mixing and reduced wake losses [127, 125, 128]. It should be emphasized that the inverse

design methodology presented in this paper is general enough to readily work for turbines with arbitrary number of rotor disks and is not limited to DRWTs.

3.2 Computational Model

3.2.1 Flow Solver

The incompressible, Reynolds Averaged Navier-Stokes (RANS) equations are solved using the semi-implicit method for pressure linked equations (SIMPLE) algorithm [129]. The governing equations are

$$
\begin{aligned}
\frac{\partial \bar{u}_i}{\partial x_i} &= 0, \text{ and,} \\
\bar{u}_j \frac{\partial \bar{u}_i}{\partial x_j} &= -\frac{1}{\rho}\frac{\partial \bar{p}}{\partial x_i} - \nu \frac{\partial^2 \bar{u}_i}{\partial x_j^2} - \frac{\partial \overline{u_i' u_j'}}{\partial x_j} + \frac{f_i}{\rho}.
\end{aligned} \tag{3.1}
$$

The two-equation $k - \epsilon$ turbulence model by Launder and Spalding[130], with modifications suggested in Hargreaves and Wright[131], is used for turbulence closure. The source term f_i in the momentum equation, Eq. (4.1) is used to model the force exerted by the turbine rotor blades on the fluid. This force is determined using the blade element theory, which requires local flow velocity at turbine location, geometric information about rotor blades such as chord and twist, and blade aerodynamic characteristics. Blade aerodynamic characteristics are specified as sectional lift and drag coefficients and are provided by the user as look-up tables. The airfoil polars may be corrected for rotational and dynamic stall effects. The body force, f_i is calculated using the Actuator Disk Method (ADM) by distributing the force over a disk surrounding the turbine rotor using a Gaussian distribution [32]. The numerical analysis procedure has been implemented in the unstructured, finite volume solver simpleFOAM (part of OpenFOAM) and has been previously validated against experimental data [16, 121, 132].

3.2.2 Simulation Set-up

The objective of the paper is to demonstrate an inverse blade design procedure that uses CFD to perform aerodynamic analysis. To minimize design time, a cost-effective computational setup is selected that is consistent with traditional inverse design methods. Specifically, a

uniform, smooth inflow is considered, all rotor blades are assumed to be identical, and only mean (time-steady) performance is investigated. With these approximations, the problem becomes axisymmetric and makes the large number of calculations, as required by inverse design procedures, conducive.

Figure 3.1 shows an isometric view of an example axisymmetric mesh used in the study with the x axis as the symmetry axis. The radius of the disk is along the z-direction. The lengths are nondimensionalized by the tip radius of the turbine rotor, R. The domain is $20\,R$ in x direction and $6\,R$ in z direction. It is one cell thick in the y direction and the angle between the side planes is selected to be $1°$. The turbine rotor (or the two rotors for a DRWT) is located around $x = 0$ and the mesh is refined in the region of the rotor disk to capture the large gradients expected there; the mesh is also refined at the radial location corresponding to the blade tip location ($z = 1$).
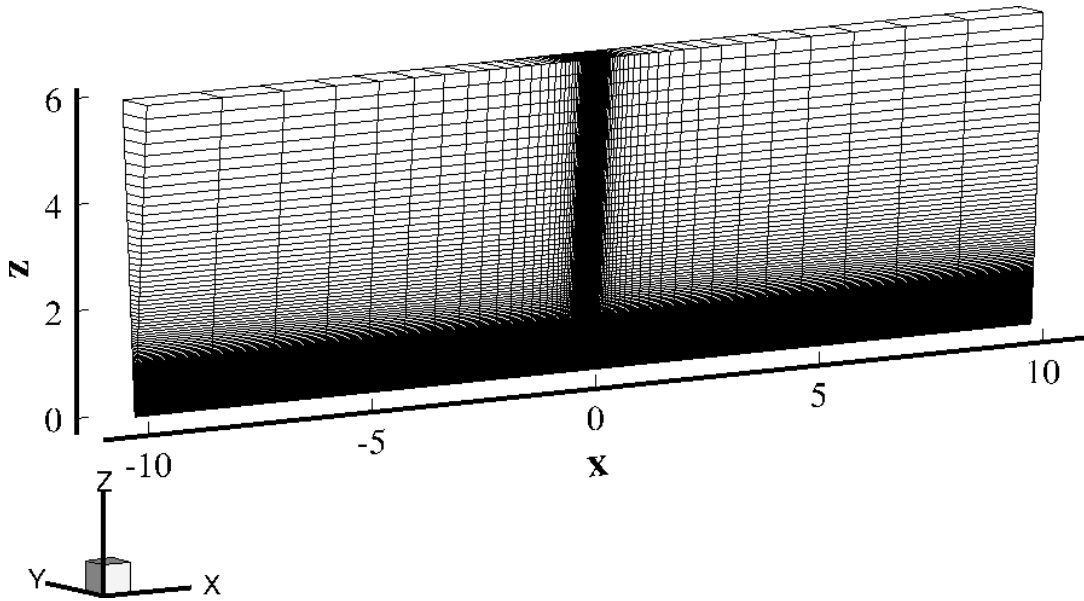
Figure 3.1: Isometric view of the computational mesh used for the proposed inverse design.

The inflow is in the positive x direction and the force exerted by the turbine on the fluid is applied in the negative x-direction. For a rotor spinning in the clockwise direction, as viewed from upstream, the torque force on the fluid is applied in the positive y direction. Axisymmetry boundary condition is applied on the side planes. Zero gradient is imposed for pressure and velocity at the outlet boundary. At the inlet, a zero-gradient pressure and a fixed-value velocity

boundary conditions are prescribed. The same setup was used in previous studies [16, 121, 132] where the methodology was verified against experimental data for aerodynamic performance prediction.

3.2.2.1 Mesh Sensitivity Study

Sensitivity of the RANS/ADM solver to mesh size is investigated with four different meshes. Table 3.1 lists the mesh dimensions and the corresponding computed turbine power coefficient, C_P. Variation with mesh size of radial distributions of angle of attack (α) and axial induction factor (a) are plotted in Fig. 3.2. As seen in the figure, refining the grid beyond $N_x \times N_z = 101 \times 229$ (mesh 2) does not adversely impact the results; the C_P value becomes constant and the variations in radial distributions are minimal. Hence, the grid resolution of mesh 2 is selected to obtain the results presented in this paper. This study is conducted for a conventional single-rotor wind turbine and grids for mulit-rotor wind turbined are deduced from this assessment. A detailed mesh sensistivity study for this solver has been reported previously in Ref. [133].

Table 3.1: Mesh sensitivity study: grid dimensions and aerodynamic power coefficient.

Mesh #	$N_x \times N_z$	C_P
1	79×141	0.483
2	101×229	0.485
3	117×279	0.485
4	136×329	0.485

3.2.3 Solution Algorithm

The purpose of using an inverse scheme in a wind turbine blade design process is to directly compute blade geometries which give the desired aerodynamic performance. The designer can choose the target aerodynamic performance parameters and prescribe their desired values (distributions). If the prescribed values of the aerodynamic performance parameters are physically consistent and achievable, the inverse design process should give the turbine blade geometry that meets the desired performance.
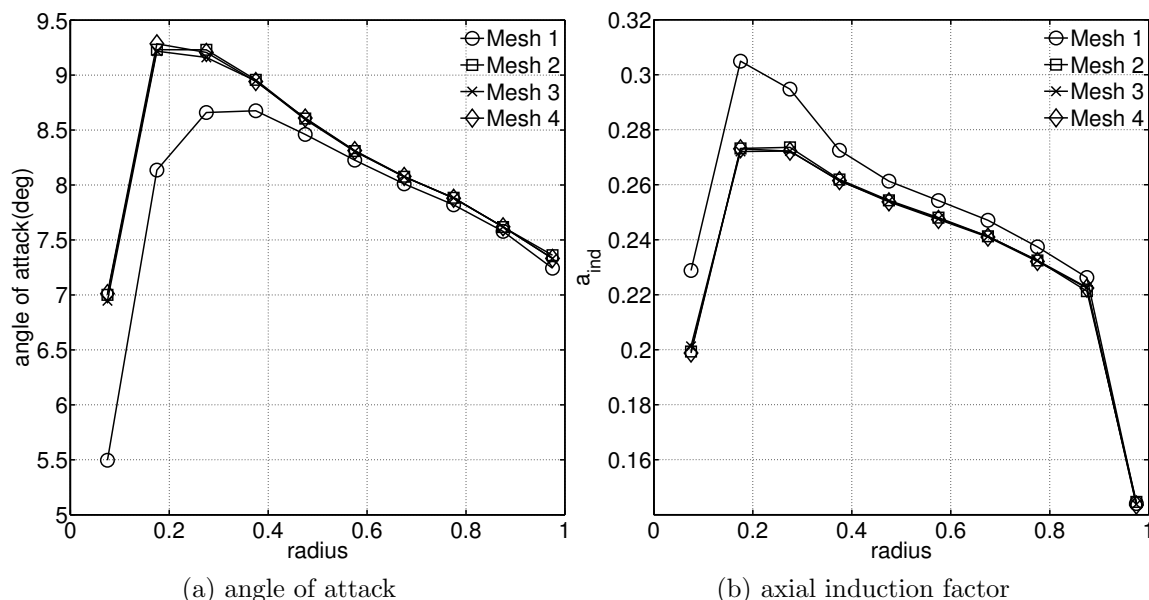
Figure 3.2: Results of mesh sensitivity study. RANS/ADM predicted distributions of angle of attack and axial induction factor are compared between four different mesh sizes.

While there are multiple ways in which the inverse design problem can be posed, we choose to prescribe distributions of axial induction factor (a), and angle of attack (α) as desired outcomes. As an example, in an ideal single-rotor turbine, the desired a could be 1/3 based on the 1-D momentum theory, and the target α values could be selected to give the highest lift-to-drag ratio for the airfoil at that radial location. In other studies, C_l distributions, as opposed to α distributions have been prescribed [45]. There is one potential problem with that choice – the $\alpha - C_l$ curve is multi-valued, i.e., a given value of C_l can occur for multiple α values (pre- and post-stall). While at a typical design point, all radial locations are in the pre-stall region, an iterative design procedure can have transients in the post-stall region and hence the duality of $\alpha - C_l$ curve can pose problems. Prescription of α is still based on the desired C_l/C_d (presumably where it is maximum), but it ensures that the turbine is not designed to operate in the post-stall regime of that airfoil. Therefore, in this study the desired parameters are set to be α and a. The inverse design algorithm then proceeds as follows:

1. The blade is discretized along the span into m segments and the desired values of α and a are prescribed for each segment j as a 1-D vector $\mathbf{b} = \{\alpha_j, a_j\}^T$.

2. For the first iteration ($n = 0$), an initial guess of the blade geometry is provided as a 1-D vector, $\mathbf{x}_0 = \{c_j, \theta_j\}^T$ of length $2\,m$, where c_j and θ_j are the blade chord and twist angle at segment j.

3. The inverse subroutine is invoked (details provided in Sec. 3.2.4):

    (a) With $\mathbf{x}_n$ as the baseline design, the direct solver is called $2\,m + 1$ times, to measure the effect of perturbing (by an infinitesimal amount) each element of $\mathbf{x}_n$ on $\mathbf{b}_n$ (distributions of α and a at iteration n). The Jacobian (sensitivity) matrix ($= \partial\{\alpha, a\}/\partial\{\theta, c\}$, see Fig. 3.4) is calculated using first order, forward finite differences.

    (b) A new estimate of the blade geometry $\mathbf{x}_{n+1}$ is computed using the Jacobian matrix and the Trust-region-reflective method (described in Sec. 3.2.4) with the aim of minimizing the difference between the desired and the computed distributions of α and a.

    (c) The direct solver (RANS/ADM) is used to evaluate the aerodynamic performance of the new turbine geometry ($\mathbf{x}_{n+1}$) and obtain $\mathbf{b}_{n+1} = \{\alpha_j, a_j\}^T$.

    (d) If the $\boldsymbol{l}^2$ norm of the difference between the desired and computed aerodynamic performance $\mathbf{b}$ ($= \{\alpha_j, a_j\}^T$) is within the desired tolerance (this is just one of many stopping criteria), the algorithm is terminated and the current blade geometry $\mathbf{x}_{n+1}$ is output as the final blade design. Otherwise, the algorithm returns to step 3(a) and the iterations continue with the iteration counter n incremented to $n + 1$.

The algorithm is presented as a flowchart in Fig. 3.3.
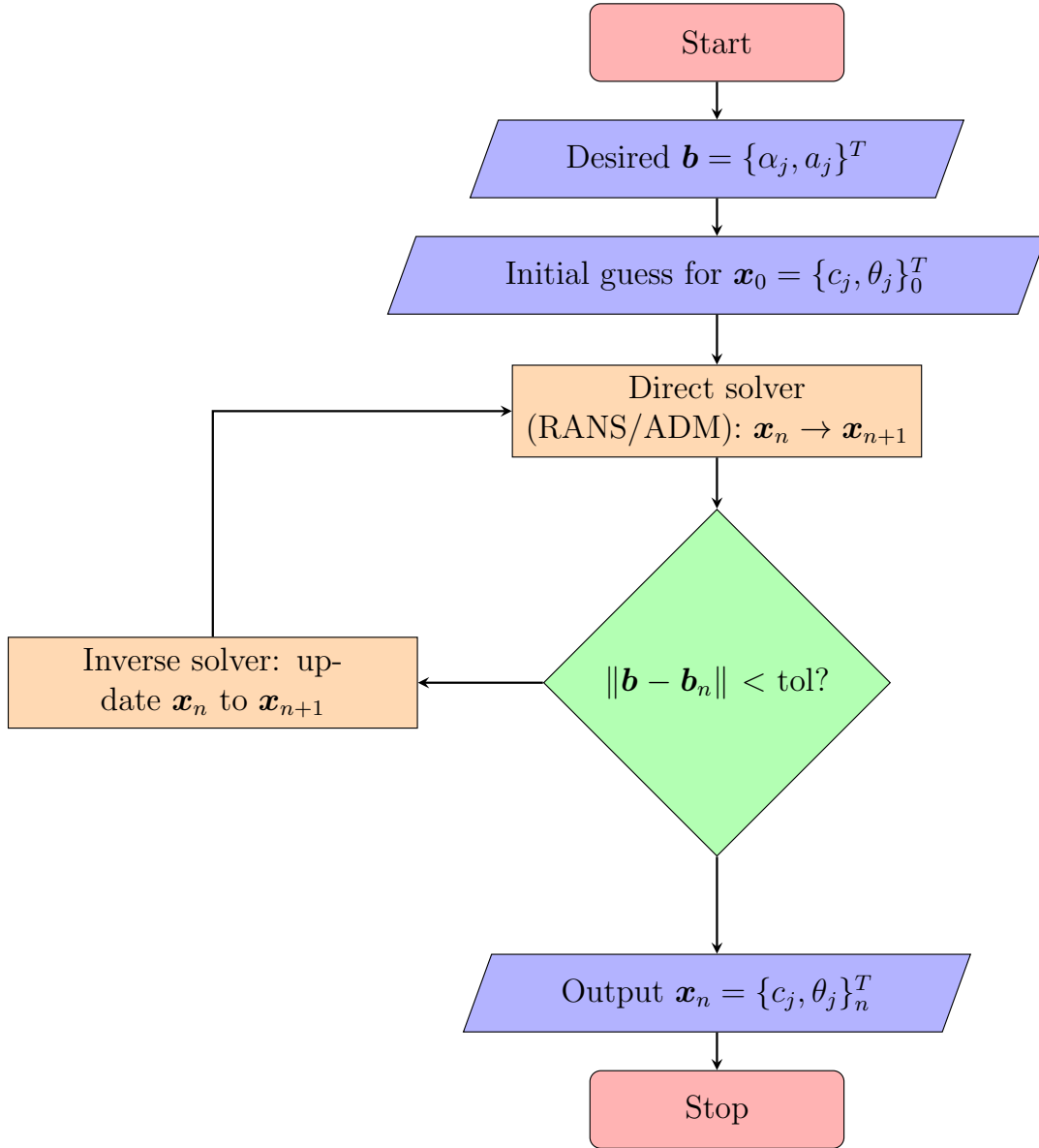
Figure 3.3: Flowchart of the inverse design algorithm.

3.2.4 Inverse Solver

This section provides a brief introduction to the selected inverse solver, the trust-region-reflective (TRF) method. Suppose the minimum of a function f is sought in a bounded or unbounded domain. As a first guess, a point x_0 in the domain is randomly picked and the function f is evaluated at x_0. The essential idea behind this method is to approximate f with a simpler function q (see Eq. 4.2) that behaves similarly to f in the vicinity (trust region, N) of x_0 and find a new point x_1 in N where q is minimum. Now if the reduction in the approximated

function (q) is also inherited by the original function f, x_1 is accepted as an updated estimate of the location of minimum value of f, and the procedure is repeated. Otherwise the trust region (N) is reduced in size and the search for minimum q is repeated. In order to reduce the computational time, the trust-region sub-problems are confined to two dimensional sub-spaces S. In fact, the sub-problem is defined as

$$\arg\min\{q(s)\}, \text{ subject to } ||Ds|| \leq \Delta \text{ and } s \in \text{span}[s_k^U, s_k^{FS}], \tag{3.2}$$

where $q(s) = f(x_k) + s^T g + \frac{1}{2} s^T H s$ is the approximation for f around x_k, g is the gradient of f at x_k, and H is the Hessian matrix (symmetric matrix of second derivatives of f), D is the diagonal scaling matrix, Δ is the radius of the trust region, s_k^U is the steepest descent direction given by $s_k^U = -g\,(g^T g)/(g^T H g)$, and s_k^{FS} is either an approximate Newton direction, $H \cdot s_k^{FS} = -g$, or a direction of negative curvature, $(s^{FS})_k^T \cdot H \cdot s_k^{FS} < 0$. This formulation results in global convergence through the steepest descent or negative curvature direction while achieving a fast local convergence, when it exists, using the Newton step[134, 48] in each trust region.

In this study, the multi-dimensional function $\mathbf{F}$ is defined as

$$\mathbf{F}(\mathbf{x}) = \mathbf{b}^d - \mathbf{b}_n^c = \begin{bmatrix} F_1(\mathbf{x}) \\ F_2(\mathbf{x}) \\ \vdots \\ F_m(\mathbf{x}) \\ F_{m+1}(\mathbf{x}) \\ \vdots \\ F_{2m}(\mathbf{x}) \end{bmatrix} = \begin{bmatrix} \alpha_1^d - \alpha_1^c \\ \alpha_2^d - \alpha_2^c \\ \vdots \\ \alpha_m^d - \alpha_m^c \\ a_1^d - a_1^c \\ \vdots \\ a_m^d - a_m^c \end{bmatrix}, \tag{3.3}$$

where superscripts d and c stand for the desired and calculated values respectively, and $\mathbf{b}$ is the vector of design parameters. There are multiple stopping criteria for this algorithm: maximum number of inverse iterations, minimum values of the target function, magnitude of change in the independent variables, and norm of gradient of the target function. The algorithm stops when any of these criteria is met. Based on the preliminary tests, the maximum number of inverse iterations is set to 30 and the minimum values of $\|\mathbf{F}\|$, $\|\Delta\mathbf{x}\|$ and $\|\Delta\mathbf{g}\|$ are set to 10^{-8}. The discussions on the merits of the TRF method over the other optimization schemes as well

as details of how the algorithm proceeds under different circumstances and determining the size of the domain N for the trust-region-reflective algorithm can be found in Refs. [134, 48]. The interested reader is referred to Refs. [124, 48, 134] for a detailed description of the method.

3.3   Verification of Inverse Design Methodology

The proposed inverse design procedure is tested for three conventional, single rotor wind turbines (SRWTs) and two dual rotor wind turbines (DRWTs). A description of these test cases and the performance of the inverse design procedure are presented in this section. The purpose of these tests is to ensure that the algorithm is capable of obtaining blade designs which satisfy different design target values for blades made of different airfoils. It should be noted that the direct solver (RANS/ADM model) utilized in this study has been validated previously [16, 121] for wind turbine aerodynamic performance prediction. For optimization, the nonlinear least-square solver package *scipy.optimize*, available with the *Python* scripting language is employed.

3.3.1   Test Case 1: Single-Rotor Betz Optimum Turbine

As a first test case, we attempt to design the Betz optimum rotor. Per the 1-D momentum theory, the axial induction factor should be 1/3 over the entire rotor disk to achieve maximum C_P. The turbine blade is desired to be designed using one airfoil (the 18% thick DU-96-W180 airfoil) for the entire blade span. This airfoil has a high lift-to-drag ratio and typically is deployed for tip sections of long blades[16]. To achieve the best performance, the desired α is selected to be 10 degrees, which is where C_l/C_d is maximum for the DU-96-W180 airfoil. Therefore, $\alpha_j = 10°$, $a_j = 1/3$ is specified for all radial segments $\forall j \in [1, m]$. The design tip speed ratio, $\lambda = \Omega R/u_\infty$ is set to be 7.0.

The design algorithm needs to compute the Jacobian matrix $(= \partial\{\alpha_j, a_j\}/\partial\{\theta_k, c_k\})$ in order to find the new minimum point at each iteration [134]. Information about the Jacobian matrix is also useful to understand how output variables, $\{\alpha_j, a_j\}$ at the jth radial segment of the blade, are influenced by change in input variables $\{c_k, \theta_k\}$ at the kth radial location on the blade; $\forall j, k \in [1, m]$.

The elements of the Jacobian matrix are calculated using a forward finite difference formula. Figure 3.4 plots the Jacobian matrix, split in four blocks. The blade is discretized into $m = 10$ segments, hence each block has 10×10 elements. Each block of the Jacobian matrix in Fig. 3.4 is expected to be diagonally dominant, as a change in geometry at a given radial location has maximum effect on the aerodynamic performance at the same radial location. The effect can be felt at other radial stations as well (off-diagonal terms), but it is much smaller than the diagonal terms. The results in Fig. 3.4 validate this hypothesis. It should be noted that due to the non-linearity of the function $\mathbf{F}(\mathbf{x})$ in Eq. (3.3), the Jacobian matrix needs to be updated at each optimization iteration. Figure. 3.4 plots the Jacobian matrix at the last iteration when convergence is achieved.

(a) Schematic of the Jacobian matrix (b) The Jacobian matrix
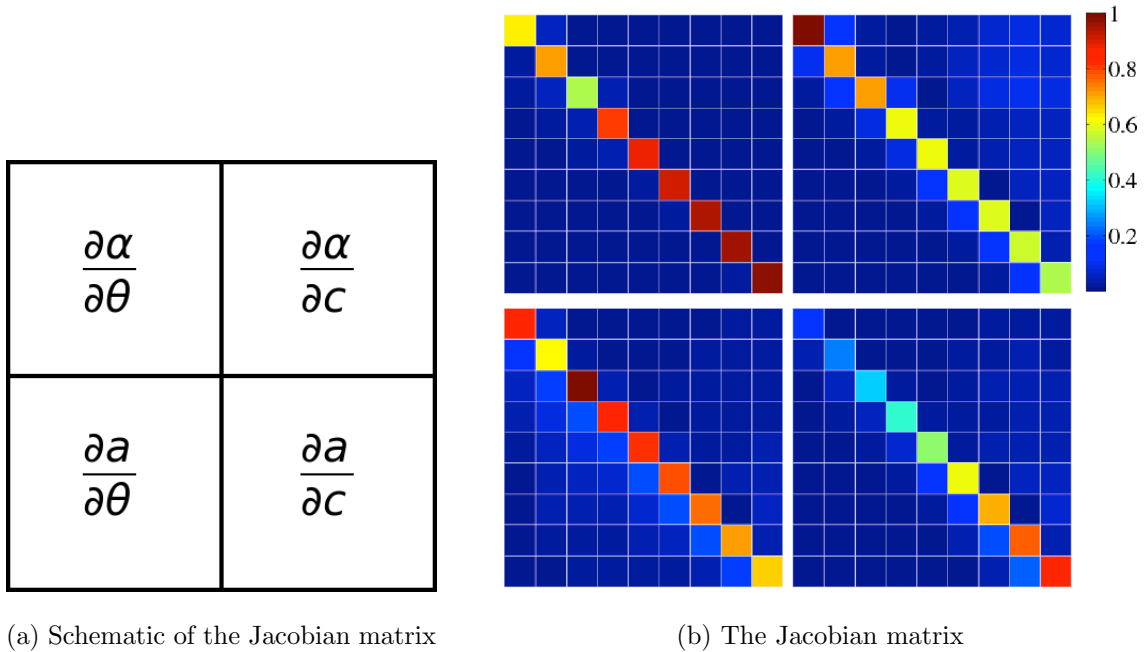
Figure 3.4: Visualization of the Jacobian matrix: (a) a schematic showing the arrangement of the four different blocks in the Jacobian matrix, (b) contour plots for each of the four blocks of the matrix.

Figure 3.5 shows the input and output of the optimization algorithm. Radius and chord are non-dimensionalized by the tip radius (R). The initial estimates for both chord and twist are uniform everywhere and are far from the final distribution. The method converges to the

desired values of α and a. The c and θ distributions of the converged result (see Fig. 3.5 (c,d)) are typical of wind turbine blades and the calculated values of a and α are almost identical to the desired (prescribed) values (Fig. 3.5 (a,b)).
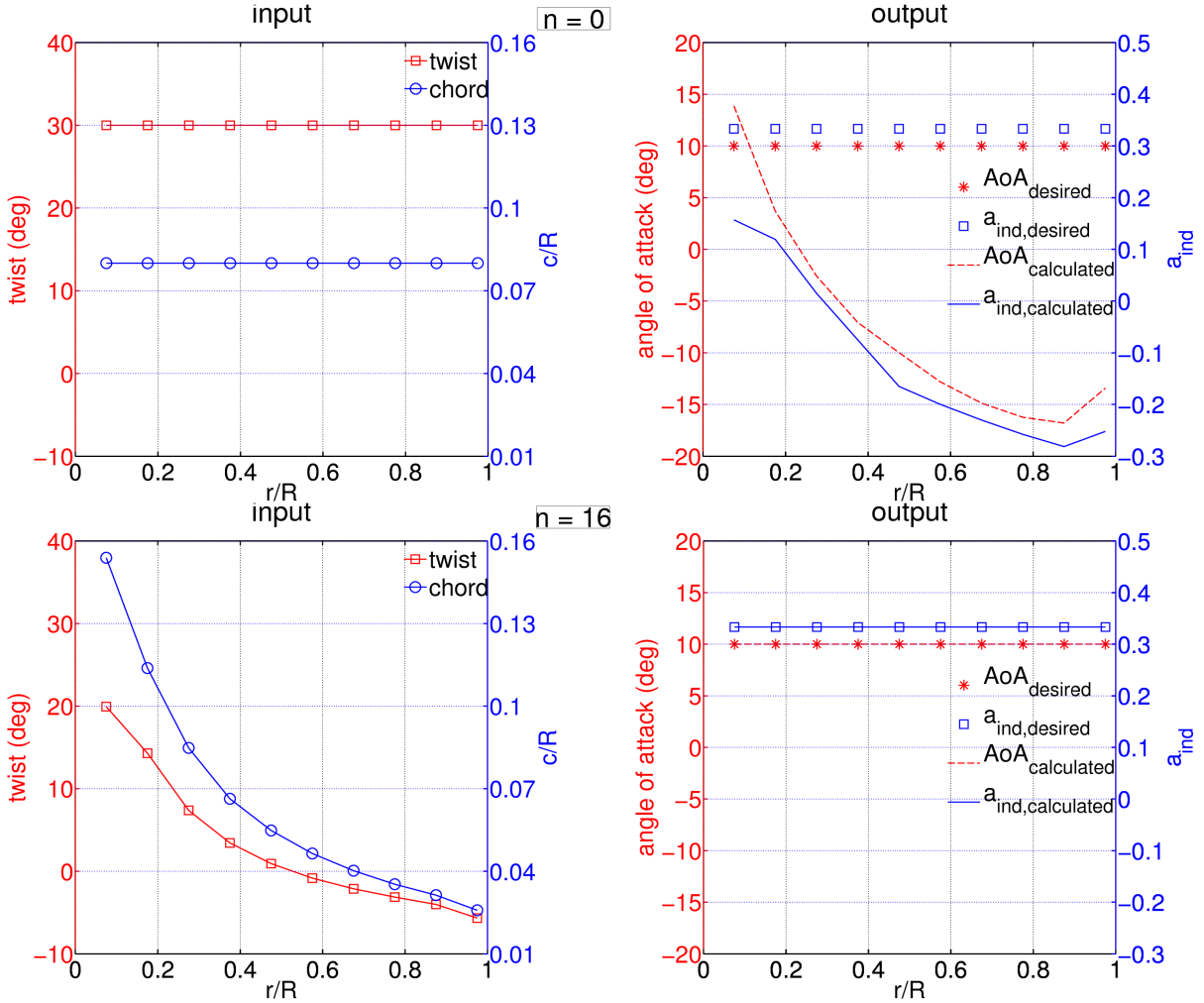
Figure 3.5: Results for test case 1, input (chord and twist distribution) and output (angle of attack and induction factor) for the first and last iterations.

The algorithm was tested with various initial input distributions of c and θ and was found to always converge, demonstrating that the method is robust and insensitive to initial estimates. This test case validates the capability of the algorithm to perform inverse design of single rotor wind turbines.

3.3.2   Test Case 2: SRWT with $\{\alpha, a\}$ Prescribed using RANS/ADM

The objective of this test case is to verify the inverse algorithm for a turbine blade that is made of different airfoils along its span. The NREL 5 MW wind turbine [36] is considered for this test. This turbine rotor blade has cylindrical cross-section at its root and the rest of the blade is made of seven different airfoils. For this test case, the turbine geometry as given in Ref. [36] is used with the RANS/ADM solver to obtain α and a distributions. These distributions are then prescribed as the desired values for the inverse design algorithm. Constant c and θ along the blade are used as the initial guess of the blade geometry. The test of the inverse algorithm is in obtaining the original c and θ distributions of Ref. [36]. The inverse algorithm can successfully reproduce the c and θ distributions with less than 1% error in l^2 norm after only 21 iterations. Figure 3.6 shows the original c and θ distributions as well as the converged results, which are nearly overlaid. The initial guess of uniform c and θ distributions are omitted from Fig. 3.6 for clarity.
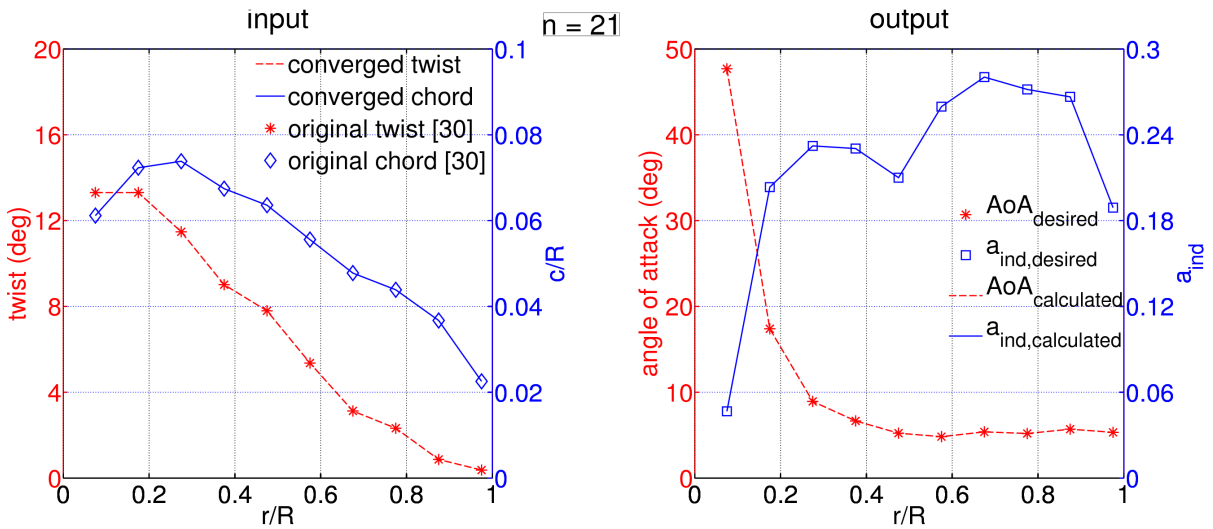
Figure 3.6: Results for test case 2. Converged input (chord and twist distribution) and outpput (angle of attack and induction factor) at the last iteration.

3.3.3   Test Case 3: SRWT with $\{\alpha, a\}$ Prescribed using BEM

Inverse design process is applied to a conventional SRWT made entirely from a single airfoil (DU-96-W180). The test is similar to test case 2 with the exception that BEM is used as

the direct solver instead of RANS/ADM to obtain the desired distributions of α and a. Note that the inverse design algorithm remains unchanged and it still uses RANS/ADM as its direct solver.

Due to the differences between RANS/ADM and BEM algorithms, the blade design obtained using the inverse method cannot be expected to yield exactly the original geometry (c and θ distributions) as was the case in test case 2. The purpose of this test is to ensure the capability of the presented inverse design algorithm to yield a geometric design that is consistent with the direct solver used; in this case RANS/ADM when the desired output is prescribed by another direct solver.

Figure 3.7 shows the final results for this test. While the uniform initial distributions for c and θ are far from the final design, the inverse design algorithm can successfully yield a blade geometry (c and θ distributions) that results in the desired distributions of α and a over the blade span.

Figure 3.7: Results for test case 3. Converged input (chord and twist distribution) and outpput (angle of attack and induction factor) at the last iteration.

3.3.4 Trust-Region-Reflective Method versus Multi-dimensional Newton Iteration

The trust-region-reflective (TRF) method is compared against the multi-dimensional Newton iteration method for test cases 1 and 3. The multi-dimensional Newton iteration method

is a standard optimization method that has been used in other wind turbine inverse design approaches (see e.g., Refs. [47, 45]). The variation with iteration number of the l^2 norm of the objective function $\boldsymbol{F}$, which is representative of residual error, is compared between the two methods. It should be noted that in order to ensure a physically realistic blade shape, the blade chord is constrained to have a value between $0.01\,R$ to $0.2\,R$.

As demonstrated in Fig. 3.8, the decrease in the norm of $\boldsymbol{F}$ for test case 1 is much faster with the TRF method than with the multi-dimensional Newton iteration method. In this case, the Newton method is trying to push the blade chord at some radial stations beyond the specified constraint of $0.2\,R$. To impose the constraint, the chord is limited to $0.2\,R$ at each iteration. This results in oscillations in the l^2 norm of $\boldsymbol{F}$.

When the chord values do not hit a constraint during convergence, as is the case in test case 3, the Newton method converges faster than the TRF method. In general, the Newton method converges faster for *unconstrained* problems while the TRF method is found to be more stable in *constrained* blade design problems. The reason for this additional stability of the TRF method can be attributed to the gradual expansion of the trusted region in which the solution to the sub-problem is sought (see Section 3.2.4). Nonetheless, both methods converge, and ultimately yield identical c and θ distributions.

3.4   Extension to Multi-Rotor Wind Turbines

This section presents the extension of the inverse blade design process to dual-rotor wind turbines (DRWTs). The procedure can be easily extended to multi-rotor turbines with more than two rotors by applying the same idea presented here.

For inverse design of DRWTs, modifications in computational set-up as well as arrangement of the Jacobian matrix are made. As mentioned in Section 4.1, DRWTs use a smaller, secondary rotor upstream of the main rotor in order to reduce blade root loss and enhance momentum entrainment. Two cases of DRWTs with different blades and rotor radius ratio, R_u/R_d are presented in this section where subscripts u and d stand for upstream and downstream rotors, respectively. Upstream rotor sits at $x_u = -Sep/2$ and downstream rotor is located at $x_d = +Sep/2$ where Sep is the rotor-rotor separation distance between the two rotors. Both rotors
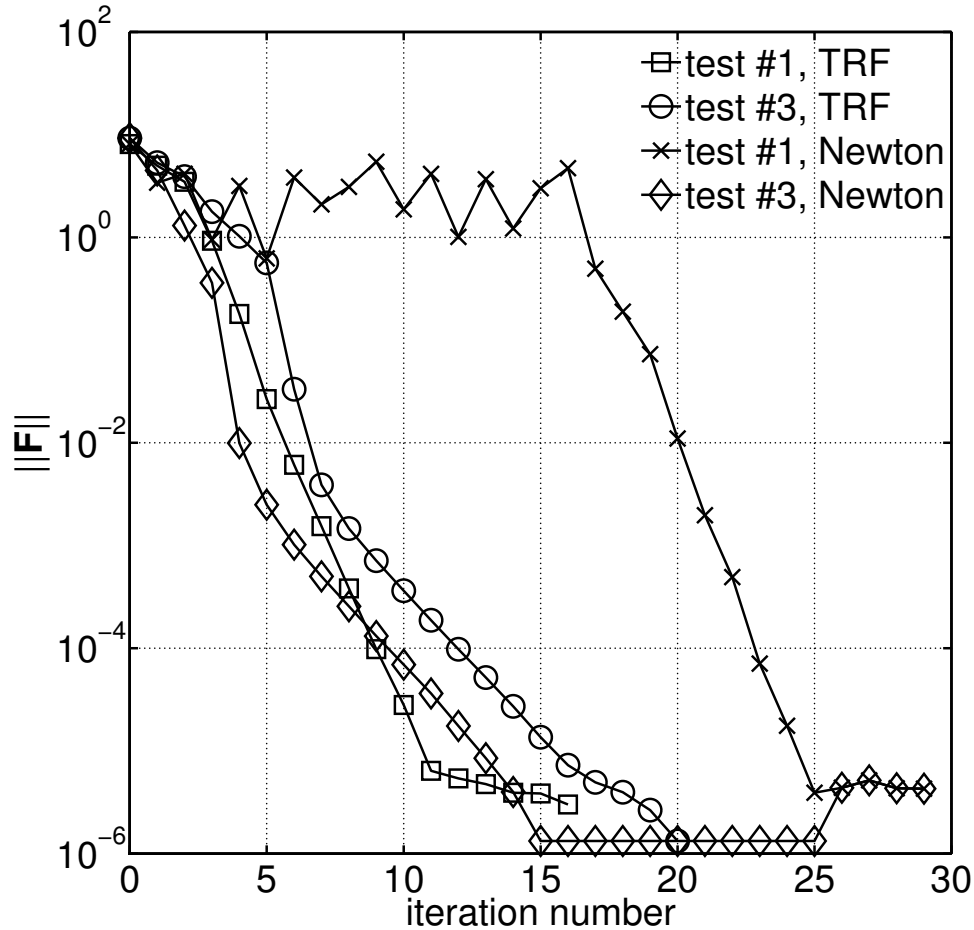
Figure 3.8: Comparison between multi-dimensional Newton iteration and trust-region-reflective optimization methods.

are modeled as actuator disks and the mesh is refined in the vicinity of the two rotor disk locations in both x and z directions. Independent variables are θ and c distributions, and target parameters are radial profiles of α and a for both rotors. For DRWTs, the Jacobian (sensitivity) matrix not only includes the effects of changing design variables of each rotor on its own target variables, but also interaction effects between the rotors. A schematic of the Jacobian matrix is shown in Fig. 3.9. For DRWT cases, it has 4 quadrants and each quadrant has 4 blocks. The diagonal quadrants model self-influence of each rotor, while the off-diagonal quadrants model rotor-rotor interaction effects.

Aerodynamic interactions (coupling) between the two rotors of a DRWT makes the design process more complicated. The main interaction between the two rotors is due to the fact that a part of the downstream rotor operates in the wake of the upstream rotor. A change in

$$
\begin{array}{|cc|cc|}
\hline
\dfrac{\partial(\alpha)_u}{\partial(\theta)_u} & \dfrac{\partial(\alpha)_u}{\partial(c)_u} & \dfrac{\partial(\alpha)_u}{\partial(\theta)_d} & \dfrac{\partial(\alpha)_u}{\partial(c)_d} \\
\dfrac{\partial(a)_u}{\partial(\theta)_u} & \dfrac{\partial(a)_u}{\partial(c)_u} & \dfrac{\partial(a)_u}{\partial(\theta)_d} & \dfrac{\partial(a)_u}{\partial(c)_d} \\
\hline
\dfrac{\partial(\alpha)_d}{\partial(\theta)_u} & \dfrac{\partial(\alpha)_d}{\partial(c)_u} & \dfrac{\partial(\alpha)_d}{\partial(\theta)_d} & \dfrac{\partial(\alpha)_d}{\partial(c)_d} \\
\dfrac{\partial(a)_d}{\partial(\theta)_u} & \dfrac{\partial(a)_d}{\partial(c)_u} & \dfrac{\partial(a)_d}{\partial(\theta)_d} & \dfrac{\partial(a)_d}{\partial(c)_d} \\
\hline
\end{array}
$$

Figure 3.9: Schematic of the Jacobian for DRWT cases.

the geometry of the upstream rotor affects its wake, and for practical rotor-rotor separation distances (small compared to rotor radius), the aerodynamic response of the downstream rotor. The downstream rotor also has a potential field which affects the aerodynamics of the upstream rotor, although this effect is expected to be much smaller compared to that due to the wake. The Jacobian matrix is helpful in visualizing, understanding, and quantifying such interaction effects.

To verify the extension of the inverse design algorithm to DRWTs, several cases corresponding to the SRWT test cases 2 and 3 were attempted. The inverse algorithm was able to successfully obtain the original distributions of c and θ in all cases. Only two of these cases are reported here for brevity.

3.4.1 Test Case 4: Inverse Design of DRWTs

The DRWT considered here has two equal-size rotors ($R_u/R_d = 1$), both made entirely of the DU-96-W180 airfoil with rotor-rotor separation of $0.3\,R_d$ and tip speed ratio $\lambda = 7.0$. Similar to test case 3, a different aerodynamic analysis solver is used to obtain radial profiles

of α and a, which are then prescribed as the desired performance outcomes. The vortex lattice method (VLM) proposed by Rosenberg and Sharma [126] is selected as the direct solver to analyze the DRWT. The objective is to see if the inverse solver is able to obtain a design that gives the desired aerodynamic performance (in this case, obtained using another wind turbine analysis software). The final results of the inverse design are shown in Fig. 3.10. The inverse design algorithm is able to obtain geometries for both rotors of the DRWT that satisfy the prescribed aerodynamic performance. As can be seen, there is a mismatch between desired and calculated output values at the last iteration of the inverse algorithm. As stated, to achieve a more realistic blade design, chord values are confined to the range of $0.01R$ to $0.2R$. In this test case, chord values at the tip region of downstream rotor have reached to the lowest limit ($0.01R_d$ in Fig. 3.10, bottom left) and this hinders the optimization algorithm to reproduce the target values.

3.4.2 Test Case 5: Inverse Design of DRWTs

The aim of this test case is to design a more realistic DRWT which has two rotors of different sizes, and the downstream rotor has different airfoils along its span. The upstream rotor is a Betz-optimum rotor, which uses only the DU-96-W180 airfoil and the downstream rotor uses the NREL Phase VI turbine rotor blades [135]. The NREL Phase VI turbine rotor uses the S809 airfoil from $r/R \geq 0.25$ to the tip, and cylinder at its blade root region; transition sections are not included. The 2D polar data of the S809 airfoil at chord-based Reynolds number, $Re_c = 5 \times 10^5$ were obtained using XFOIL [136]. Separation between the rotors is $0.3\,R_d$ with $R_u/R_d = 0.3$ and the tip speed ratio of either rotor, defined using its tip rotor radius, is 7.0. A test case similar to test case 2 is performed, in which the direct solver (RANS/ADM) is evoked with a known geometry (c and θ distributions for both rotors). The RANS/ADM computed α and a distributions for both rotor blades are then set as target values in the design process.

Initial estimates of c and θ for both rotors are constant values ($c_u = 0.03R_d$, $c_d = 0.07R_d$ and $\theta_u = \theta_d = 35°$) along the span. The converged geometry (c and θ) and aerodynamic performance (α and a) are presented in Fig. 3.11. The desired distributions of α and a are achieved through inverse design, and the converged geometry is identical to the originial geometry.

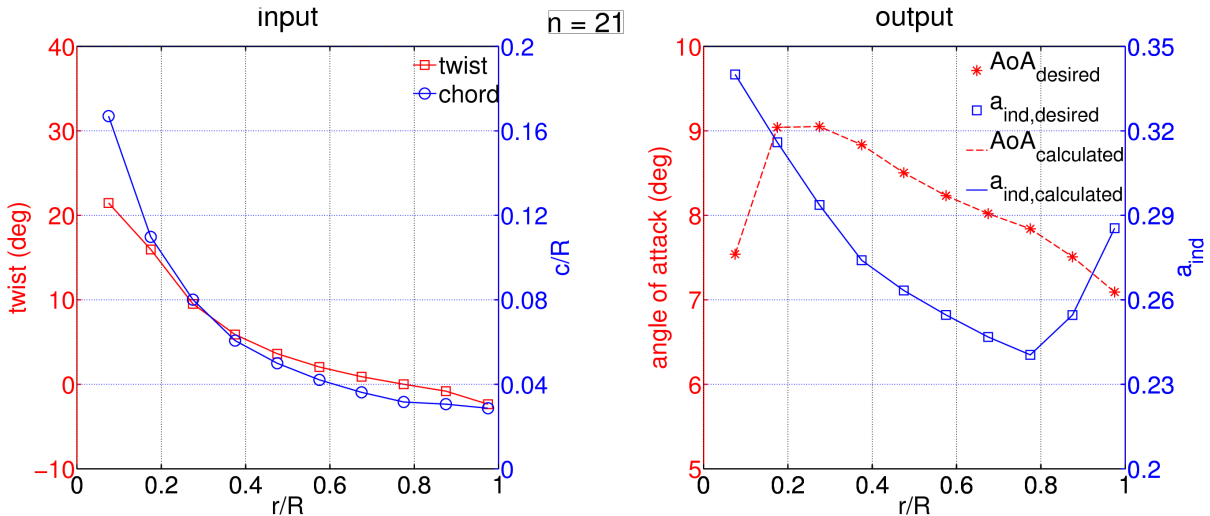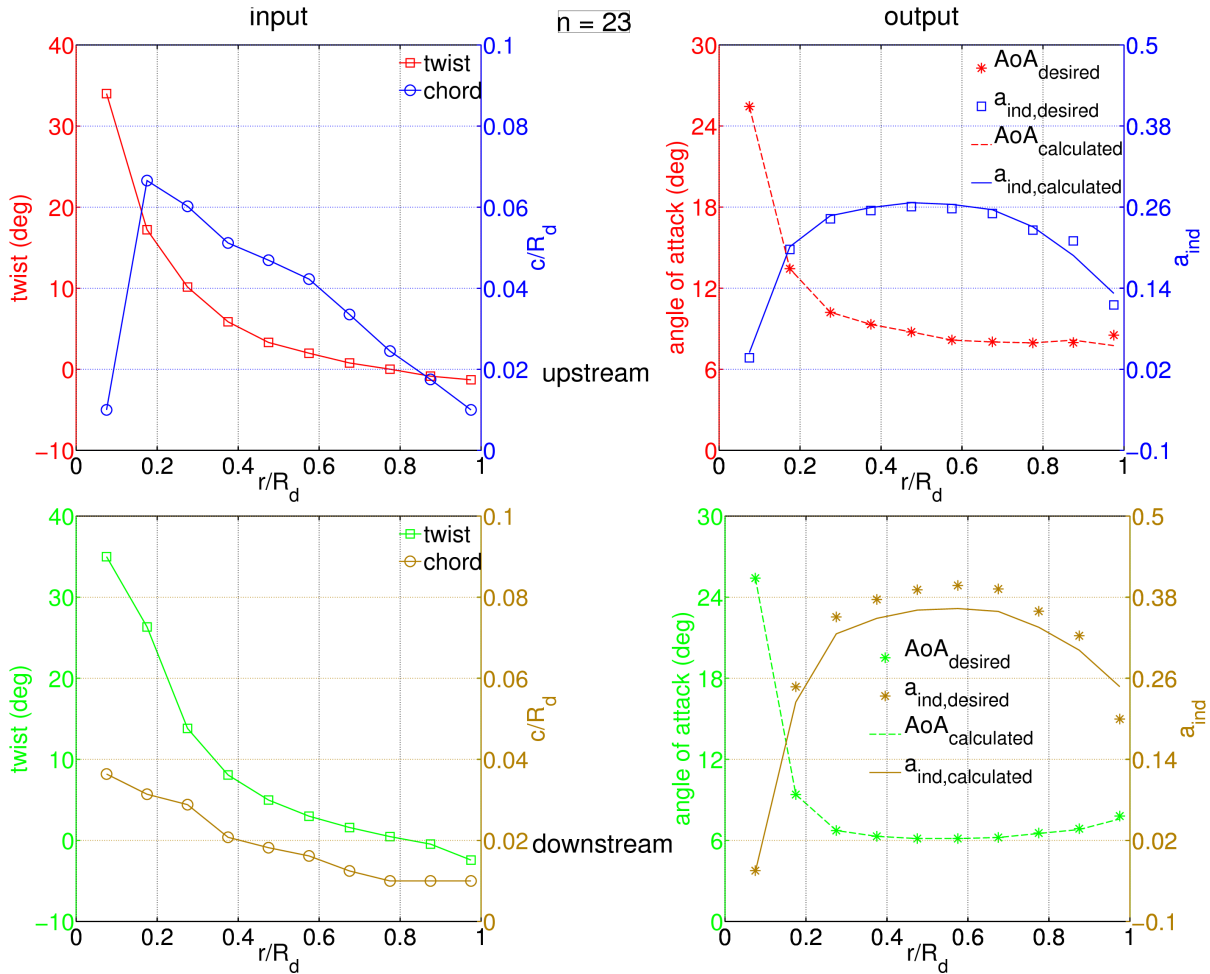Figure 3.10: Results for test case 4. Input (chord and twist distribution) and outpput (angle of attack and induction factor) for upstream and downstream rotors at the last iteration.

The Jacobian at the last iteration is shown in Fig. 3.12. As expected, the blocks in the diagonal (upper left and bottom right) quadrants are strongly diagonal because they represent the sensitivity of output parameters to the inputs of the same rotor (refer to the schematic in Fig. 3.9). The upper right quadrant shows the effect of input parameters of the downstream rotor on the output of the upstream rotor. This effect is almost negligible because the rotor-rotor separation distance $(= 0.3\,R_d)$ is too large for the potential field of the downstream rotor to substantially influence the upstream rotor aerodynamics. It should be noted that the only potential field captured here is due to the aerodynamic pressure; thickness effects are not modeled. Rosenberg and Sharma [126] has shown that thickness effects can be neglected at such separation distances.
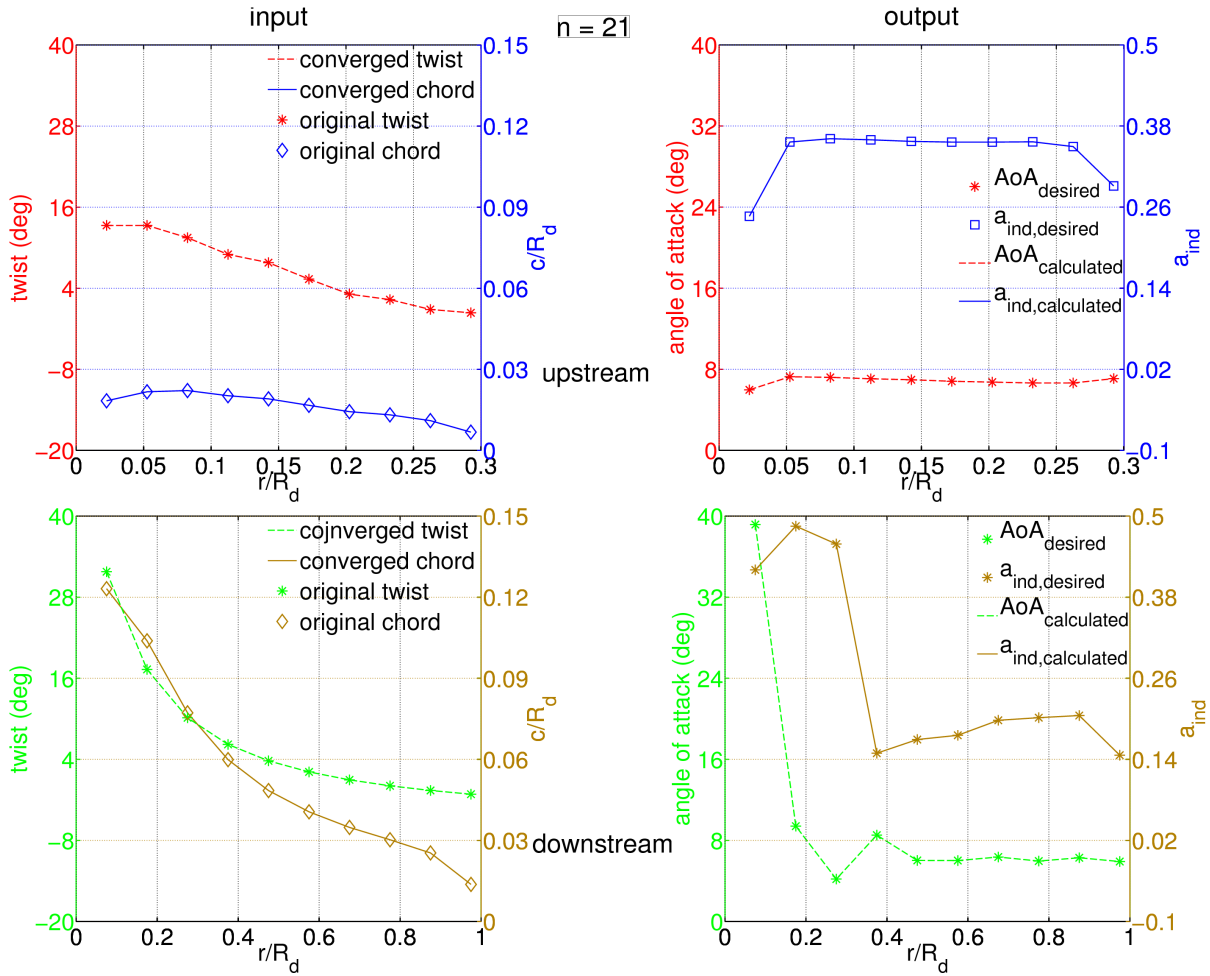
Figure 3.11: Results for test case 5. Converged input (chord and twist distribution) and outpput (angle of attack and induction factor) for upstream and downstream rotors at the last iteration.

Lastly, the bottom left quadrant has non-zero components up to the tip radius of the upstream rotor $(R_u/R_d = 0.3)$ since any change in the shape of the smaller upstream rotor will change the flow speed and angle in its wake and eventually the downstream rotor will be affected over a partial span. The downstream blade sections with $r > R_u \ (= 0.3 \, R_d$ here) will not experience much difference by changing the geometry of the upstream rotor.
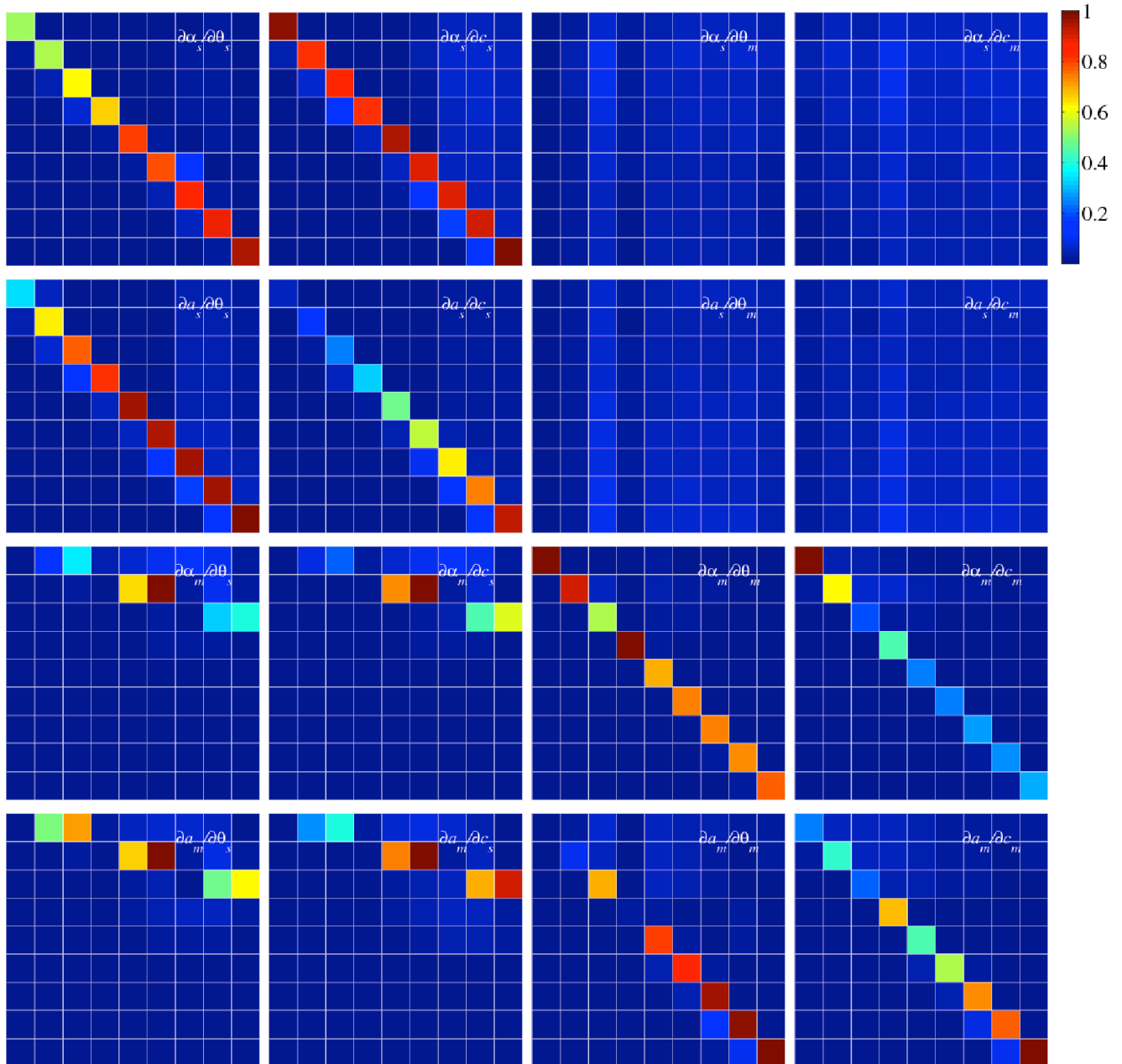
Figure 3.12: Blocks of the Jacobian matrix for test case 5

3.5 Conclusion

An inverse design algorithm for wind turbine blade design is presented in this paper. The goal is to realize the desired aerodynamic performance along the turbine blade by iteratively changing the blade geometry until convergence. The design parameters are axial induction

factor and angle of attack, while the independent variables are dimensionless chord and twist distributions along the blades. The inverse design procedure requires the flow field to be solved around the wind turbine blades. In this study, RANS/ADM is chosen as the direct solver to compute wind turbine aerodynamic performance. The design process involves minimizing a target function which is defined as the difference between the calculated and desired design parameters. The process starts with a user-provided initial estimate of independent variables and then it iteratively tries to improve this guess, based on the value of the target function. The trust-region-reflective is selected as the iterative searching method.

The design algorithm is tested with different single- and dual-rotor turbines. The purpose of each case is discussed and then the algorithm is put to the test to demonstrate its ability for accomplishing the design goal. In order to achieve a realistic design, constraints are applied to chord values. It's seen that when this constraint is not active (i.e. all the cases except test case 4), the proposed inverse design algorithm converges to the blade geometry that yields the desired aerodynamic performance. However, in test case 4 there is a small difference between desired and calculated values because of the active constraint.

Moreover, the trust-region-reflective (TRF) method is compared to the multi-dimensional Newton iteration method. It's found that while both methods are capable of handling the inverse problem and converge to the same input distributions, they have different convergence rates in differenet test cases. When the chord values met the constraint, Newton method exhibited oscillations before starting to decrease the target function. But when the constraints were not active, as in test case 3, the Newton method showed a faster convergence than the TRF. The TRF was more stable in constrained problems due to its gradual increase of the trust region.

Another objective of this study is to extend the blade design process to multi-rotor wind turbines. The analysis presented in this paper showed the ability of the design algorithm in obtaining the desired goal in DRWT cases. In addition, differences in SRWT and DRWT Jacobian matrices were discussed. Jacobian matrix quantifies the sensitivity of the output to the input parameters. For DRWT cases, it also demonstrates the interplay between the two rotors. It's seen that the geometry of the downstream rotor blade has a negligible effect on the

aerodynamic behavior of the upstream rotor for a relatively large rotor-rotor separation. The effect of upstream rotor blade shape on the aerodynamic response of the downstream rotor is remarkable up to the size of the upstream rotor.

CHAPTER 4.   ON DESIGNING WIND TURBINE ROTOR BLADES TO ENHANCE ENERGY CAPTURE IN WINDFARMS

Behnam Moghadassian and Anupam Sharma

Abstract

A method for inverse design of horizontal axis wind turbine (HAWT) blades is presented. The goal is to find turbine blade geometries that results in maximum output power from isolated wind turbines and wind farms. An iterative inverse algorithm is proposed to solve the design problem. The algorithm needs an initial guess for the blade geometry, a target function and two solvers: a direct solver to compute the target function, and an inverse solver to update the blade geometry in each iteration. The target function is defined as $f = -C_{P,tot}$, where $C_{P,tot}$ is the overall wind farm capacity. To calculate C_P values, the Reynolds Averaged Navier Stokes (RANS) equations in the domain are solved. The effect of turbine rotors is modeled as momentum sources using the actuator disk model (ADM). This computational fluid dynamics (CFD) approach is referred to as RANS/ADM and provides a good combination of the high fidelity offered by CFD at a relatively low cost. A previously validated implementation of this RANS/ADM in OpenFOAM is used to simulate wind turbine aerodynamics. The inverse solver in the design algorithm is the nonlinear least squares regression solver, trust-region-reflective (TRF) method. The Broyden method is used to reduce the computational time by approximating the Jacobian matrix instead of computing it. The inverse algorithm stops when the minimum of target function is reached. For manufacturability purpose, the distribution of chord and twist is smoothed out at each iteration. The method is first applied to conventional, single-rotor wind turbines (SRWTs) and then extended to multi-rotor, specifically dual-rotor wind turbines (DRWTs).

4.1 Introduction

In recent decades, wind turbine and wind industry has become an important part of the sustainable energy resources in the world. The goal of using a wind turbine is to transform the wind power into electrical power. Wind turbines have many common essential parts which have been improved throughout history in order to excel the performance of wind turbines [5]. For power transformation, wind causes rotation of turbine blades and this rotation is transferred via shaft to a gear box and eventually to a generator. So, the process of energy extraction starts when airflow reaches the blades. Blades of a typical horizontal axes wind turbine (HAWT) has airfoil cross-sections from root to tip. Lift force is generated along the blade when airflow passes airfoil shaped cross-sections. This lift force is the cause of blade rotation and eventually power generation.

Power generation from a wind turbine is strongly dependent on its blade geometry. Parameters such as size (length) of blades and radial distribution of chord and twist of the airfoils affect the wind turbine performance and aerodynamic behavior. Optimizing wind turbine aerodynamics and power extraction through blade shape design has attracted many researchers. Lee [45] employed an inverse approach to optimize the angle of attack and lift coefficient along the blade by changing the radial distribution of chord and twist. He used Blade Element Momentum Theory (BEMT) to find the aerodynamic parameters on turbine blades. He also applied Newton's method to search iteratively for the optimum blade design. Tahani *et al.* [53] used BEMT to find the optimal chord and twist distribution of blades of a 1 mega-Watt wind turbine that leads to the maximum power coefficient (C_P). They tested various airfoils and pointed out the differences in power extraction characteristics of each airfoil. They also linearized the chord and twist profiles to increase the manufacturability of their design. Liu *et al.* [52] investigated the blade design of a fixed-pitch fixed-speed (FPFS) horizontal-axis wind turbine to maximize the Annual Energy Production (AEP) for a wind turbine that works in wind sources with a known wind speed Weibull distribution. They linearized the chord and twist distribution on a heuristic basis to facilitate the blade manufacturing process.

In all the above works, the idea was to design an isolated wind turbine. However, wind turbines are usually working in wind farms with other turbines in the same location to capitalize the energy extraction. Large wind farms usually consist of multiple arrays of wind turbines. In this configuration, downstream turbines work partially/totally in the wake of upstream turbines. Wind turbines capture less energy when they work in the wake flow instead of an undisturbed inflow. Wake loss in wind farms is estimated to reduce the overall wind farm power capacity by $8 - 40\%$ and is one of the major reasons for deficit in the overall energy capture [137, 20]. Therefore, proper modeling of wake flow is needed to analyze wind farms. In practice, the accepted blade design of a wind turbine that works in isolation cannot be used for all turbines in a wind farm. It is because each row of turbines experiences a different incoming flow and should be designed accordingly.

The idea of this work is to design blades of wind turbines (working in isolation with undisturbed airflow or in the wake of upstream turbines) to maximize the total power of an array of turbines. To the authors' best knowledge, blade design of wind turbines to maximize the net power of a set of in-line turbines has not been studied before. Computationally cheap aerodynamic solvers, such as BEMT, are very popular in blade design of isolated wind turbines. However, they cannot be used in wind farms because they are unable to model the wake flow [54, 55]. In order to analyze aerodynamics of wind farms, one needs more complex methods that can model the wake. Computational cost of these methods is typically medium to high [56]. An efficient way to analyze the wake is to solve the Reynolds Averaged Navier Stokes (RANS) equations to calculate flow variables such as mean velocity and pressure. Reynolds stresses are found by various methods such as the $k - \omega$ [138] or the $k - \epsilon$ [139]. Resolving the turbine blades requires a very fine mesh and increases the computational cost drastically. A more affordable and favorite method among researchers is to represent the effect of rotating blades as body forces in the RANS momentum equation. This body force is estimated by Actuator Disk Model (ADM) [123] or Actuator Line Model (ALM) [122]. A combination of RANS with ADM or ALM can predict the far wake as well as mean loads on the wind turbine. It also models the wake rotation [56]. Researches have shown that RANS/ADM is computationally not very demanding and performs well in simulation of wake flow. Masters et al. [140] analyzed

the turbine wake dynamics in a tidal stream using RANS/ADM and found a good agreement between their predicted mid- to far wake velocity structures and experimental data. Van der Laan *et al.* [141] studied the turbine wake modeling for different arrays of wind turbines under neutral atmospheric stability. They used RANS/ADM simulation with an improved $k - \epsilon$ model and compared it to field measurements. They found a good agreement between their velocity profiles and turbulent intensities in turbine wakes and field data. When there were no field data, they compared RANS/ADM results to the Large Eddy Simulation (LES) with an ADM representation of blades (LES/ADM). These comparisons were also in very good agreement. They reported the computational costs of two simulation techniques (RANS/ADM and LES/ADM) and it clearly demonstrated the benefit of RANS/ADM by being much cheaper than LES/ADM. Shives and Crawford [142] analyzed the wake flow of different cases of side-by-side and in-line turbines. They noted a similar agreement between experimental data and RANS/ADM with $k - \omega$ turbulence closure model.

The objective of this paper is to develop and demonstrate a framework to design wind turbine blades so as to maximize the aggregate power capture in a wind farm. In order to demonstrate the concept, the worst-case scenario with the turbines in a row in perfect alignment with the freestream wind, is considered. A practical application would require consideration of the entire wind rose and optimization of turbine blades to maximize the annual energy production (AEP) of the wind farm.

Multiple cases with different number of in-line turbines are considered to demonstrate the capability of the proposed design process. An iterative inverse approach is used to perform the design. A user-defied initial guess for the geometry (i.e., chord and twist) of wind turbine blades is made. The RANS/ADM equations with the $k - \epsilon$ turbulence closure are solved to find the flow field and total power (algebraic sum of power from all turbines in the domain). If the total power is not at its maximum, a new blade geometry is calculated. Calculation of the new geometry is carried out by finding how much and in which direction the initial guess should change in order to have the maximum total power. The RANS/ADM then uses the new blade geometry to assess the flow parameters and total power. This process continues until the maximum of the total power is reached. In this work, the trust-region-reflective (TRF)

method is selected to prepare the new geometry at each iteration. TRF is a gradient-based nonlinear least squares minimization scheme that is suitable for bounded multi-variable and multi-objective optimization problems [48, 49]. Our inverse problem is bounded and multi-variable. The blades are divided into several sections with input variables as chord and twist of each section. In addition, to achieve a physically possible design, top and bottom constraints are placed on chord and twist values. As a common step in gradient-based searching algorithms, the Jacobian matrix is calculated. This matrix demonstrates the sensitivity of the output variable (here, total power) to all the input variables (chord and twist at different sections). It reveals useful information to the designer by providing an estimate of which input variables have the largest impact on the output. The distribution of chord and twist is smoothed out at each iteration of the inverse procedure in order to keep the manufacturability of the proposed final design.

4.2 Computational Model

An inverse approach has been used to numerically perform wind turbine blade design. Generally, the solution to an inverse problem requires two solvers: a direct solver (or model) to find the value of target function at any design point; and an inverse solver to find the optimum point of the target function iteratively. The definition of the target function and explanation of how direct and inverse solvers work are presented in this section.

4.2.1 Direct Solver

The direct solver in this study simulates the turbulent flow in a computational domain where in-line wind turbines are operating in full wake of the upstream rows. For flow simulation, the semi-implicit method for pressure linked equations (SIMPLE) algorithm [129] is used to solve the incompressible RANS equations. These equations are:

$$\frac{\partial \bar{u}_i}{\partial x_i} = 0, \text{ and,}$$
$$\bar{u}_j \frac{\partial \bar{u}_i}{\partial x_j} = -\frac{1}{\rho}\frac{\partial \bar{p}}{\partial x_i} - \nu \frac{\partial^2 \bar{u}_i}{\partial x_j{}^2} - \frac{\partial \overline{u'_i u'_j}}{\partial x_j} + \frac{f_i}{\rho}. \tag{4.1}$$

Reynolds stresses are obtained using the two-equation $k - \epsilon$ turbulence closure model suggested by Launder and Spalding [130] and modified by Hargreaves and Wright [131]. The effect of rotating turbine blades on the flow is represented by the momentum *sinks* (f_i) in the RANS equations. The actuator disk model (ADM) is used to estimate f_i. In the ADM, the effect of the rotor blades is modeled by a disk over which a body force is applied. This disk is discretized into several annular elements. Based on the ADM formulation, the f_i at each element of the disk is a function of the local flow velocity vector, the number of blades, the turbine rotational speed, the chord and twist distributions along the blade and the airfoil polars (C_l and C_d versus angle of attack). The finite blade length effects are modeled using Prandtl's tip loss correction [143]. The body force f_i is distributed over the disk with a Gaussian distribution [32]. A numerical code to perform ADM calculations was developed and implemented in the unstructured, finite volume solver simpleFOAM (part of OpenFOAM) and has been previously validated against experimental measurements [16, 121, 132]. for wind turbine power and aerodynamic performance prediction.

4.2.2 Inverse Solver

The trust-region-reflective (TRF) is selected as the inverse solver. TRF is a non-linear least squares method to minimize a multi-variable and multi-objective target function in a bounded or unbounded domain. The goal of our study is to maximize the total power from a set of wind turbines. Therefore, the target function is defined as $f = -C_{P,tot}$. Minimizing this function means $C_{P,tot}$ is at its maximum. f is a function of different parameters such as tip speed ratios of different turbines, geometry of each blade, distance between turbines, yaw angle. etc. The focus of this study is to minimize F through changing the geometry of blades. So, other involving parameters are kept constant. Blade geometry consists of radial distribution of chord and twist of each blade. Blades are divided into multiple elements and chord and twist of each element is found to maximize the total power from the wind farm. A brief introduction of TRF in a 1-D problem is given below. The algorithm remains the same for higher dimensions (like in our case).

Suppose the minimum of a function f is sought in a bounded or unbounded domain. As a first guess, a point x_0 in the domain is randomly picked and the function f is evaluated at x_0. The essential idea behind this method is to approximate f with a simpler function q (see Eq. 4.2) that behaves similarly to f in the vicinity (trust region, N) of x_0 and find a new point x_1 in N where q is minimum. Now if the reduction in the approximated function (q) is also inherited by the original function f, x_1 is accepted as an updated estimate of the location of minimum value of f, and the procedure is repeated. Otherwise the trust region (N) is reduced in size and the search for minimum q is repeated. In order to reduce the computational time, the trust-region sub-problems are confined to two dimensional sub-spaces S. In fact, the sub-problem is defined as

$$\arg\min\{q(s)\}, \text{ subject to } ||Ds|| \leq \Delta \text{ and } s \in \text{span}[s_k^U, s_k^{FS}], \qquad (4.2)$$

where, $q(s) = f(x_k) + s^T g + \frac{1}{2} s^T H s$, is the approximation for f around x_k, g is the gradient of f at x_k, and H is the Hessian matrix (symmetric matrix of second derivatives of f), D is the diagonal scaling matrix, Δ is the radius of the trust region, s_k^U is the steepest descent direction given by $s_k^U = -g\,(g^T g)/(g^T H g)$, and s_k^{FS} is either an approximate Newton direction, $H \cdot s_k^{FS} = -g$, or a direction of negative curvature, $(s^{FS})_k^T \cdot H \cdot s_k^{FS} < 0$. This formulation results in global convergence through the steepest descent or negative curvature direction while achieving a fast local convergence, when it exists, using the Newton step [48, 134] in each trust region.

4.2.3 Jacobian Update Scheme

A required step in gradient-based optimization methods (such as TRF) is to compute the Jacobian, $\mathbf{J} = \partial f/\partial \mathbf{x}$, which shows the sensitivity of the target function to the input arguments. The Jacobian is needed by the algorithm at each iteration of the inverse solver, and is typically evaluated numerically using a finite difference scheme with multiple runs of the direct solver. For a multi-variable problem, calculation of the Jacobian can become very computationally expensive, particularly when a higher fidelity direct solver is used. To find each element of $\mathbf{J}$, using finite differencing method (FDM) for example, the direct solver has to be called twice

(for $x_i + \epsilon$ for a forward differencing scheme). Therefore, the direct solver has to be called $n+1$ times to calculate all elements of $\mathbf{J}$, where n is the length of $\mathbf{x}$. In this work, $n = 20$ for the least computationally demanding case study (design of a SRWT) as the blades are discretized into ten elements and chord and twist on each element form the $\mathbf{x}$ vector. Therefore, the direct solver needs to be run 21 times in each iteration of the inverse solver.

One approach to reducing the computational cost is to use a *quasi-Newton* scheme [144] to update the Jacobian. The idea of quasi-Newton methods is to approximate the Jacobian, as opposed to computing it precisely [145]. In many methods, simple recursive formulae are used to relate $\mathbf{B}_{k+1}^{-1}$ to $\mathbf{B}_k^{-1}$, where $\mathbf{B}_k$ is an approximation for the $\mathbf{J}_k$ (Jacobian at k-th iteration). These formulae typically do not involve finding derivatives at all [146]. In this study, we have used Broyden's method [57]. The idea is to calculate the Jacobian at the first iteration of the inverse solver ($\mathbf{J}_0$) using the forward finite difference formula and approximate it for later iterations using the following algorithm.

$$\mathbf{J_n} = \mathbf{J_{n-1}} + \frac{(f_n - f_{n-1}) - \mathbf{J_{n-1}}(\mathbf{x_n} - \mathbf{x_{n-1}})}{||\mathbf{x_n} - \mathbf{x_{n-1}}||^2}(\mathbf{x_n} - \mathbf{x_{n-1}})^T \tag{4.3}$$

Using this method, the direct solver needs to be called just once to calculate the target function at each iteration of the inverse solver, except for the first iteration. To make sure that the search for the optimum point of f is carried out accurately, in this study the Jacobian matrix is computed by the forward finite difference formula every 5 iterations of the inverse solver.

4.3   Results and Discussions

The proposed inverse design procedure is tested for conventional, single rotor wind turbines (SRWTs) and the novel dual rotor wind turbine (DRWT) proposed in Ref.[16]. A total of four turbine/windfarm design problems (Test Cases) are investigated. The purpose of these tests is to verify that the algorithm is capable of obtaining blade geometries which enhance wind turbine or wind farm power output in comparison to the baseline. A description of the test cases and the performance of the proposed inverse design technique are presented in this

section. Grid independence has been already been established for direct solver with the same computational set-up in Ref. [147], and hence is not repeated here.

By using the RANS/ADM method for the direct solver, designers can model the wake flow and are able to design the turbines in the wake and extend blade design approaches beyond the design of isolated wind turbines only. For optimization, the nonlinear least-square solver package *scipy.optimize*, available with the *Python* scripting language is employed. The proposed inverse algorithm requires the designer to input an initial guess for the blade shape. In this study, initial guesses are either arbitrary or have been obtained from previous cases. To achieve manufacturable and realistic blade designs, top and bottom limits are set for chord and twist values. In addition, chord and twist profiles are smoothed out prior to each iteration of the inverse loop.

4.3.1 Inverse Design of a Turbine Operating in Isolation

4.3.1.1 Isolated Single Rotor Wind Turbine

The inverse design procedure is first verified for a conventional, single-rotor wind turbine (SRWT) operating in isolation in uniform inflow. The inverse algorithm seeks to find the turbine rotor blade geometry (chord and twist distributions) that maximizes the power extracted (measured with the nondimensional power coefficient, C_P) by the turbine. For simplicity, the turbine blade is desired to be designed using one airfoil (DU-96-W180) for the entire blade span. The DU-96-W180 airfoil has a high lift-to-drag ratio and is typically used in the outboard region of long turbine blades [16]. The design tip speed ratio, $\lambda = \Omega\,R/u_\infty$ is set to be 7.0.

Figure 4.1 (a) shows the axisymmetric grid (one-cell thick in the circumferential direction) used for the simulations. The blade chord and twist distributions are assumed to be uniform everywhere along the entire blade as the initial guess for the first iteration: $(c/R)^{(0)} = 0.08$ and $\theta^{(0)} = 60°$; the initial guess is far from the final distributions. The procedure converges in 17 iterations of the inverse solver. Figure 4.1 (b) shows the converged chord and twist distributions.

The 1-D momentum theory, credited to Albert Betz, suggests that an axial induction of $1/3$ gives the maximum C_P. A *Betz optimum* rotor was designed using the inverse design procedure described in Refs. [147, 148], which utilizes the same RANS/ADM solver as used here, however that design procedure aims to achieve a constant $a = 1/3$ throughout the blade span rather than maximizing C_P. The aerodynamic performance, measured as C_P gives the following result: $C_{P,Betz} = 0.524$ and $C_{P,max(C_P)} = 0.572$. An increase of about 9% in C_P is observed with the new design obtained using the proposed inverse design procedure. Figure 4.1 (b) compares the chord and twist distributions of the blades of the two turbines. Figure 4.1 (c) compares the a distribution between the two rotors. The largest differences are found to be in the blade root and the blade tip regions, where finite-span effects, unaccounted for in the 1D momentum theory, are in play.

4.3.1.2   Isolated Dual Rotor Wind Turbine

One of the objectives of the DRWT technology is to mitigate blade root loss. The bending moment loads of utility-scale, multi-megawatt turbine blades is very high; these blades are therefore designed for structural integrity rather than for high aerodynamic performance in the blade root region. Furthermore, blades of utility-scale turbines, such as the NREL 5 MW conceptual turbine, utilize different airfoils along thei span. In some cases, up to around 10% of the inner blade region has a cylindrical cross section, which does not contribute to power production; in fact it generates negative torque and hence negates the power produced in the outboard region.

The idea of the DRWT technology [16] is to use a small, secondary rotor upstream of the large, main rotor. The secondary rotor of the DRWT efficiently captures the energy in the wind flowing through the root region (inner 25%) of the main rotor blades. The DRWT technology has been numerically demonstrated to increase energy capture by up to 5% when in realistic, atmospheric boundary layer operation; the percentage increase is dependent on the atmospheric stability condition [25]. The main rotor of the DRWT considered here is the same as the NREL 5 MW conceptual turbine [36] rotor, and the secondary rotor is designed using only the DU-96-W180 airfoil along its entire blade span. The rotor-rotor separation distance is
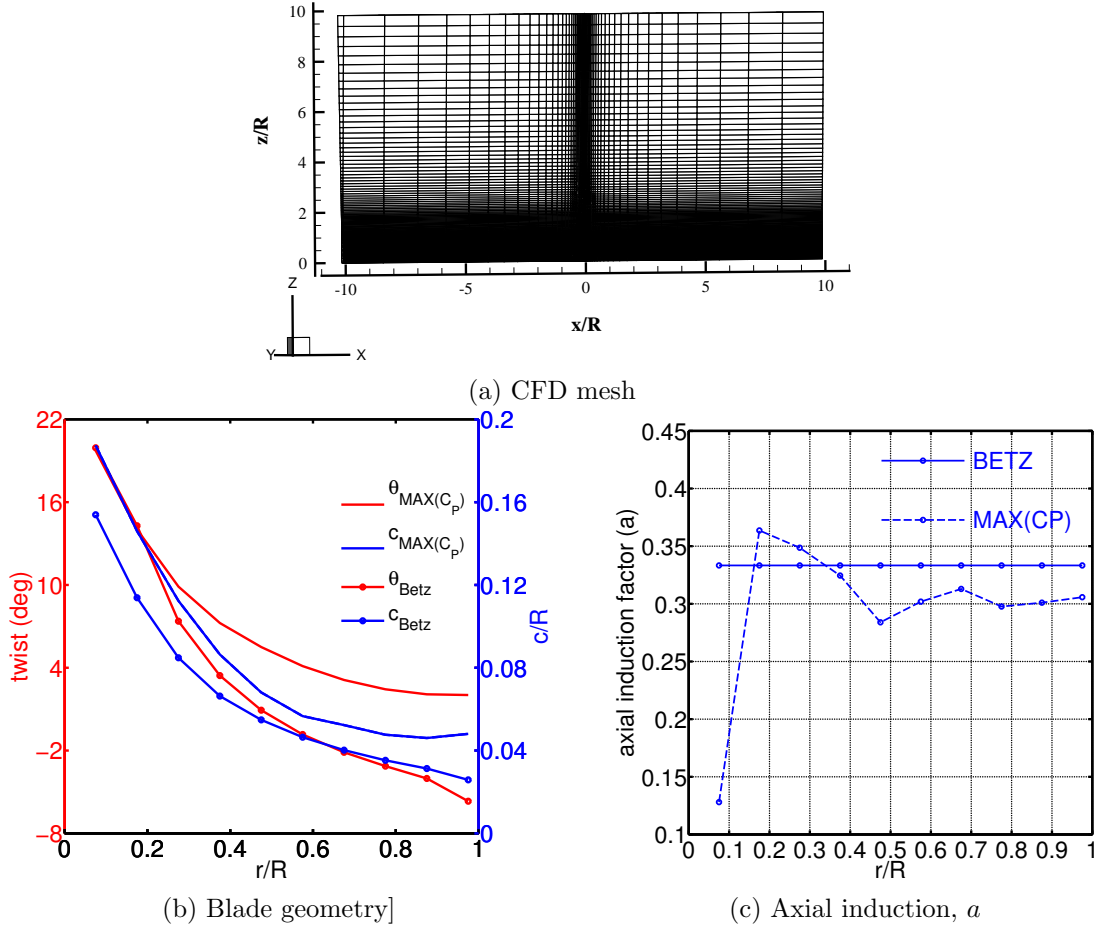
Figure 4.1: Inverse design of a SRWT: (a) computational mesh (mesh density is reduced for clarity), (b) geometry of the blade obtained using the proposed inverse design compared with Betz optimum rotor design, and (c) comparison of axial induction factor (a) distribution between the two designs.

30% of the main rotor tip radius. Both rotors are modeled as actuator disks and their design tip speed ratio is set to be 7.0.

The mesh is modified to carry out the inverse design analysis for DRWTs and finer mesh is used around both rotors. The inverse design is carried out in three stages: First, the aerodynamic performance of the baseline, NREL 5 MW turbine (referred to as baseline) is analyzed using the RANS/ADM direct solver. The RANS/ADM analysis predicts the baseline turbine power coefficient, $C_{P_{\text{Base}}} = 0.52$.

In the next step, the turbine blades are redesigned to maximize C_P for the NREL 5 MW turbine (SRWT) operating in isolation; the process is exactly the same as in Sec. 4.3.1.1, but is

performed for the NREL 5 MW turbine blades, which use different airfoils along the span. The independent variables for this problem are the radial distributions of θ and c of the turbine rotor blades, and the target is to maximize the C_P of the turbine. The redesigned turbine yields a 13% increase in performance with power coefficient, $C_{P_\text{Redesigned}} = 0.588$. Figure 4.2 compares the chord and twist distributions for the baseline and the redesigned DRWT.

In the final step, a DRWT is designed so as to maximize the aggregate power captured by the main and the secondary rotors of the DRWT. The independent variables for this problem are the θ and c distributions for *both* the main and secondary rotors. The objective of the inverse design is to maximize the turbine power coefficient (C_{P_DRWT}), which is defined as the total power extracted by the two rotors of the DRWT normalized by the power in the air stream that passes through the area swept by the main rotor. Note that C_{P_DRWT} is equivalent to the area weighted sum of the C_P of the individual rotors.

$$C_{P_\text{DRWT}} = \frac{2\left(P_m + P_s\right)}{\rho_\infty u_\infty^3 A_m} = \frac{A_m\, C_{P_m} + A_s\, C_{P_s}}{A_m}, \tag{4.4}$$

where the subscripts m and s denote that the quantity corresponds to the main rotor and the secondary rotor respectively. The converged values of C_P in each case can be found in Table 4.1. The optimized DRWT gives a C_{P_DRWT} of 0.604, which is an increase in C_P of 16.2% over the baseline SRWT and a 2.7% over the redesigned SRWT.

For redesigning the baseline turbine and designing DRWT, the inverse algorithm converged to the same blade geometries with and without the Broyden method for updating the Jacobian matrix. However, approximating the Jacobian matrix by Broyden method is less computationally demanding, according to Table 4.1.

Table 4.1: Aerodynamic power coefficients, number of iterations to converge (N), and relative computational costs of the different turbine designs.

Turbine type	Power coefficient	% increase over baseline	N (FDM)	N (Broyden)	relative costs (Broyden:FDM)
Baseline	0.520	-	-	-	-
Redesigned baseline	0.588	13	16	28	1:3.2
DRWT design	0.604	16.2	19	27	1:3.8

(a) Baseline v/s redesigned SRWT

(b) Redesigned SRWT v/s DRWT
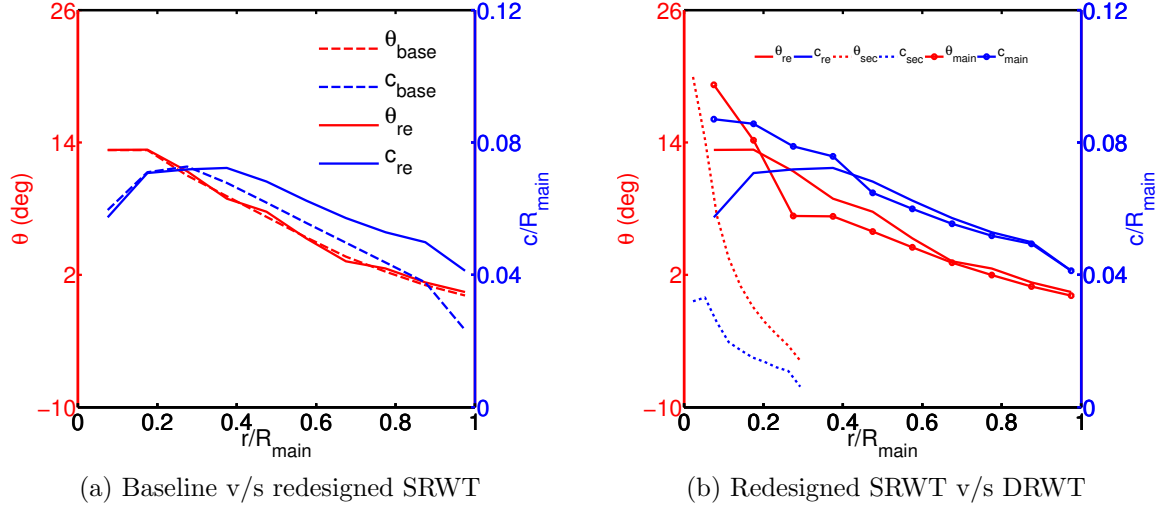
Figure 4.2: Comparisons of the chord and twist distributions between: (a) the baseline (NREL 5MW conceputal turbine) and the redesigned SRWT, and (b) between the DRWT and the redesigned SRWT.

4.3.2 Turbine Design for Maximizing Windfarm Power Output

As discussed in Section 4.1, the primary reason for using a higher fidelity and a computationally demanding method such as the RANS/ADM, as opposed to the commonly used BEMT based methods, is to extend the blade design methodology to wind farm applications. In other words, the objective is to design turbine blades such that the wind farm power output, as opposed to individual turbine output, is maximized. For the purposes of demonstrating the concept, only the configuration with the turbines directly in the wake of each other is considered. This simplification allows makes the problem axisymmetric, and dramatically reduces the required computing time. Extension to staggered turbines is straightforward but computationally expensive.

There are at least two different ways to pose the blade design problem for an array of turbines. One is to design each turbine separately, i.e., every turbine in the windfarm can have a different geometric design. We will call is *Approach 1*. However, this is undesirable from manufacturing cost and complexity perspectives; it is much more cost effective and simpler to have one geometry for all the turbines in a windfarm. The second way to approach the blade design problem is to impose the constraint that all turbines should have the same geometry. The objective then is to find this one blade geometry that would maximize the power output

from a windfarm. This will be referred to as *Apprach 2*. Results from both design approaches are compared in the following sections.

4.3.2.1   Windfarm with Three In-line SRWTs

Three in-line turbines (SRWTs) aligned with the incoming wind are considered. All turbines have the same tip speed ratio, $\lambda = 7$ and use one airfoil (DU-96-W180) throughout the blade span. The initial guess of the blade geometry for the inverse algorithm is taken to be the geometry that gives maximum C_P when operating in isolation (design procedure presented in Sec. 4.3.1.1).

The objective is to improve the total power captured in windfarms. In order to compare windfarm performance between different design approaches, a farm-averaged turbine aerodynamic power coefficient is defined,

$$C_{P_{\text{av}}} = \frac{2}{\rho u_\infty^3 A} \frac{1}{N} \sum_{i=1}^{N} P_i, \tag{4.5}$$

where the P_i denotes the power output of each of the N turbines in the farm, and A is the area swept by a turbine rotor (rotor diameter is maintained across turbines). This definition is equivalent to the average C_P of all the turbines in a windfarm if the freestream wind speed (far upstream of the windfarm) is used for power normalization.

Turbine rotor blade design is carried out for this three-turbine windfarm using Approaches 1 and 2 described earlier (see Fig. 4.3 (a)). Table 4.2 lists the $C_{P_{\text{av}}}$ for each case. As expected, when each turbine rotor geometry is allowed to vary independent of the other turbines, the increase in wind farm energy capture is highest (about 9.7%). When all the turbines are required to have the same geometry, there is still a substantial (5.3%) increase in windfarm energy capture. While the first approach leads to a higher farm output, the difference may not justify the added cost and complexity associated with manufacturing three different blade designs.

Table 4.2: Windfarm average turbine power coefficients for the two different design approaches compared against the baseline.

Windfarm type	$C_{P_{\mathrm{av}}}$	% increase over baseline
C_P max for isolated turbine operation	0.340	-
Different geometry for each turbine	0.373	9.7%
One geometry for all turbines	0.358	5.3%

Figure 4.3 (b) compares the individual turbine C_P (note that $C_P = P/0.5\rho u_\infty^3 A$ where u_∞ is the flow speed far upstream of the windfarm. In general the two windfarm design approaches suggest lowering the power capture from the first turbine to enhance power capture from the downstream turbines. In doing so, the overall windfarm energy capture is enhanced.

(a) Contours of axial velocity (b) C_P of individual turbines
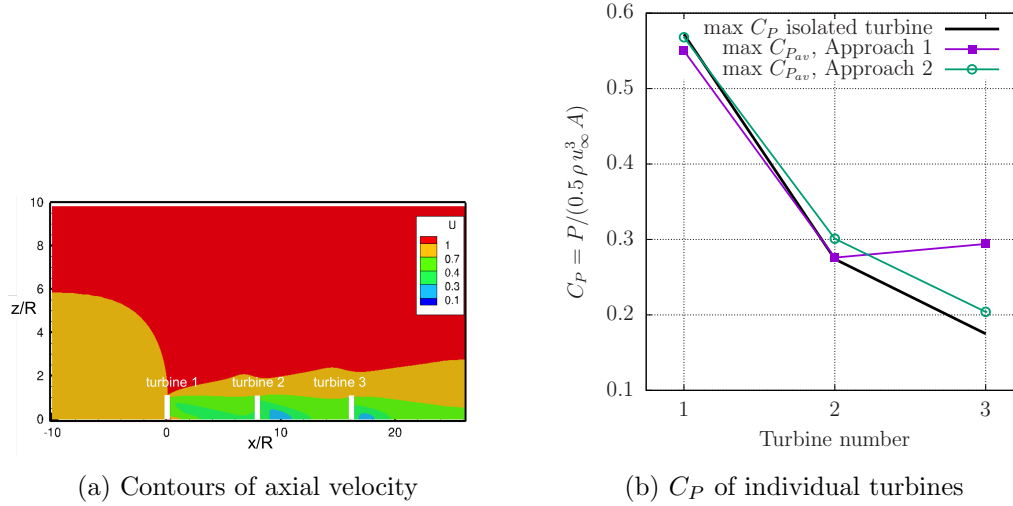
Figure 4.3: Design of a three-turbine wind farm using multiple design approaches. (a) Contours of axial velocity from a windfarm simulation with three in-line wind turbines, and (b) normalized individual turbine power compared between three cases: (1) turbines optimized for isolated operation, and (2 & 3) optimized for max windfarm power using Approach A and Approach B respectively.

Figure 4.4 shows the geometry of each of the three turbines in the windfarm obtained using Approach 1. It is interesting to note that the inverse design procedure suggests larger changes in the blade root region compared to the blade outboard region. Figure 4.5 shows the radial profiles of blade shapes obtained for the same three-turbine wind farm using Approach 2.
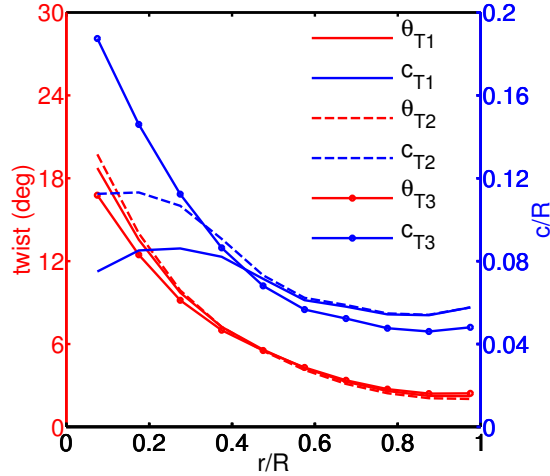
Figure 4.4: Chord and twist distributions of each turbine in the three-turbine windfarm obtained using Approach 1 to maximize windfarm power output.
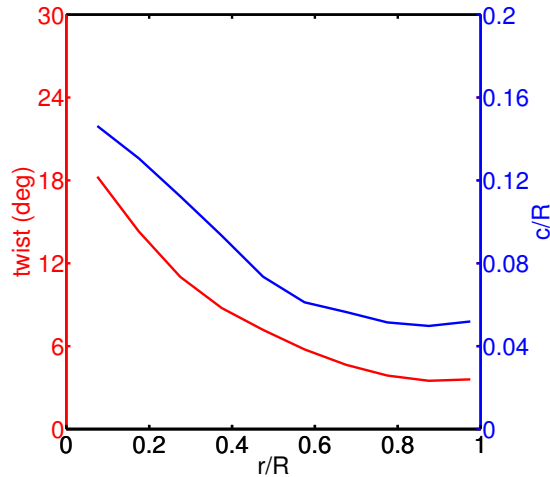
Figure 4.5: Chord and twist distributions of the turbines in the three-turbine windfarm obtained using Appraoch 2 to maximize windfarm power output. All turbines have the same geometry.

4.3.2.2   Windfarm with Ten In-line SRWTs

Modern windfarms consists of hundreds of turbines arranged in arrays, where deep array effects play a dominant role. Deep array effect are typically observed beyond (downstream of) the first 3-5 rows of turbines. A ten-array windfarm is considered, which is representative of large wind farms with multiple rows of turbines experiencing deep array effects. As in the previous example, all turbines are co-linear and aligned with the wind direction. The objective in this case is still the same: to design turbine rotor blades to maximize total energy capture from the windfarm. However, only Approch 2 is used for inverse design, as it is unreasonable to

expect 10 different blades designs in a windfarm. Furthermore, the turbines experiencing deep array effects are expected to have a similar design as the flow becomes statistically stationally in deep arrays. As in the case of the three-turbine farm, the initial guess for rotor blade geometry is taken to be the one that gives maximum C_P in isolated operation (result presented in Sec. 4.3.1.1).

With design Approach 2, the increase in farm-averaged power coefficient, $C_{P_{\mathrm{av}}}$ is predicted to be approximately 47%, which is a huge improvement in energy capture. It should be noted however that this anlaysis is limited to the case of in-line turbines, which is the worst-case scenario of operation of a windfarm. Actual benefits realized in a real windfarm are therefore expected to be smaller, but still substantial.

Figure 4.6 (a) shows the convergence history of $C_{P_{\mathrm{av}}}$ through the inverse design procedure. Windfarm energy capture monotonically increases as the inverse algorithm proceeds, and converges to the final solution in 12 iterations. Figure 4.6 (b) shows the C_P of each turbine in the wind farm scaled by the C_P of the first (most upstream) turbine. Results are shown for the first and last iteration of the inverse cycle. The initial design of turbines (aimed at maximizing C_P in isolated operation) extract more energy with the first few turbines but the power extraction then drops substantially for downstream turbines. The final design however, sacrifices energy capture in the upstream turbines to increase the total energy capture from the windfarm. Note that C_P in Fig. 4.6 (b) is scaled by the C_P of the first turbine ($C_{P,Turb\#1}$), which changes as the design algorithm proceeds. For the first iteration is $C_{P,Turb\#1} = 0.572$, and for the last iteration it is 0.503.

Figure 4.7 shows the converged blade geometry. The chord distribution of the converged design is highly unconventional, which much smaller chord values in the blade root region. This distribution allows high-momentum fluid to slip through the blade root region and allow higher momentum extraction from the downstream turbines. Blade twist is increased, likely to ensure that the turbines operate close to the angle of attack where the airfoil has the highest lift-to-drag ratio.
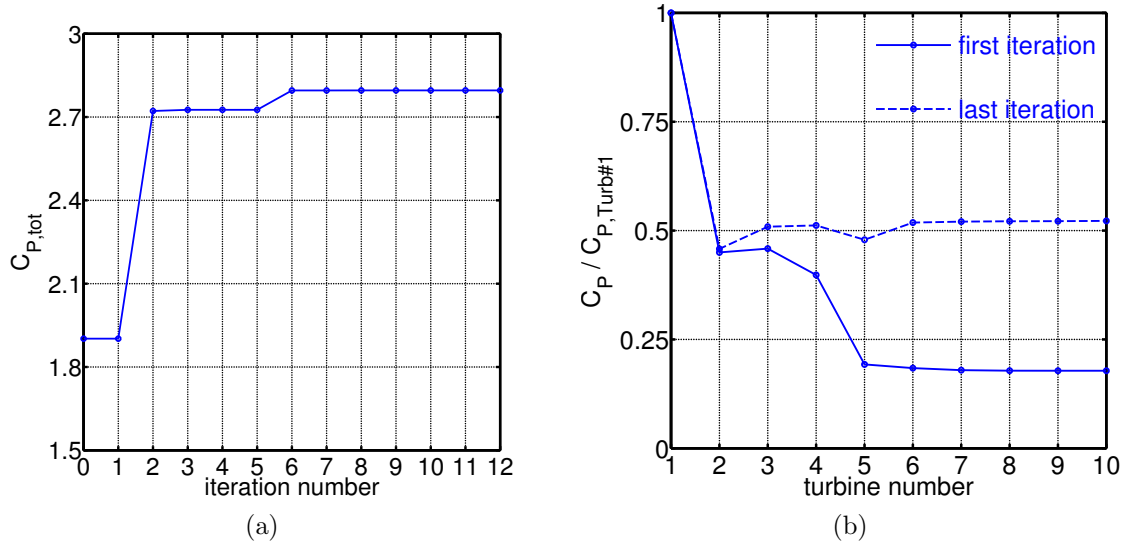
Figure 4.6: Results of inverse design of the ten-turbine windfarm: (a) convergence history of C_{P_av}, (b) C_P of each turbine in the farm normalized by $C_{P,Turb\#1}$.

4.4 Conclusions

An inverse algorithm for geometric blade design of horizontal axis wind turbine (HAWT) is presented in this study. The goal is to maximize energy capture from isolated HAWTs and the overall windfarm capacity by finding turbine blade geometries. Design of single rotor wind turbines (SRWTs) as well as dual rotor wind turbines (DRWTs) are considered. To perform the the aerodynamic analysis in the design procedure, the Reynolds Averaged Navier Stokes (RANS) equations are solved. Turbine rotors being modeled by the actuator disk method (ADM). The trust region reflective (TRF) is employed to perform the iterative search for the optimal blade geometry. The TRF is combined with the Broyden method which saves up to almost 75% of computational time by recursively updating the Jacobian matrix instead of computing the entire matrix.

The algorithm is first tested for isolated wind turbines. Blades of a wind turbine that has DU-96-W180 airfoil throughout the blade span are designed for maximum energy capture. The dimensionless power coefficient (C_P) of this design is about 9% higher than the C_P obtained from the Betz optimal design of the same blade (that has the axial induction of 1/3 along the blade). The largest difference between the two designs is observed at the blade root and the blade tip.
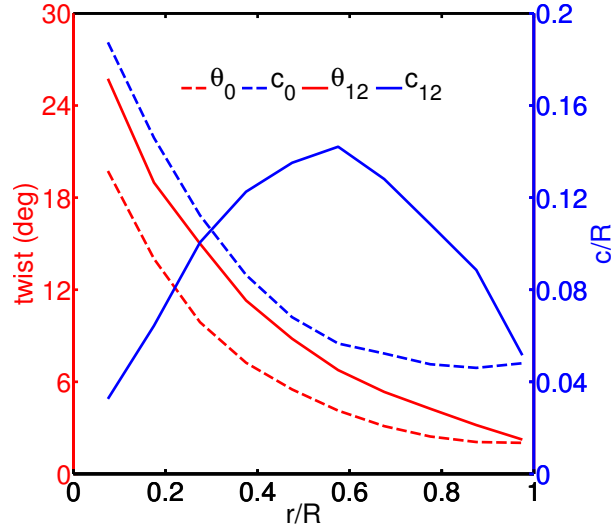
Figure 4.7: Radial profiles of chord and twist of optimized turbines for the ten-turbine windfarm case.

Redesigning the blades of the NREL 5MW turbine to achieve maximum power shows 13% increase in C_P compared to its original (baseline) design. Then blade design of a DRWT is considered. This DRWT has the NREL 5MW turbine rotor as the main rotor; and the secondary rotor has DU-96-W180 airfoil along its entire blade span. When both rotors of the DRWT are designed, the increase in energy capture reaches to 16.2% compared to the baseline NREL 5MW turbine rotor design.

Solving RANS/ADM equations instead of using methods that are based on the blade element momentum theory has made the design algorithm suitable for windfarm applications, where the wake flow modeling/prediction is required. Two approaches are considered in designing turbine blades for windfarms: 1) to design each turbine separately and 2) to have the same blade geometry for all turbines. For a case of three in-line SRWTs, it is found that the first approach results in higher farm-averaged power coefficient ($C_{P_{av}}$) than the second approach. However, the difference may not justify the added cost and complexity of manufacturing three different blade designs.

To examine the inverse algorithm in a windfarm with deep array effects, design of ten in-line SRWTs using the second approach is considered. The remarkable gain in $C_{P_{av}}$ by this approach compared to the baseline blade geometry (SRWTs designed without the wake effect)

is achieved by diminishing energy capture from upstream turbines, but increasing the energy capture from the downstream turbines.

CHAPTER 5.   CONCLUSIONS

Different numerical techniques were employed to analyze aerodynamic performance and loads of horizontal axis wind turbines (HAWTs) as well as to design turbine blades. The ultimate goal of this research was to evaluate novel ideas to enhance energy capture in windfarms and examine the recently proposed concept of dual rotor wind turbine (DRWT) that was aimed at mitigating blade root and wake losses.

Analysis of DRWTs and comparisons to single rotor wind turbines (SRWTs) were discussed in Chapter 2. For analysis purposes, a high-fidelity model (Large Eddy Simulation, LES) was employed to perform numerical simulations of wind turbines operating in the atmospheric boundary layer (ABL). A two-step procedure was used for the simulations. These two steps were the precursor run, which simulated the ABL in a large domain without the turbines, followed by the main run, that simulated the turbine operating in the ABL. Uniform flow as well as neutral and stable ABL conditions were investigated. Effect of the rotating turbine blades on the airflow was estimated by the Actuator Line Model (ALM). In the DRWT cases, the main rotor was chosen to be the rotor of the conceptual NREL 5 MW turbine and the secondary rotor was designed using the DU-96 airfoil along the entire blade span. The solver was first validated against experimental data for the three-bladed, stall-controlled, 100 kW Tellus (Riso) turbine. Improvements in power extraction (C_P) of 5 to 6% for all inflow conditions were observed for the DRWT compared to the SRWTs. The enhancement in C_P was obtained due to efficient extraction of energy from the streamtube going through the blade root region. The DRWT also enhanced wake mixing and entrainment of higher momentum fluid from outside the wake layer when the atmospheric turbulence was moderately high (as in the neutral stability case). A modest increase (up to 3.2%) in momentum entrainment was observed for DRWTs. Unsteady aerodynamic loads (measured as rotor power and out-of-plane blade root moment)

showed negligible reduction for the main rotor in the DRWT. Spectral analysis demonstrated that unsteady fluctuations in rotor power happened at the blade passing frequency, while fluctuations in blade root moments were at the rotor passing frequency and its harmonics. These fluctuations were attributed to the turbulence in the wind and variations with hight (due to the ABL) in the incoming mean wind.

In Chapter 3, the focus is on the inverse design of wind turbine blades and extension of the inverse design methodology to DRWTs. The inverse design problem was to find the turbine blade geometry that resulted in the desired (prescribed) aerodynamic behavior of the wind turbine. Blade geometry was defined by radial distributions of chord and twist while aerodynamic behavior was quantified by distributions of angle of attack and axial induction factor along the blade. A new algorithm for solving the design problem was proposed. The aerodynamic (direct) problem was solved by combining the Reynolds Averaged Navier Stokes (RANS) equations with the Actuator Disk Model (ADM). The inverse problem was solved using the trust region reflective (TRF) method, which is an iterative method to solve the constrained nonlinear least square curve fitting problems. The Jacobian (sensitivity) matrix was computed by a forward finite difference formula. The design algorithm was tested with different single- and dual-rotor wind turbines. The TRF method was compared to the commonly-used multi-dimensional Newton iteration method. Both methods were capable of handling the inverse problem, and converged to the same blade geometry. However, they had different convergence rates depending on whether or not the constraints on blade chord were imposed. In general, the TRF method was found to be more stable in constrained problems. The differences in SRWT and DRWT Jacobian matrices were remarkable. For DRWTs, the Jacobian also demonstrated the aerodynamic coupling between the two rotors. The geometry of the downstream main rotor blade was found to have a negligible effect on the aerodynamics of the upstream secondary rotor for relatively large rotor-rotor separation distances. However, the upstream secondary rotor had a considerable effect on the aerodynamic performance of the main rotor.

Reducing the levelized cost of energy (LOCE) is the ultimate goal of wind energy industry. Capturing more energy in windfarms is a way to reduce the LOCE. The goal of the work presented in Chapter 4 was to find the blade geometry that leads to the maximum energy

capture in windfarms. This is done by modifying the algorithm proposed in Chapter 3 to accept a new target function, $f = -C_{P,tot}$. The RANS/ADM method can predict far wake flow and therefore it is suitable for windfarm design purpose. To decrease the computational time, the Jacobian matrix is updated by Broydens method instead of actually calculating the entire matrix at each iteration. This idea was demonstrated to be very effective and saved up to 75% of computational time. For isolated wind turbines, increase in power capture by redesigning the available turbines was substantial. The total power of a windfarm was shown to be remarkably higher when the blade design of turbines operating in the wake were included in the design process. As an instance, for the case of ten in-line turbines the difference between the total power with and without including the downstream turbines in the design process was around 47%. This difference was achieved by a blade design that captures slightly less energy from the turbines in upstream rows but considerably more energy from the turbines operating in deep wake.

In summary, from the analysis I did in my research it can be deduced that DRWTs are able to capture more energy from the wind, especially through blade root loss mitigation. However, the focus of this research has been on aerodynamic analysis only. A more detailed study, especially from an economics point of view, is still needed to decide whether or not to use DRWTs instead of SRWTs. The benefits of using a relatively complex aerodynamic solver (i.e. RANS/ADM) in lieu of traditionally simple design methods (such as BEM) were remarkable as I could carry out design of windfarms, instead of being limited to design of isolated turbines. In addition, the design algorithm proposed in this thesis can technically be extended to include any other factor that influences the aerodynamic response of wind turbines and farms. The proposed algorithm is also not limited to work with any specific direct or inverse solvers. Depending on the designers' needs and computational resources, higher- or lower-fidelity solvers can be implemented into the algorithm.

BIBLIOGRAPHY

[1] A. Rosenberg, S Selvaraj, and A. Sharma. A novel dual-rotor turbine for increased wind energy capture. *Journal of Physics: Conference Series*, 524(1), 2014.

[2] James F Manwell, Jon G McGowan, and Anthony L Rogers. *Wind energy explained: theory, design and application*. John Wiley & Sons, 2010.

[3] Global Wind Energy Council. Global wind report 2014. *Brussels, Belgium*, pages 9–10, 2016.

[4] US EIA. Electric power monthly (february 2017).

[5] Wei Tong. *Wind power generation and wind turbine design*. WIT press, 2010.

[6] Mazharul Islam, David S-K Ting, and Amir Fartaj. Aerodynamic models for darrieus-type straight-bladed vertical axis wind turbines. *Renewable and Sustainable Energy Reviews*, 12(4):1087–1109, 2008.

[7] John O Dabiri. Potential order-of-magnitude enhancement of wind farm power density via counter-rotating vertical-axis wind turbine arrays. *Journal of renewable and sustainable energy*, 3(4):043104, 2011.

[8] Rozenn Wagner, Ioannis Antoniou, Søren M Pedersen, Michael S Courtney, and Hans E Jørgensen. The influence of the wind speed profile on wind turbine performance measurements. *Wind Energy*, 12(4):348–362, 2009.

[9] K Pope, I Dincer, and GF Naterer. Energy and exergy efficiency comparison of horizontal and vertical axis wind turbines. *Renewable energy*, 35(9):2102–2113, 2010.

[10] European Wind Energy Association et al. *Wind energy-the facts: a guide to the technology, economics and future of wind power.* Routledge, 2012.

[11] H Li and Zhe Chen. Overview of different wind generator systems and their comparisons. *IET Renewable Power Generation*, 2(2):123–138, 2008.

[12] Rebecca Jane Barthelmie, Sten Tronæs Frandsen, MN Nielsen, SC Pryor, P-E Rethore, and Hans Ejsing Jørgensen. Modelling and measurements of power losses and turbulence intensity in wind turbine wakes at middelgrunden offshore wind farm. *Wind Energy*, 10(6):517–528, 2007.

[13] Albert Betz. Schraubenpropeller mit geringstem energieverlust. mit einem zusatz von l. prandtl. *Nachrichten von der Gesellschaft der Wissenschaften zu Göttingen, Mathematisch-Physikalische Klasse*, 1919:193–217, 1919.

[14] Alexander M Gorlov, Valentin M Silantyev, et al. Limits of the turbine efficiency for free fluid flow. *Journal of energy resources technology*, 123:311–317, 2001.

[15] Aaron John Rosenberg. *A computational analysis of wind turbine and wind farm aerodynamics with a focus on dual rotor wind turbines.* PhD thesis, Iowa State University, 2016.

[16] A Rosenberg, Suganthi Selvaraj, and Anupam Sharma. A novel dual-rotor turbine for increased wind energy capture. In *Journal of Physics: Conference Series*, volume 524, page 012078. IOP Publishing, 2014.

[17] GM Joselin Herbert, Selvaraj Iniyan, E Sreevalsan, and S Rajapandian. A review of wind energy technologies. *Renewable and sustainable energy Reviews*, 11(6):1117–1145, 2007.

[18] B Sanderse, van der SP Pijl, and B Koren. Review of computational fluid dynamics for wind turbine wake aerodynamics. *Wind Energy*, 14(7):799–819, 2011.

[19] Rebecca Jane Barthelmie, SC Pryor, Sten Tronæs Frandsen, Kurt Schaldemose Hansen, JG Schepers, K Rados, W Schlez, A Neubert, LE Jensen, and S Neckelmann. Quantifying

the impact of wind turbine wakes on power output at offshore wind farms. *Journal of Atmospheric and Oceanic Technology*, 27(8):1302–1317, 2010.

[20] Rebecca Jane Barthelmie, K Hansen, Sten Tronæs Frandsen, Ole Rathmann, JG Schepers, W Schlez, J Phillips, K Rados, A Zervos, ES Politis, et al. Modelling and measuring flow and wind turbine wakes in large wind farms offshore. *Wind Energy*, 12(5):431–444, 2009.

[21] BG Newman. Multiple actuator-disc theory for wind turbines. *Journal of Wind Engineering and Industrial Aerodynamics*, 24(3):215–225, 1986.

[22] BG Newman. Actuator-disc theory for vertical-axis wind turbines. *Journal of Wind Engineering and Industrial Aerodynamics*, 15(1-3):347–355, 1983.

[23] Dale E Berg. Improved double-multiple streamtube model for the darrieus-type vertical-axis wind turbine. Technical report, Sandia National Labs., Albuquerque, NM (USA), 1983.

[24] TS No, J-E Kim, JH Moon, and SJ Kim. Modeling, control, and simulation of dual rotor wind turbine generator system. *Renewable Energy*, 34(10):2124–2132, 2009.

[25] Behnam Moghadassian, Aaron Rosenberg, and Anupam Sharma. Numerical investigation of aerodynamic performance and loads of a novel dual rotor wind turbine. *Energies*, 9(7):571, 2016.

[26] Zhenyu Wang, Ahmet Ozbay, Wei Tian, Anupam Sharma, and Hui Hu. An experimental investigation on the wake characteristics behind a novel twin-rotor wind turbine. In *AIAA SciTech, 33rd Wind Energy Symposium, AIAA Paper*, volume 1663, 2015.

[27] Raúl Bayoán Cal, José Lebrón, Luciano Castillo, Hyung Suk Kang, and Charles Meneveau. Experimental study of the horizontally averaged flow structure in a model wind-turbine array boundary layer. *Journal of Renewable and Sustainable Energy*, 2(1):013106, 2010.

[28] Mahdi Abkar and Fernando Porté-Agel. The effect of atmospheric stability on wind-turbine wakes: A large-eddy simulation study. In *Journal of Physics: Conference Series*, volume 524, page 012138. IOP Publishing, 2014.

[29] Henry Seifert and J Kroning. Recommendations for spacing in wind farms. In *European Wind Energy Conference, Madrid, Spain*, 2003.

[30] Niels Troldborg, Jens N Sørensen, and Robert Mikkelsen. Actuator line simulation of wake of wind turbine operating in turbulent inflow. In *Journal of physics: conference series*, volume 75, page 012063. IOP Publishing, 2007.

[31] Robert Mikkelsen, Jens N Sørensen, Stig Øye, and Niels Troldborg. Analysis of power enhancement for a row of wind turbines using the actuator line technique. In *Journal of Physics: Conference Series*, volume 75, page 012044. IOP Publishing, 2007.

[32] Robert Mikkelsen. Actuator disc methods applied to wind turbines. *Technical University of Denmark*, 2003.

[33] Pankaj K Jha, Matthew J Churchfield, Patrick J Moriarty, and Sven Schmitz. Guidelines for volume force distributions within actuator line modeling of wind turbines on large-eddy simulation-type grids. *Journal of Solar Energy Engineering*, 136(3):031003, 2014.

[34] G Crasto, AR Gravdahl, F Castellani, and E Piccioni. Wake modeling with the actuator disc concept. *Energy Procedia*, 24:385–392, 2012.

[35] Jens N Sørensen, Robert F Mikkelsen, Dan S Henningson, Stefan Ivanell, Sasan Sarmast, and Søren J Andersen. Simulation of wind turbine wakes using the actuator line technique. *Phil. Trans. R. Soc. A*, 373(2035):20140071, 2015.

[36] Jason Jonkman, Sandy Butterfield, Walter Musial, and George Scott. Definition of a 5-mw reference wind turbine for offshore system development. Technical report, National Renewable Energy Laboratory (NREL), Golden, CO., 2009.

[37] Paul A Durbin and BA Pettersson Reif. *Statistical theory and modeling for turbulent flows*. John Wiley & Sons, 2011.

[38] H Polinder, D Bang, RPJOM Van Rooij, AS McDonald, and MA Mueller. 10 mw wind turbine direct-drive generator design with pitch or active speed stall control. In *Electric Machines & Drives Conference, 2007. IEMDC'07. IEEE International*, volume 2, pages 1390–1395. IEEE, 2007.

[39] Marco Liserre, Roberto Cardenas, Marta Molinas, and Jose Rodriguez. Overview of multi-mw wind turbines and wind parks. *IEEE Transactions on Industrial Electronics*, 58(4):1081–1095, 2011.

[40] Thomas D Ashwill. Developments in large blades for lower cost wind turbines. *SAMPE Journal-Society for the Advancement of Material and Process Engineering*, 40(4):65–73, 2004.

[41] Paul S Veers, Thomas D Ashwill, Herbert J Sutherland, Daniel L Laird, Donald W Lobitz, Dayton A Griffin, John F Mandell, Walter D Musial, Kevin Jackson, Michael Zuteck, et al. Trends in the design, manufacture and evaluation of wind turbine blades. *Wind Energy*, 6(3):245–259, 2003.

[42] Ernesto Benini, Andrea Toffolo, et al. Optimal design of horizontal-axis wind turbines using blade-element theory and evolutionary computation. *TRANSACTIONS-AMERICAN SOCIETY OF MECHANICAL ENGINEERS JOURNAL OF SOLAR ENERGY ENGINEERING*, 124(4):357–363, 2002.

[43] MEZYK Jureczko, M Pawlak, and A Mezyk. Optimisation of wind turbine blades. *Journal of materials processing technology*, 167(2):463–471, 2005.

[44] Karam Y Maalawi and Hani M Negm. Optimal frequency design of wind turbine blades. *Journal of Wind Engineering and Industrial Aerodynamics*, 90(8):961–986, 2002.

[45] Seongkyu Lee. Inverse design of horizontal axis wind turbine blades using a vortex line method. *Wind Energy*, 18(2):253–266, 2015.

[46] JCC Henriques, F Marques Da Silva, AI Estanqueiro, and LMC Gato. Design of a

new urban wind turbine airfoil using a pressure-load inverse method. *Renewable Energy*, 34(12):2728–2734, 2009.

[47] Michael S Selig and James L Tangler. Development and application of a multipoint inverse design method for horizontal axis wind turbines. *Wind Engineering*, pages 91–105, 1995.

[48] Richard H Byrd, Jean Charles Gilbert, and Jorge Nocedal. A trust region method based on interior point techniques for nonlinear programming. *Mathematical Programming*, 89(1):149–185, 2000.

[49] Andrew R Conn, Nicholas IM Gould, and Philippe L Toint. *Trust region methods*. SIAM, 2000.

[50] Jens Nørkær Sørensen and Robert Flemming Mikkelsen. On the validity of the blade element momentum theory. In *2001 European Wind Energy Conference and Exhibition (EWEC'01)*. WIP-Renewable Energies, 2001.

[51] Sven G Hedman. Vortex lattice method for calculation of quasi steady state loadings on thin elastic wings in subsonic flow. Technical report, AERONAUTICAL RESEARCH INST OF SWEDEN STOCKHOLM, 1966.

[52] Xiongwei Liu, Lin Wang, and Xinzi Tang. Optimized linearization of chord and twist angle profiles for fixed-pitch fixed-speed wind turbine blades. *Renewable Energy*, 57:111–119, 2013.

[53] Mojtaba Tahani, Ghazale Kavari, Mehran Masdari, and Mojtaba Mirhosseini. Aerodynamic design of horizontal axis wind turbine with innovative local linearization of chord and twist distributions. *Energy*, 131:78–91, 2017.

[54] Wen Zhong Shen and J Sørensen. Numerical modeling of wind turbine wakes. *J. Fluids Eng*, 124(2):393–399, 2002.

[55] R Malki, AJ Williams, TN Croft, M Togneri, and I Masters. A coupled blade element momentum–computational fluid dynamics model for evaluating tidal stream turbine performance. *Applied Mathematical Modelling*, 37(5):3006–3020, 2013.

[56] A Olczak, T Stallard, T Feng, and PK Stansby. Comparison of a rans blade element model for tidal turbine arrays with laboratory scale measurements of wake velocity and rotor thrust. *Journal of Fluids and Structures*, 64:87–106, 2016.

[57] Charles G Broyden. A class of methods for solving nonlinear simultaneous equations. *Mathematics of computation*, 19(92):577–593, 1965.

[58] A. Sharma, F. Taghaddosi, and A. Gupta. Diagnosis of aerodynamic losses in the root region of a horizontal axis wind turbine, 2010. General Electric Company Technical Report.

[59] R. J. Barthelmie and L. E. Jensen. Evaluation of power losses due to wind turbine wakes at the Nysted offshore wind farm. *Wind Energy*, 13:573–586, 2010.

[60] JP Baker, EA Mayda, and CP Van Dam. Experimental analysis of thick blunt trailing-edge wind turbine airfoils. *Journal of Solar Energy Engineering*, 128(4):422–431, 2006.

[61] Peter Fuglsang and Christian Bak. Development of the Risø wind turbine airfoils. *Wind Energy*, 7(2):145–162, 2004.

[62] Andrew Kusiak and Zhe Song. Design of wind farm layout for maximum wind energy capture. *Renewable Energy*, 35(3):685–694, 2010.

[63] Javier Serrano González, Angel G Gonzalez Rodriguez, José Castro Mora, Jesús Riquelme Santos, and Manuel Burgos Payan. Optimization of wind farm turbines layout using an evolutive algorithm. *Renewable Energy*, 35(8):1671–1681, 2010.

[64] Prateek Mittal, Kedar Kulkarni, and Kishalay Mitra. A novel hybrid optimization methodology to optimize the total number and placement of wind turbines. *Renewable Energy*, 86:133–147, 2016.

[65] John O. Dabiri. Potential order-of-magnitude enhancement of wind farm power density via counter-rotating vertical-axis wind turbine arrays. *Journal of Renewable and Sustainable Energy*, 3(4):043104, 2011.

[66] Gustave Paul Corten, Koert Lindenburg, and Pieter Schaak. Assembly of energy flow collectors, such as windpark, and method of operation, November 27 2007. US Patent 7,299,627.

[67] Ángel Jiménez, Antonio Crespo, and Emilio Migoya. Application of a les technique to characterize the wake deflection of a wind turbine in yaw. *Wind energy*, 13(6):559–572, 2010.

[68] Carsten Hein Westergaard. Method for improving large array wind park power performance through active wake manipulation reducing shadow effects, August 21 2012. US Patent App. 14/344,284.

[69] B.G. Newman. Multiple actuator-disc theory for wind turbines. *Journal of Wind Engineering and Industrial Aerodynamics*, 24:215–225, 1986.

[70] Sung Nam Jung, Tae-Soo No, and Ki-Wahn Ryu. Aerodynamic performance prediction of a 30kw counter-rotating wind turbine system. *Renewable Energy*, 30(5):631–644, 2005.

[71] Toshiaki Kanemoto and Ahmed Mohamed Galal. Development of intelligent wind turbine generator with tandem wind rotors and double rotational armatures (1st report, superior operation of tandem wind rotors). *JSME International Journal Series B*, 49(2):450–457, 2006.

[72] Toshiaki Kanemoto. Wind turbine generator, January 28 2010. US Patent App. 13/147,021.

[73] A Rosenberg and A Sharma. A prescribed-wake vortex lattice method for aerodynamic analysis and optimization of co-axial, dual-rotor wind turbines. *ASME Journal of Solar Energy Engineering*, 2016. (in review).

[74] Suganthi Selvaraj. *Numerical Investigation of Wind Turbine and Wind Farm Aerodynamics*. Thesis, Iowa State University, 2014.

[75] J. Jonkman, S. Butterfield, W. Musial, and G. Scott. Definition of a 5-mw reference wind turbine for offshore system development, 2009.

[76] R. Mikkelsen. *Actuator Disk Models Applied to Wind Turbines.* Thesis, Technical University of Denmark, 2003.

[77] A. Betz. *Schraubenpropeller mit Geringstem Energieverlust.* Thesis, Gottingen Nachrichten, 1919.

[78] S. Goldstein. On the vortex theory of screw propellers. *Proceedings of the Royal Society of London Series A: Mathematical, Physical and Engineering Sciences*, 123(792):440–465, 1929.

[79] T. Burton, D. Sharpe, N. Jenkins, and E. Bossanyi. *Wind Energy Handbook.* John Wiley & Sons Ltd., 2002.

[80] J. F. Ainslie. Calculating the flow field in the wake of wind turbines. *Journal of Wind Engineering and Industrial Aerodynamics*, 27:213–224, 1988.

[81] H. Snel. Review of aerodynamics for wind turbines. *Wind Energy*, 6:203–211, 2003.

[82] M. Calaf, C. Meneveau, and J. Meyers. Large eddy simulation study of fully developed wind-turbine array boundary layers. *Physics of Fluids*, 22(1), 2010.

[83] L. J. Vermeer, J. N. Sørensen, and A. Crespo. Wind turbine wake aerodynamics. *Progress in Aerospace Sciences*, 39, 2003.

[84] B. Sanderse, S. P. van der Pijl, and B. Koren. Review of computational fluids dynamics for wind turbine wake aerodynamics. *Wind Energy*, 2011.

[85] A. Jimenez, A. Crespo, E. Migoya, and J. Garcia. Advances in large-eddy simulation of a wind turbine wake. *Journal of Physics: Conference Series*, 75, 2007.

[86] A. Jimenez, A. Crespo, E. Migoya, and J. J. Garica. Large eddy simulation of spectral coherence in a wind turbine wake. *Environmental Research Letters*, 3, 2008.

[87] F. Porté-Agel, Y. Wu, H. Lu, and R. J. Conzemius. Large-eddy simulation of atmospheric boundary layer flow through wind turbines and wind farms. *Journal of Wind Engineering and Industrial Aerodynamics*, 99:154–168, 2011.

[88] Y. Wu and F. Porté-Agel. Large-eddy simulation of wind-turbine wakes: Evaluation of turbine parametrisations. *Boundary-Layer Meteorology*, 138(3), 2011.

[89] N. Troldborg, G. C. Larsen, H. A. Madsen, K. S. Hansen, J. N. Sørensen, and R. Mikkelsen. Numerical simulations of wake interaction between two wind turbines at various inflow conditions. *Wind Energy*, 14(7):859–876, 2011.

[90] Fernando Porté-Agel, Yu-Ting Wu, and Chang-Hung Chen. A numerical study of the effects of wind direction on turbine wakes and power losses in a large wind farm. *Energies*, 6(10):5297–5313, 2013.

[91] Richard JAM Stevens, Dennice F Gayme, and Charles Meneveau. Large eddy simulation studies of the effects of alignment and wind farm length. *Journal of renewable and sustainable energy*, 6(2):023105, 2014.

[92] M. J. Churchfield, S. Lee, J. Michalakes, and P. J. Moriarty. A numerical study of the effects of atmospheric and wake turbulence on wind turbine dynamics. *Journal of Turbulence*, 13(14):1–32, 2012.

[93] M. Churchfield, S. Lee, and P. Moriarty. A large-eddy simulation of wind-plant aerodynamics, 2012.

[94] J. Smagorinsky. General circulation experiments with the primitive equations i. the basic experiment. *Monthly Weather Review*, 91, 1963.

[95] Douglas K Lilly. A proposed modification of the germano subgrid-scale closure method. *Physics of Fluids A: Fluid Dynamics (1989-1993)*, 4(3):633–635, 1992.

[96] Massimo Germano, Ugo Piomelli, Parviz Moin, and William H Cabot. A dynamic subgrid-scale eddy viscosity model. *Physics of Fluids A: Fluid Dynamics (1989-1993)*, 3(7):1760–1765, 1991.

[97] M Churchfield and S Lee. Nwtc design codes (sowfa), 2013.

[98] C. Moeng. A large-eddy-simulation model for the study of planetary boundary-layer turbulence. *Journal of the Atmospheric Sciences*, 41(13):2052–2062, 1984.

[99] R. B. Stull. *An Introduction to Boundary Layer Meteorology*. Kluwer Academic Publishers, 1988.

[100] S. Lee, P. Moriarty, and M. Churchfield. On fatigue loadings of wind turbines from atmospheric boundary layer, 2012.

[101] J. Jonkman and M. Buhl. Fast user's guide, 2005.

[102] J.G. Schepers, A.J. Brand, A. Bruining, J.M.R. Graham, M.M. Hand, D.G. Infield, H.A. Madsen, R.J.H. Paynter, and D.A. Simms. Final report of iea annex xiv: Field rotor aerodynamics. Technical Report ECN-C-97-027, Energy Research Center of the Netherlands, 1997.

[103] World Meteorological Organization. *Guide to meteorological instruments and methods of observation*. Secretariat of the World Meteorological Organization, 1983.

[104] Lars Davidson. Hybrid les-rans: Inlet boundary conditions for flows with recirculation. In *Advances in Hybrid RANS-LES Modelling*, pages 55–66. Springer, 2008.

[105] Leon Sedefian and Edward Bennett. A comparison of turbulence classification schemes. *Atmospheric Environment (1967)*, 14(7):741–750, 1980.

[106] Joost A Businger. Turbulent transfer in the atmospheric surface layer. In *Workshop on micrometeorology*, pages 67–100. Amer. Met, Soc,, 1973.

[107] Leonardo P Chamorro and Fernando Porté-Agel. Effects of thermal stability and incoming boundary-layer flow characteristics on wind-turbine wakes: a wind-tunnel study. *Boundary-layer meteorology*, 136(3):515–533, 2010.

[108] Pankaj K Jha, Earl PN Duque, Jessica L Bashioum, and Sven Schmitz. Unraveling the mysteries of turbulence transport in a wind farm. *Energies*, 8(7):6468–6496, 2015.

[109] LP Chamorro, M Guala, REA Arndt, and F Sotiropoulos. On the evolution of turbulent scales in the wake of a wind turbine model. *Journal of Turbulence*, 13, 2012.

110

[110] Yu-Ting Wu and Fernando Porté-Agel. Large-eddy simulation of wind-turbine wakes: evaluation of turbine parametrisations. *Boundary-layer meteorology*, 138(3):345–366, 2011.

[111] Jean-Jacques Chattot. Optimization of wind turbines using helicoidal vortex model. *Journal of solar energy engineering*, 125(4):418–424, 2003.

[112] Sydney Goldstein. On the vortex theory of screw propellers. *Proceedings of the Royal Society of London. Series A, Containing Papers of a Mathematical and Physical Character*, 123(792):440–465, 1929.

[113] Michael S Selig and Victoria L Coverstone-Carroll. Application of a genetic algorithm to wind turbine design. *Journal of Energy Resources Technology*, 118(1):22–28, 1996.

[114] P Giguere and MS Selig. Desirable airfoil characteristics for large variable-speed horizontal axis wind turbines. *Journal of solar energy engineering*, 119(3):253–260, 1997.

[115] Ki-Hak Lee, Kyu-Hong Kim, Dong-Ho Lee, Kyung-Tae Lee, and Jong-Po Park. Two-step optimization for wind turbine blade with probability approach. *Journal of Solar Energy Engineering*, 132(3):034503, 2010.

[116] Charles N Adkins and Robert H Liebeck. Design of optimum propellers. *Journal of Propulsion and Power*, 10(5):676–682, 1994.

[117] Peter Bachant and Martin Wosnik. Modeling the near-wake of a vertical-axis cross-flow turbine with 2-d and 3-d rans. *arXiv preprint arXiv:1604.02611*, 2016.

[118] HF Lam and HY Peng. Study of wake characteristics of a vertical axis wind turbine by two-and three-dimensional computational fluid dynamics simulations. *Renewable Energy*, 90:386–398, 2016.

[119] Andrea Alaimo, Antonio Esposito, Antonio Messineo, Calogero Orlando, and Davide Tumino. 3d cfd analysis of a vertical axis wind turbine. *Energies*, 8(4):3013–3033, 2015.

[120] Philip Marsh, Dev Ranmuthugala, Irene Penesis, and Giles Thomas. Three-dimensional numerical simulations of straight-bladed vertical axis tidal turbines investigating power output, torque ripple and mounting forces. *Renewable Energy*, 83:67–77, 2015.

[121] Suganthi Selvaraj. *Numerical investigation of wind turbine and wind farm aerodynamics*. PhD thesis, Iowa State University, 2014.

[122] N Troldberg. Actuator line modeling of wind turbine wakes (ph. d. thesis). *Department of Mechanical Engineering, Technical University of Denmark, Lynby*, 2008.

[123] Jens N Sørensen and Asger Myken. Unsteady actuator disc model for horizontal axis wind turbines. *Journal of Wind Engineering and Industrial Aerodynamics*, 39(1):139–149, 1992.

[124] Thomas F Coleman and Yuying Li. On the convergence of interior-reflective newton methods for nonlinear minimization subject to bounds. *Mathematical programming*, 67(1-3):189–224, 1994.

[125] Behnam Moghadassian, Aaron Rosenberg, and Anupam Sharma. Numerical investigation of aerodynamic performance and loads of a novel dual rotor wind turbine. *Energies*, 9(571), 2016.

[126] Aaron Rosenberg and Anupam Sharma. A prescribed-wake vortex lattice method for preliminary design of co-axial, dual-rotor wind turbines. *Journal of Solar Energy Engineering*, 138(6), 2016.

[127] Behnam Moghadassian, Aaron Rosenberg, Hui Hu, and Anupam Sharma. Numerical investigation of aerodynamic performance and loads of a novel dual rotor wind turbine.

[128] Z Wang, W. Tian, A. Ozbay, A Sharma, and H. Hui. An experimental study on the aeromechanics and wake characteristics of a novel twin-rotor wind turbine in a turbulent boundary layer flow. *Experiments in Fluids*, 57(-):150, 2016.

[129] Suhas V Patankar and D Brian Spalding. A calculation procedure for heat, mass and momentum transfer in three-dimensional parabolic flows. *International journal of heat and mass transfer*, 15(10):1787–1806, 1972.

[130] Brian Edward Launder and DB Spalding. The numerical computation of turbulent flows. *Computer methods in applied mechanics and engineering*, 3(2):269–289, 1974.

[131] DM Hargreaves and Nigel G Wright. On the use of the k–ε model in commercial cfd software to model the neutral atmospheric boundary layer. *Journal of Wind Engineering and Industrial Aerodynamics*, 95(5):355–369, 2007.

[132] Aaron Rosenberg. *A Computational Analysis of Wind Turbine and Wind Farm Aerodynamics with a Focus on Dual Rotor Wind Turbines*. PhD thesis, Iowa State University, 2016.

[133] Andrew S Thelen, Leifur T Leifsson, Anupam Sharma, and Slawomir Koziel. Direct and surrogate-based optimization of dual-rotor wind turbines. In *34th Wind Energy Symposium*, page 1265, 2016.

[134] Richard H Byrd, Robert B Schnabel, and Gerald A Shultz. A trust region algorithm for nonlinearly constrained optimization. *SIAM Journal on Numerical Analysis*, 24(5):1152–1170, 1987.

[135] MM Hand, DA Simms, LJ Fingersh, DW Jager, JR Cotrell, S Schreck, and SM Larwood. Unsteady aerodynamics experiment phase vi: wind tunnel test configurations and available data campaigns. *National Renewable Energy Laboratory, Golden, CO, Report No. NREL/TP-500-29955*, 2001.

[136] Mark Drela. Xfoil: An analysis and design system for low reynolds number airfoils. In *Low Reynolds number aerodynamics*, pages 1–12. Springer, 1989.

[137] LJ Vermeer, Jens Nørkær Sørensen, and A Crespo. Wind turbine wake aerodynamics. *Progress in Aerospace Sciences*, 39(6):467–510, 2003.

[138] Florian R Menter. Improved two-equation k-omega turbulence models for aerodynamic flows. 1992.

[139] Bijan Mohammadi and Olivier Pironneau. Analysis of the k-epsilon turbulence model. 1993.

[140] Ian Masters, Rami Malki, Alison J Williams, and T Nicholas Croft. The influence of flow acceleration on tidal stream turbine wake dynamics: A numerical study using a coupled bem–cfd model. *Applied Mathematical Modelling*, 37(16):7905–7918, 2013.

[141] M Paul Laan, Niels N Sørensen, Pierre-Elouan Réthoré, Jakob Mann, Mark C Kelly, Niels Troldborg, J Gerard Schepers, and Ewan Machefaux. An improved $k - \epsilon$ model applied to a wind turbine wake in atmospheric turbulence. *Wind Energy*, 18(5):889–907, 2015.

[142] Michael Shives and Curran Crawford. Adapted two-equation turbulence closures for actuator disk rans simulations of wind & tidal turbine wakes. *Renewable Energy*, 92:273–292, 2016.

[143] Ludwig Prandtl and Albert Betz. *Vier Abhandlungen zur Hydrodynamik und Aerodynamik*, volume 3. Universitätsverlag Göttingen, 2010.

[144] Carl T Kelley. *Iterative methods for optimization*. SIAM, 1999.

[145] John E Dennis, Jr and Jorge J Moré. Quasi-newton methods, motivation and theory. *SIAM review*, 19(1):46–89, 1977.

[146] Richard H Byrd, Jorge Nocedal, and Robert B Schnabel. Representations of quasi-newton matrices and their use in limited memory methods. *Mathematical Programming*, 63(1):129–156, 1994.

[147] Behnam Moghadassian and Anupam Sharma. Inverse design of single-and multi-rotor horizontal axis wind turbine blades using computational fluid dynamics. *Journal of Solar Energy Engineering*, 2017. accepted.

[148] B. Moghadassian and A. Sharma. Inverse design of single- and multi-rotor horizontal axis wind turbine blades using computational fluid dynamics. In *2017 AIAA Science and Technology Forum and Exposition (SciTech 2017)*, Grapevine, TX, USA, 2017.

APPENDIX .   ADDITIONAL MATERIAL

A   Coordinate Systems

Three coordinate systems are used: (1) attached to the ground in which the CFD simulations are performed, which is specified by the unit vectors $(\hat{e}_{\tilde{x}}, \hat{e}_{\tilde{y}}, \hat{e}_z)$; $\hat{e}_{\tilde{x}}$ points East, $\hat{e}_{\tilde{y}}$ points North, and $\hat{e}_z$ points up and away from the ground (Earth), (2) the coordinate system aligned with the freestream flow direction given by the unit vectors $(\hat{e}_x, \hat{e}_y, \hat{e}_z)$, where $\hat{e}_x$ makes an angle ϕ with $\hat{e}_{\tilde{x}}$, and (3) a cylindrical coordinate system given by $(\hat{e}_r, \hat{e}_\theta, \hat{e}_z)$ is used to compute turbulent momentum and energy flux into a cylindrical region behind the turbine rotor. These coordinates and their inter-relationships are shown in Fig. A.1.

(a) $(\hat{e}_{\tilde{x}}, \hat{e}_{\tilde{y}}) \rightarrow (\hat{e}_x, \hat{e}_y)$ (b) $(\hat{e}_x, \hat{e}_y) \rightarrow (\hat{e}_r, \hat{e}_\theta)$
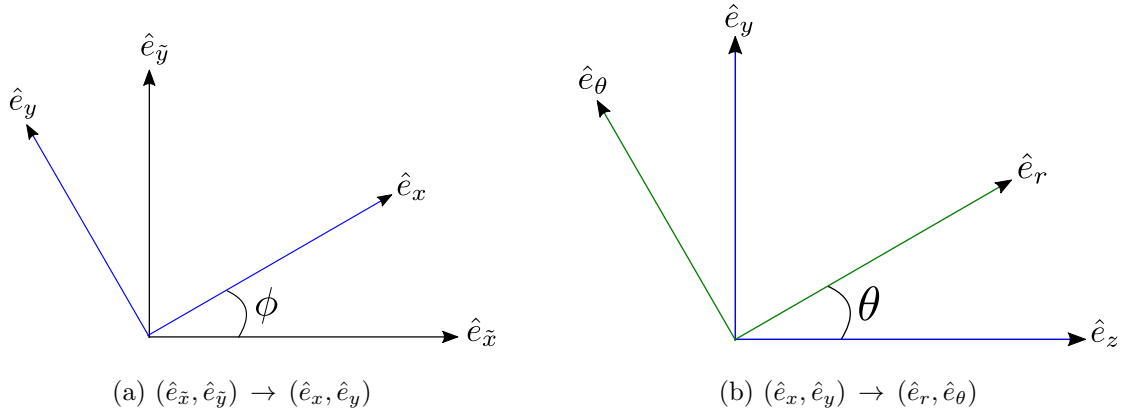
Figure A.1: The three coordinate systems used and their interrelationships. The CFD simulations are performed in $(\hat{e}_{\tilde{x}}, \hat{e}_{\tilde{y}}, \hat{e}_z)$; meanflow is along the $\hat{e}_x$ direction.

A.1   Streamwise Turbulence Intensity

Streamwise turbulence intensity is $\sigma_{u_x}/u_{\infty,h}$, where u_x denotes the wind velocity component in the $\hat{e}_x$ direction.

The following relates the desired streamwise turbulence intensity to Reynolds stresses computed in the $(\hat{e}_{\tilde{x}}, \hat{e}_{\tilde{y}}, \hat{e}_z)$ coordinate system.

$$\sigma_{u'_x}^2 = \overline{u_x'^2} = \overline{\left(u'_{\tilde{x}}\cos\phi + u'_{\tilde{y}}\sin\phi\right)^2}$$

$$= \overline{u_{\tilde{x}}'^2}\cos^2\phi + \overline{u_{\tilde{y}}'^2}\sin^2\phi + \overline{u'_{\tilde{x}}u'_{\tilde{y}}}\sin(2\phi) \tag{A.1}$$

A.2 Streamwise Turbulent Momentum and Energy Flux

Streamwise turbulent momentum flux through the circular cylinder in Fig. 2.14 is determined by integrating the Reynolds stress term $\overline{u'_r u'_x}$ over the cylinder surface. $\overline{u'_r u'_x}$ is related to the Reynolds stress defined in the $(\hat{e}_{\tilde{x}}, \hat{e}_{\tilde{y}}, \hat{e}_z)$ coordinate system as follows:

$$\overline{u'_r u'_x} = \overline{(u'_z\cos\theta + u'_y\sin\theta) \times (u'_{\tilde{x}}\cos\phi + u'_{\tilde{y}}\sin\phi)}$$

$$= \left(\overline{u'_{\tilde{x}}u'_z}\cos\phi + \overline{u'_{\tilde{y}}u'_z}\sin\phi\right)\cos\theta + \left(\overline{u'_{\tilde{x}}u'_y}\cos\phi + \overline{u'_{\tilde{y}}u'_y}\sin\phi\right)\sin\theta, \tag{A.2}$$

where,

$$\overline{u'_{\tilde{x}}u'_y} = \overline{u'_{\tilde{x}}u'_{\tilde{y}}}\cos\phi - \overline{u_{\tilde{x}}'^2}\sin\phi, \text{ and}$$

$$\overline{u'_{\tilde{y}}u'_y} = \overline{u_{\tilde{y}}'^2}\cos\phi - \overline{u'_{\tilde{x}}u'_{\tilde{y}}}\sin\phi.$$

Using these in Eq. A.2 gives

$$\overline{u'_r u'_x} = \left(\overline{u'_{\tilde{x}}u'_z}\cos\phi + \overline{u'_{\tilde{y}}u'_z}\sin\phi\right)\cos\theta$$

$$+ \left(\overline{u'_{\tilde{x}}u'_{\tilde{y}}}\cos^2\phi - \overline{u'_{\tilde{x}}u'_{\tilde{y}}}\sin^2\phi + \overline{u_{\tilde{y}}'^2}\frac{\sin(2\phi)}{2} - \overline{u_{\tilde{x}}'^2}\frac{\sin(2\phi)}{2}\right)\sin\theta,$$

$$\text{or, } \overline{u'_r u'_x} = \left(\overline{u'_{\tilde{x}}u'_z}\cos\phi + \overline{u'_{\tilde{y}}u'_z}\sin\phi\right)\cos\theta$$

$$+ \left(\overline{u'_{\tilde{x}}u'_{\tilde{y}}}\cos(2\phi) + (\overline{u_{\tilde{y}}'^2} - \overline{u_{\tilde{x}}'^2})\frac{\sin(2\phi)}{2}\right)\sin\theta. \tag{A.3}$$

The turbulent energy flux is obtained by integrating the following over the surface.

$$\overline{u}_x \times \overline{u'_r u'_x} = \overline{u'_{\tilde{x}}\cos\phi + u'_{\tilde{y}}\sin\phi} \times \overline{u'_r u'_x} \tag{A.4}$$